

INFORMATION TO USERS

This manuscript has been reproduced from the microfilm master. UMI films the text directly from the original or copy submitted. Thus, some thesis and dissertation copies are in typewriter face, while others may be from any type of computer printer.

The quality of this reproduction is dependent upon the quality of the copy submitted. Broken or indistinct print, colored or poor quality illustrations and photographs, print bleedthrough, substandard margins, and improper alignment can adversely affect reproduction.

In the unlikely event that the author did not send UMI a complete manuscript and there are missing pages, these will be noted. Also, if unauthorized copyright material had to be removed, a note will indicate the deletion.

Oversize materials (e.g., maps, drawings, charts) are reproduced by sectioning the original, beginning at the upper left-hand corner and continuing from left to right in equal sections with small overlaps.

Photographs included in the original manuscript have been reproduced xerographically in this copy. Higher quality 6" x 9" black and white photographic prints are available for any photographs or illustrations appearing in this copy for an additional charge. Contact UMI directly to order.

ProQuest Information and Learning
300 North Zeeb Road, Ann Arbor, MI 48106-1346 USA
800-521-0600

UMI[®]

DEVELOPMENT OF LASSA: A LARGE AREA SILICON STRIP
ARRAY FOR NUCLEAR REACTION STUDIES AND
INVESTIGATION OF MID-VELOCITY FRAGMENT EMISSION IN
 $^{114}\text{Cd} + ^{92,98}\text{Mo}$ REACTIONS AT $E/A = 50$ MEV

Brian P. Davin

Submitted to the faculty of the University Graduate School
in partial fulfillment of the requirements
for the degree of
Doctor of Philosophy
in the Department of Chemistry,
Indiana University
October 2001

UMI Number: 3038556

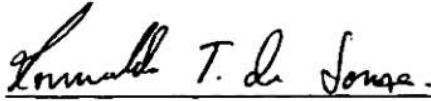
UMI[®]

UMI Microform 3038556

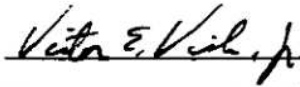
**Copyright 2002 by ProQuest Information and Learning Company.
All rights reserved. This microform edition is protected against
unauthorized copying under Title 17, United States Code.**

**ProQuest Information and Learning Company
300 North Zeeb Road
P.O. Box 1346
Ann Arbor, MI 48106-1346**

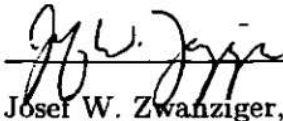
Accepted by the Graduate Faculty, Indiana University, in partial fulfillment of the requirements for the degree of Doctor of Philosophy.




Romualdo T. de Souza, Ph.D.



Victor E. Viola Jr., Ph.D.



Josef W. Zwanziger, Ph.D.



David E. Clemmer, Ph.D.

Oral Examination

October 23, 2001

Dedication

To my wife Kimberley,
my mother and father,
and H.P. Gronemeier ('til we meet again)

Acknowledgments

I would first like to thank my advisor Romualdo de Souza for his time and support during my graduate studies. His keen insight made it possible to accomplish many experiments and this thesis. I would also like to thank the members of my research committee Vic Viola, Joe Zwanziger and David Clemmer.

The post-docs and fellow group members who assisted me with the trials and tribulations of being a graduate student are Kris Kwiatkowski, Dan Fox, Earl Cornell, Yunian Lou, Yves Larochelle, Luc Beaulieu, Thomas Lefort, Ricardo Yanez, Ruben Alfaro-Molina, Anne Caraley, Hushan Xu, Shaolin Chen, Todd Hamilton, Todd Bredeweg. I would like to thank them all for their valuable input.

The LASSA project was the primary focus during my latter graduate studies. I am deeply indebted to the technical staffs at Indiana University (IU), NSCL at Michigan State University (MSU) and Washington University (WU) for their contributions to this project. Without their skills this project would not have been possible. John Dorsett, Kenny Bastin, and Gary Fleener from the IU mechanical shop who fabricated the LASSA components. Deon Osman, Richard Landgrebe and Ray Sporleder from the IU electronic shop who helped with creation of the flexible leads needed for the project, while John Poehlman, Andy Alexander and Paul Ludlow designed and fabricated the pre-amps. The signal processing modules required to process the multiple signals from LASSA were designed and built by John Elson at WU. Fabrication of the LASSA frames was done by the machine shop at WU. Len Morris at MSU used my initial ideas and made them a physical reality.

I would also like to thank my fellow colleagues who assisted with the running of my thesis experiment. They are Andreas Wagner, Tianxiao Liu, Xiaodong Liu, Bill Lynch, Richard Shomin, Wanpeng Tan, Betty Tsang, John Yurkon, Ron Fox, Jack Ottarson, and Skip Vander Molen from MSU, Jan Toke from University of Rochester, and Bob Charity and Lee Sobotka from WU. In addition, the operations group deserves my deepest gratitude for supplying the multiple beams we requested.

Two organizations who have helped me greatly with support are P.E.A.C. for their many discussions and insights on physics and life. A special thanks goes to the folks at SVGC for their assistance while they were overcoming the tyranny which was besieged upon them.

Lastly, I need to thank my family for their support during my journey. My parents, sister and parents-in-law who never failed to support me. Most importantly I need to thank my wife Kimberley for her support, love and *much* patience during my graduate years.

Abstract

Brian P. Davin

DEVELOPMENT OF LASSA: A LARGE AREA SILICON STRIP ARRAY FOR NUCLEAR REACTION STUDIES AND INVESTIGATION OF MID-VELOCITY FRAGMENT EMISSION IN $^{114}\text{Cd} + ^{92,98}\text{Mo}$ REACTIONS AT $E/A = 50$ MEV

A new high-resolution, low-threshold, charged-particle detector array, LASSA, was developed for the detection of isotopically resolved fragments emitted in intermediate energy heavy-ion reactions. This array of nine telescopes utilizes silicon-strip technology and a novel method for mounting the silicon detectors. Each telescope of the array consists of a Si-Si-CsI(Tl) stack and provides isotopic resolution for $Z \leq 8$ with good angular ($\theta_{lab} \leq 0.9^\circ$) and energy resolution.

Investigation of peripheral collisions in the reaction $^{114}\text{Cd} + ^{92}\text{Mo}$ at $E_{lab}/A = 50$ MeV reveals that fragment emission aft of the projectile-like fragment (PLF) is enhanced relative to emission forward of the PLF. Examination of events in which the PLF undergoes binary decay indicates the existence of two components. Based upon the relative magnitude of the velocity of the two decay products or their relative velocity, one can separate these two components. One of these two components can be understood as the standard statistical decay of the excited PLF. Comparison of the charge correlations selected on the relative magnitudes of two fragment velocities indicates that while for the standard decay component the sizes of the two fragments involved in the binary split are anti-correlated, for the second component the size of the smaller fragment is independent of the size of the larger fragment. The non-standard component also exhibits a different Z distribution as compared to the standard component. Characteristics of both components are explored.

Romualdo T. de Souza, Ph.D. (chair)

Josef W. Zwanziger, Ph.D.

Victor E. Viola Jr., Ph.D.

David E. Clemmer, Ph.D.

Contents

1 Introduction	1
References	9
2 LASSA: A Large Area Silicon Strip Array for Isotopic Identification of Charged Particles	11
2.1 Introduction	11
2.2 Design Constraints	12
2.3 Si Detectors	14
2.3.1 Mechanical Mounting and Electrical Contacts	14
2.3.2 Measurement of Silicon Resolution and Depletion Voltage	16
2.4 Electronics	20
2.4.1 Charge Integrating Pre-amplifier	21
2.4.2 Silicon Processor Module	23
2.4.3 Stability Measurement	24
2.5 Overview of LASSA Data Acquisition	27
2.6 Calibration	29
2.6.1 Thickness Non-uniformity Correction for the 65 μm Detector	32
2.6.2 Thickness Determination for the 500 μm Detector	36
2.6.3 Isotopic Resolution in the Si-CsI(Tl)	36
2.7 Energy calibration of the CsI(Tl)	40
References	44
3 Experimental Details	46
3.1 Experimental Details	46

3.2	Miniball/Miniwall	47
3.2.1	Particle Identification	47
3.3	Ring Counter	53
3.3.1	Energy Calibration of the Silicon Pie Detectors	53
3.3.2	Energy Calibration of the Annular Ring Detectors	56
3.3.3	Energy Calibration of CsI(Tl) Detectors	56
3.3.4	Particle Identification	63
3.3.5	Consistency Checks	63
	References	69
4	General Characteristics of PLF* Decay	70
4.1	Introduction	70
4.2	General Reaction Characteristics	71
4.3	Analysis of the $N_{RC} = 2$ case	80
	References	99
5	Fragment Production in Non-central Collisions of Intermediate Energy	
	Heavy Ions	100
5.1	Introduction	100
5.2	General Reaction Features	101
5.3	Charge-Charge Correlations	102
5.4	Relative Velocity of Two Fragments	104
5.5	Atomic Number Distribution of Two Fragments	108
	References	111
6	Fragment Isospin as a Probe of Heavy-Ion Collisions	113
6.1	Introduction	113
6.2	IMF Yield Ratios	114
6.3	Model Comparisons	117
	References	124
7	Conclusions	125

A	Design and Fabrication of the Polyimide Cable	129
A.1	Introduction	129
A.2	Design of the Polyimide Cable	129
A.3	Etching of the Polyimide traces	130
A.4	Lamination of the Polyimide Cable	132
A.5	Plating of the Ground Signals	134
A.6	Bending of Polyimide Cable	135
A.7	Attaching a Front Cable to the PCB Frame	136
A.8	Attaching a Back Cable to the PCB Frame	147
A.9	Plating of the Signal Pads	148
A.10	Attachment of the Connector	148
	References	149
B	Data Analysis Techniques	150
B.1	Data Tape Format	150
B.1.1	Raw Data Tape Format	150
B.1.2	Physics Disk Format	152
B.1.3	Stripped Disk Format	153
B.2	List of Programs	154
B.2.1	Calibration	154
B.2.2	Analysis	156
C	Thickness Uniformity of Nominally 30μm Thick Silicon Detectors	157
C.1	Introduction	157
C.2	Test setup	157
C.3	Analysis of data	160
	References	165

List of Figures

1.1	Pictorial representation of the Rayleigh instability of a fluid jet	3
1.2	Galilean-invariant emission patterns of light charged particles and IMF's co-incident with PLF's from peripheral collision	5
1.3	Ratio of the measured yields of neck fragmentation divided by statistical emission	6
1.4	Azimuthal distribution of the IMF from the fragmentation of a projectile into two fragments	8
2.1	CAD rendition of a detector telescope	13
2.2	Photo of a telescope	15
2.3	Photo of a 65 μm single sided detector	17
2.4	Photo of a 500 μm double sided detector	18
2.5	Alpha spectrum of a collimated ^{228}Th source	19
2.6	Distributions of measured resolutions for the 65 μm and 500 μm silicon detectors.	20
2.7	Electronic circuit diagram of pre-amplifier	22
2.8	Photo of a pre-amplifier	23
2.9	Functional block diagram of silicon processor module	24
2.10	Functional block diagram of IU pulser	26
2.11	Stability as measured by IU pulser	27
2.12	Functional block diagram of the electronics	28
2.13	Two-dimensional plot of $\Delta E_{65}\text{-EF}_{500}$ before thickness correction of the 65 μm detector	32
2.14	Two-dimensional map of thickness correction factors for 65 μm detector . . .	34

2.15 Two-dimensional plot of ΔE_{65} - EF_{500} following thickness correction of the $65\mu\text{m}$ detector	35
2.16 Two-dimensional plot of ΔEF_{500} -CsI(Tl) for a telescope in LASSA	38
2.17 Isotopic distributions for carbon and oxygen	39
2.18 Light output of CsI(Tl) as a function of Z, A, and E	41
2.19 Percent deviation of the fragmentation and PID calibration data from the respective fits	43
3.1 Cross sectional view of experimental apparatus	48
3.2 Schematic diagram of an individual phoswich detector	49
3.3 Schematic anode signal from the photomultiplier tube of a phoswich detector	50
3.4 "Fast" versus "slow" spectrum measured in ring 13 $\theta_{lab} = 16.6^\circ$	51
3.5 "Tail" versus "slow" spectrum measured in ring 5 $\theta_{lab} = 45^\circ$	52
3.6 Relationship between dial setting on the precision pulser and raw channel number for the calibration of the silicon detectors	54
3.7 Silicon energy calibration with calibration data	55
3.8 Dependence of the energy deposited in the ring detector to the energy deposited in the pie detector.	57
3.9 Distribution of signal leakage into adjacent rings	58
3.10 Distribution of pie energy minus the sum of ring energies	59
3.11 Fits used to determine the mass number of the reaction products	61
3.12 Results of the global fit using Mastinu's procedure	62
3.13 Two-dimensional plot used for the particle identification	64
3.14 One-dimensional spectrum for the particle identification	65
3.15 One-dimensional spectra of the particle identification summed over the entire ring counter	66
3.16 Percent difference in the gain changes of the CsI(Tl) crystals and silicon detectors	68
4.1 Classification of projectile-target collisions based on impact parameter	72
4.2 Measured kinetic energy spectra for Z = 10 to Z = 48 in the reaction $^{114}\text{Cd} + ^{92}\text{Mo}$	73

4.3	Relationship between the energy of the detected fragment and the laboratory angle at which the fragment was detected	74
4.4	Relationship between the atomic number of the detected fragment and the laboratory angle at which the fragment was detected	76
4.5	Multiplicity distribution of fragments detected in the ring counter	77
4.6	Probability distributions for the sum charge for all fragments detected in the ring counter for a given event when one, two or three fragments were detected	78
4.7	Distributions of the charged particle multiplicity, N_c , both inclusive and selected on the number of fragments detected in the ring counter	79
4.8	Dependence of the atomic number, Z , on its laboratory velocity for the case $N_{RC} = 2$	81
4.9	The velocity relationship between the two fragments detected in the ring counter	82
4.10	Dependence of the atomic number on its laboratory velocity when $v_H > v_L$ and $v_L > v_H$	84
4.11	Laboratory angular distribution of both fragments when $v_H > v_L$ and $v_L > v_H$	85
4.12	$\Delta\phi$ distributions of the two fragments in the ring counter	86
4.13	Normalized probability distributions for $Z = 1$ (N_H), $Z = 2$ (N_{He}) and $Z \geq 3$ (N_{IMF}) detected in the MB/MW and LASSA	87
4.14	Dependence of the total charge ($Z_H + Z_L$) of the two fragments detected in the ring counter on N_c	88
4.15	Distributions of the total charge ($Z_H + Z_L$) of the two fragments detected in the ring counter	89
4.16	Dependence of $\langle Z_H + Z_L \rangle$ on N_c	90
4.17	Charge correlation between the two fragments detected in the ring counter selected on both the magnitudes of the fragment velocity and N_c	91
4.18	Relationship of Z_L on v_{rel} selected by fragment velocity and impact parameter	93
4.19	Dependence of $\langle v_{rel} \rangle$ on Z_L for peripheral and mid-peripheral collisions	94
4.20	Relationship of Z_L on Z_H for $Z_H + Z_L$, $Z_H - Z_L$, and η	96
4.21	Dependence of the observed yield on $Z_H + Z_L$, $Z_H - Z_L$ and η and v_{rel}	98
5.1	General features of the $^{114}\text{Cd} + ^{92}\text{Mo}$ reaction	103

5.2	Charge-charge correlation selected by velocity and N_c	105
5.3	Dependence of center-of-mass velocity and $\langle v_{rel} \rangle$ of the two ring counter fragments on multiplicity	107
5.4	Dependence of the yield ratios of Z_L and $\langle v_{rel} \rangle$ on Z_L	109
5.5	Z distributions for peripheral collisions selected on the velocity of the PLF*	110
6.1	Ratio of isotopic yields for fragments with $3 \leq Z \leq 6$ at mid-rapidity as a function of N_c	116
6.2	Comparison of the measured Z distribution with the predicted Z distribution of the SMM model	119
6.3	Comparison of V_{\perp} distributions associated with central collisions for ${}^6\text{Li}$ and ${}^{12}\text{C}$ fragments with the SMM predictions	121
6.4	Relative yield at mid-rapidity for isotopes of Li, B, and C associated with central and peripheral collisions	123
A.1	Plot of the signal and ground traces used in etching the polyimide sheet	131
A.2	Drawing of the cut jig	133
A.3	Drawing of the right half of the bend jig	137
A.4	Drawing of the left half of the bend jig	138
A.5	Drawing of the brass piece used to determine the polyimide's bent length	139
A.6	3-D drawing of the PCB frame used in LASSA	141
A.7	Top view of the PCB frame used in LASSA	142
A.8	Drawing of the base of the glue jig	143
A.9	Drawing of the plate used for the epoxying of the front cable	144
A.10	Drawing of the plate used for epoxying of the back cable	145
A.11	Drawing of the bar used for holding the PCB frame in place in the glue jig	146
C.1	Drawing of the setup used to test the nominal $30 \mu\text{m}$ detectors	159
C.2	Typical degraded alpha spectrum as measured by the surface barrier detector	161
C.3	Thickness of the nominal $30 \mu\text{m}$ detectors as a function of position	162
C.4	Percent thickness variation of the $30 \mu\text{m}$ detectors tested	163
C.5	Percent thickness difference from the quoted value of the $30 \mu\text{m}$ detectors	164

List of Tables

2.1	Comparison of the characteristics of different FET's tested in the LASSA preamp circuit.	22
2.2	Secondary beams produced by projectile fragmentation of ^{16}O used in the calibration of LASSA.	30
2.3	Secondary beams produced by projectile fragmentation of ^{36}Ar used in the calibration of LASSA.	31
2.4	Nominal and deduced thicknesses of the $500\ \mu\text{m}$ LASSA Si strip detectors. .	36

Chapter 1

Introduction

One of the interesting questions in the study of many-body systems is the character of multi-particle correlations between the constituent particles. It is well established that the average behavior of a multi-particle system, such as nucleus, is well described within a mean field approach. The success of such an approach in the case of nuclei is validated by the excellent description of nuclear spectra and binding energies by the nuclear shell model. Nucleons are assumed to move independent of each other in the mean field generated by all the nucleons [1]. Such mean field descriptions have proven valuable in describing physical phenomena in atomic and molecular systems as well. Although many properties of many-body systems can be understood within a mean field approach, other phenomena such as clustering require consideration of multiparticle correlations [2]. In the case of nuclei, clustering is well established [3, 4]. Light nuclei such as ^{12}C and ^{16}O are well known to exhibit “alpha clustering”, that is, they behave as if they were composed of three or four alpha particles, respectively, rather than the constituent neutrons and protons [5]. Investigation of cluster formation within the nuclear medium therefore presents an opportunity to examine these in-medium correlations. In addition, the dependence of clusterization on density and temperature is poorly known. While cluster formation may have a significant probability in the ground state, as the temperature of the nucleus increases, the probability that the clusters break increases. However, the higher temperature results in an increased probability that a cluster can overcome the emission barrier and be emitted. In contrast, nuclear matter at reduced density might manifest both an increase in clusterization (reduced impact of Pauli blocking) and increased emission due to a reduced emission barrier, which also can increase

the probability of a cluster being emitted.

Clusters can be emitted from slightly excited nuclei following fusion reactions in a process describable as evaporation. While this evaporation of simple clusters has been addressed within a statistical framework, all such models rely on the pre-formation of the cluster within the medium and in reality only treat the particle emission within a transition state theory. Thus, the more difficult (and interesting) question of the composite particle aggregation is not addressed.

Clusters may also result from shape instabilities of the nuclear drop during fission [6, 7, 8]. These instabilities can be understood if the nucleus is modeled as a liquid drop. In 1878 Lord Rayleigh demonstrated that a long cylindrical fluid jet could separate into droplets [9]. The primary factor influencing the breakup was that the individual droplets had a larger surface energy as compared to the cylindrical jet. The disassembly of the jet into droplets required perturbations along the surface of the fluid that satisfied the expression:

$$\lambda \geq 2\pi r_o \quad (1.1)$$

when the wavelength of the perturbation, λ , was greater than the mean circumference of the jet, $2\pi r_o$. A diagram of this instability is depicted in Fig. 1.1. The presence of the Rayleigh instability for a small system consisting of a few hundred constituent particles, i.e. a nucleus, has been well established [6]. One means to study the influence of deformation (perturbations) on cluster emission is to study fragment emission from non-spherical geometries of nuclear matter by producing transient, non-spherical geometries using the non-central collision of two heavy-ions.

Cluster emission from a deformed nucleus was first observed in the fission of heavy nuclei having little (neutron-induced fission of ^{235}U and ^{239}Pu [10]) or no (spontaneous fission of ^{252}Cf [11]) excitation. In these experiments, while the coincidence of the cluster with the fission was established, whether the cluster emission preceded, followed, or was concurrent with the fission was not apparent. The emission of clusters occurring near or at the scission point was first proposed by San-Tsiang [12]. Subsequently, Gazit's analysis of the angular and energy distributions from the triple coincidence of two fission fragments and an alpha particle from the thermal-neutron induced fission of ^{235}U [13] confirmed San-Tsiang's hypothesis.

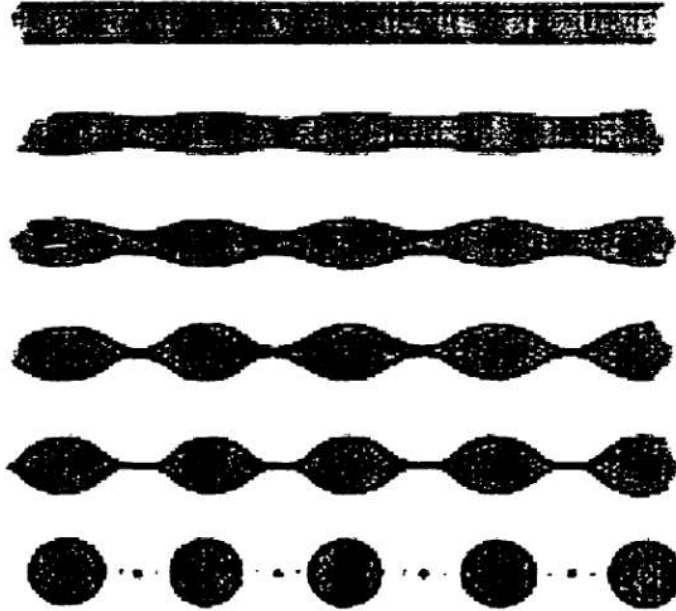


Figure 1.1: Pictorial representation of the Rayleigh instability of a fluid jet.

The investigation of cluster emission was extended to more symmetric systems at incident energies of $E/A = 5-10$ MeV by utilizing the mid-central collision of two heavy-ions in a strongly damped (deeply inelastic) collision [14] – [18]. In this energy domain, the reactions involve the binary collision of projectile and target nuclei during which mass and energy are exchanged between the two nuclei yielding an excited target-like fragment (TLF*) and projectile-like fragment (PLF*). These two reaction products have mass number and atomic number similar to the original projectile and target nuclei but with significant velocity damping [19]. The interaction time is less than one revolution resulting in a characteristic angular distribution. As kinetic energy of relative motion is transferred into intrinsic excitation during the collision, the excited di-nuclear system can decay *via* the emission of neutrons, protons, or complex clusters. After separation the TLF* and PLF* accelerate away from each other due to their mutual Coulomb repulsion and each can subsequently de-excite by emission of neutrons, protons, or clusters.

The predominant cluster detected in the early work utilizing strongly damped collisions was the alpha particle. Wilcke *et al.* [20] reported the preferential emission of alpha particles

perpendicular to the separation axis from a heavy-ion-induced fusion-fission reaction of $^{56}\text{Fe} + ^{165}\text{Ho}$ at $E/A = 8.3$ MeV. From their examination of angular distributions and kinetic energy spectra, Wilcke *et al.* concluded that the experimental observations could not be understood as evaporation only from the fused projectile and target and the subsequent statistical decay of a PLF* and TLF*. The observed emission pattern could be explained if the alpha emission occurred from “the neck region of the highly deformed nucleus” [20].

Emission of larger clusters having atomic numbers between $3 \leq Z \leq 10$, also referred to as intermediate mass fragments (IMF), were examined by Toke *et al.* This investigation focused on IMF emission following peripheral collisions in reaction $^{136}\text{Xe} + ^{209}\text{Bi}$ at $E/A = 28$ MeV [21]. The low excitation energies and well-known binary mechanisms of peripheral collisions from previous studies facilitated the analysis of the emitted IMF's. As depicted in Fig. 1.2 the data indicated clearly that a majority of the IMF's were emitted with velocities between the PLF* and the TLF*. The theoretical velocities of the TLF* and PLF* are indicated by the arrows. Further analysis of the data demonstrated that the IMF's had a significant in-plane anisotropy with the TLF* and PLF*. These observations led Toke *et al.* to infer that the emission of IMF's was dynamically produced in the region between the PLF* and TLF*.

Contemporaneous with the work of Toke *et al.*, Montoya investigated the influence of the decaying system shape on the IMF emission process. In their analysis of the asymmetric system $^{129}\text{Xe} + ^{\text{nat}}\text{Cu}$ at $E/A = 50$ MeV [22], relative velocity distributions between the PLF and IMF were examined. These distributions were decomposed into two components: a statistical component and a non-statistical component. To calculate the statistical component, the experimental data having emission patterns consistent with statistical decay were compared to a model. The statistical yield was subtracted from the total yield to obtain the non-statistical yield. Based upon the IMF angular distributions, Montoya *et al.* arrived at the same results as Toke *et al.* that the IMF was emitted preferentially between the PLF and TLF. The non-statistical emitted fragments were found to have an enhanced yield as compared to the statistical yield for $4 \leq Z \leq 12$ with a maximum yield at $Z = 7$ as depicted in Fig. 1.3. Comparing the experimentally derived yields to a percolation model, they proposed that this IMF yield distribution could be understood in terms of the breakup of a cylindrical neck joining the PLF* and TLF*. Thus, they attributed the observed yield

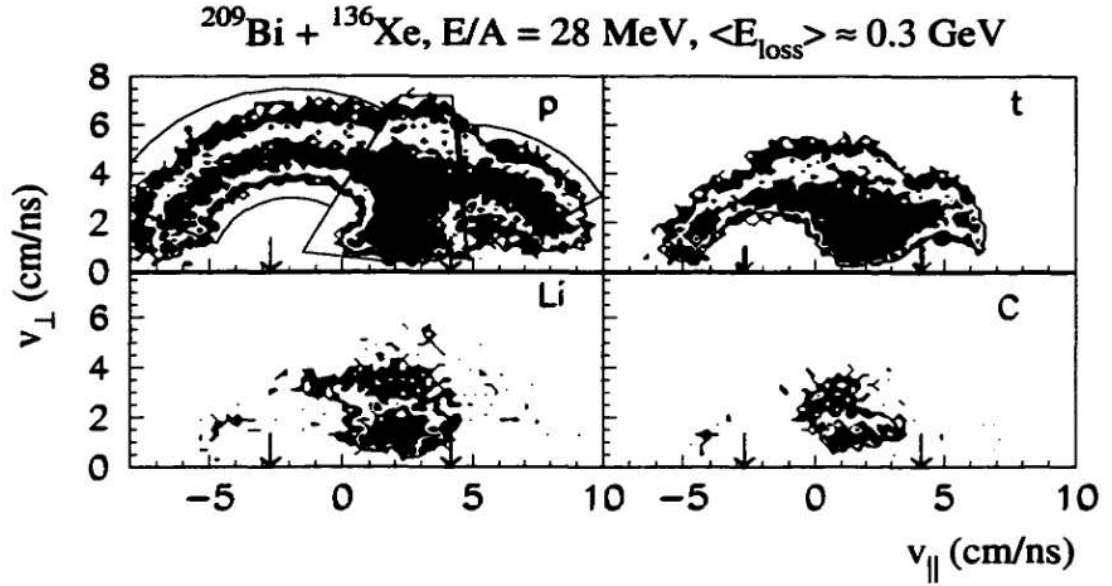


Figure 1.2: Galilean-invariant emission patterns of light charged particles and IMF's coincident with PLF's from peripheral collisions. Arrows demote theoretical source velocities. From Ref. [21].

distribution of the non-statistical component to a geometrical constraint.

Bocage *et al.* have recently extended the early work of Montoya and Toke with a systematic study of fragment emission in peripheral and mid-central collisions. They have investigated several projectile-target combinations ranging from asymmetric to symmetric collisions over a broad range in incident energy [23]. Charge asymmetric projectile-target combinations (*e.g.* light-projectile bombarding a heavy target) decayed in a manner consistent with fission of a hot, heavy system, i.e. a charge distribution peaked at symmetry. For more charge-symmetric collisions, however, an additional yield in the charge distribution, notably the creation of charge-asymmetric products was observed. To understand the nature of this additional yield, the distribution of the angle between the direction of the PLF* velocity and the breakup axis was examined. This angular distribution was peaked, indicating that the decay of the PLF* was aligned with the TLF. The smaller fragment from the decay of the PLF* was located between the larger fragment and the TLF*. Bocage *et al.* refer

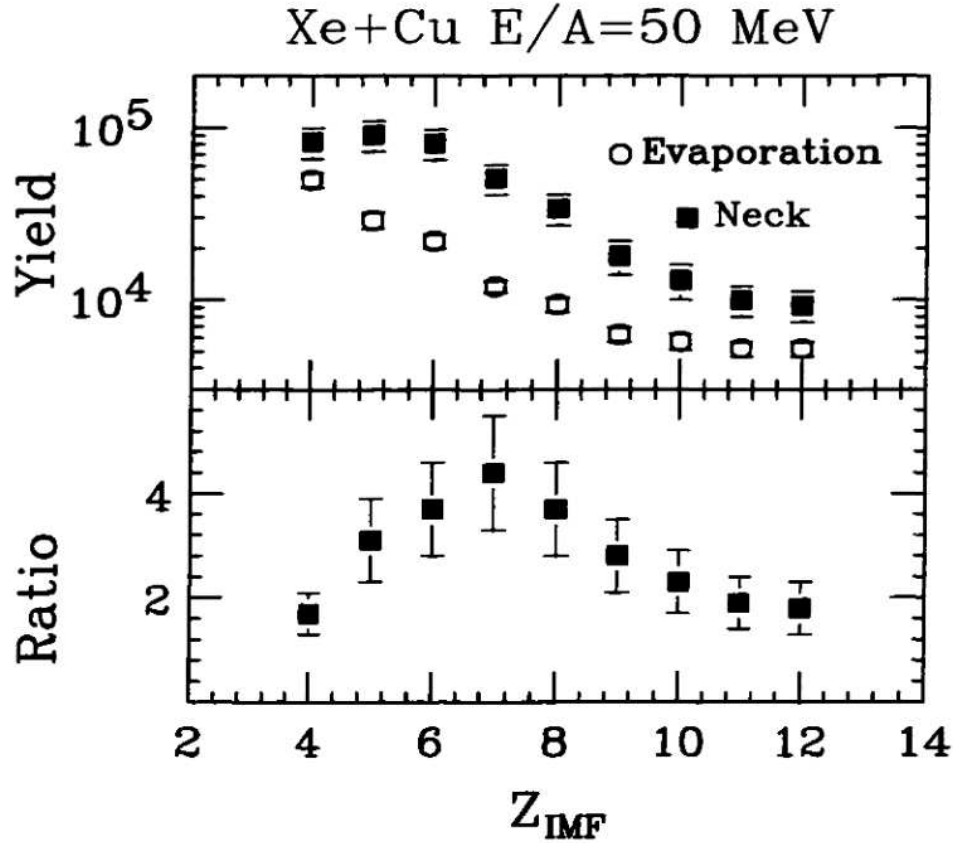


Figure 1.3: Ratio of the measured yields of neck fragmentation divided by statistical emission. From Ref. [22].

to this process as “aligned fission”. The conditions which appear to influence the “aligned fission” most strongly are the larger charge asymmetry of the detected fragments, symmetry of the projectile-target combination, and the centrality of the collision. To characterize the standard fission and the aligned fission components further, the relationship between the average relative velocity and charge asymmetry was investigated. The average relative velocity of the standard fission component was reasonably well described by an approximate Coulomb calculation which utilized the atomic number, radii and reduced mass of the two fission fragments. The aligned fission component, however, had a significantly larger average relative velocities as compared to the calculation. From these results Bocage *et al.* proposed

that for aligned fission the interaction of the projectile and target deforms the projectile and this deformation induces the breakup of the projectile.

As can be seen from the work of Toke and Bocage, both neck fragmentation and PLF* breakup resulting in IMF production have largely been attributed to a dynamical process. Recently, Botvina *et al.* have proposed an alternative explanation for the emission of IMF's at velocities intermediate between the PLF and TLF [24]. In this model, the Coulomb field of the TLF* influences the decay of the PLF*. Shown in Fig. 1.4 is the significant influence of the TLF* Coulomb field has on the decay of the PLF*. The dotted line represents breakups with no Coulomb field, whereas the solid line represents the TLF* Coulomb influence. This Coulomb proximity effect favors asymmetric breakups and emission of the smaller fragment toward the TLF*. Rigorous comparison of this proposed explanation has not yet been made.

Another factor possibly influencing fragment emission at velocities intermediate between the PLF and TLF is the isospin instability of nuclear matter. Asymmetric nuclear matter can undergo an isospin fractionation – it is thermodynamically favorable for the low-density region to be neutron-rich and the high-density region to be proton-rich [25]. As the neck is a region of lower density, it might be susceptible to isospin fractionation, i.e. the emission of fragments at mid-velocity might be driven by an isospin instability.

To explore the process of fragment emission at velocities intermediate between the PLF and TLF, a compact, high granularity, low-threshold detector array was constructed. In order to probe the isotopic composition of the emitted fragments for which limited information was previously available, a principal feature of this array is its ability to isotopically identify fragments with $Z \leq 9$. This array of nine independent telescopes was based upon silicon-strip technology to meet the design criteria. A description of the design and construction of the Large Area Silicon Strip Array (LASSA) constitutes a major fraction of this thesis.

The remainder of this thesis is organized as follows: Chapter 2 describes the design, construction and testing of LASSA. Chapter 3 depicts the experimental setup and describes the calibration of the three detector arrays used in the study of the reaction $^{114}\text{Cd} + ^{92,98}\text{Mo}$ at $E/A = 50$ MeV. General reaction characteristics of PLF decay in this reaction are presented in Chapter 4. In Chapter 5 charge correlations, relative yields, and average relative velocities for the PLF* decay are investigated. The isospin of mid-velocity fragments for peripheral and central collisions is examined in Chapter 6. The conclusions for this thesis are

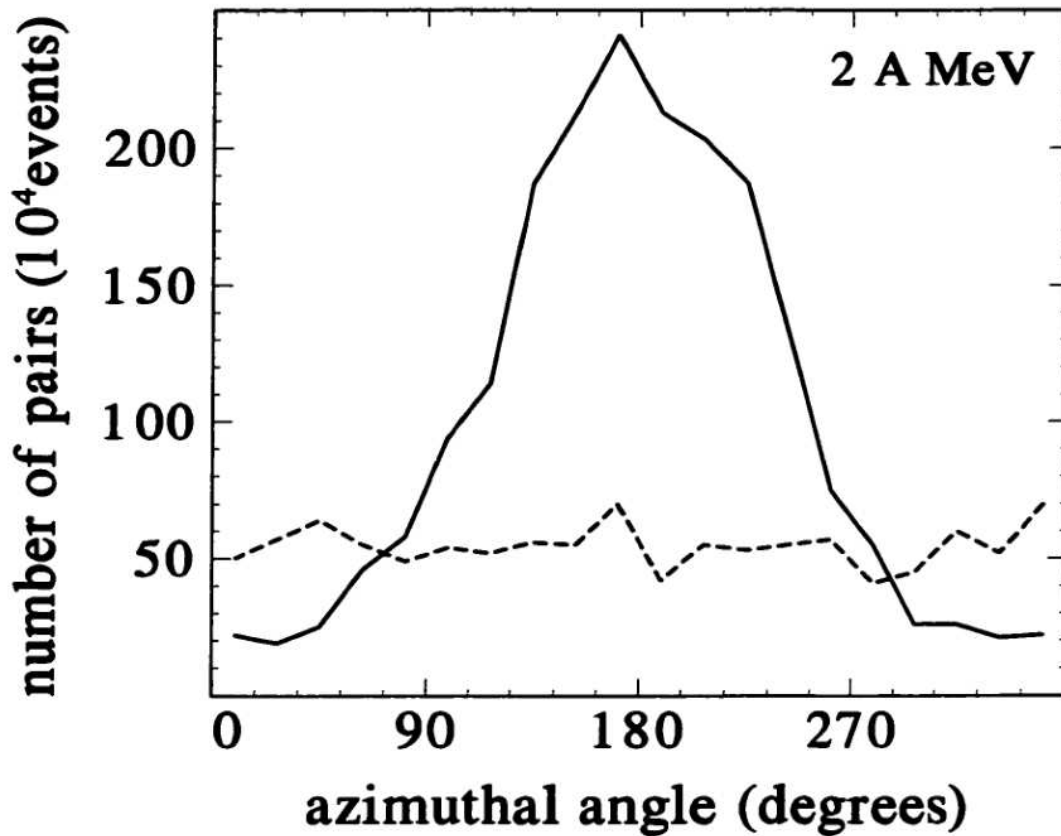


Figure 1.4: Azimuthal distribution of the IMF from the fragmentation of a projectile into two fragments. The solid line depicts the Coulomb influence of the target source and the dashed line is without the influence. From Ref. [24].

presented in Chapter 7. Details relevant to the initial design, construction and operation of LASSA are contained in the Appendices. Appendix A describes the procedure to fabricate a frame assembly for holding the silicon detector. The data format and relevant programs used in the analysis are described in Appendix B. The testing of very thin ($30 \mu\text{m}$), single area silicon detectors which preceded the LASSA project is detailed in Appendix C.

References

- [1] W. Nörenberg and H.A. Weidenmüller, *Lecture Notes in Physics: Introduction to the Theory of Heavy-Ion Collisions*, edited by J. Ehlers *et al.* (Springer-Verlag, Berlin, Heidelberg and New York, 1980), Vol.51, and references therein.
- [2] J. Schmelzer, G. Ropke, and R. Mahnke. *Aggregation Phenomena in Complex Systems*. Weinheim/Berlin/New York: WILEY-VCH, 1999.
- [3] M.F. Werby *et al.*, *Phys. Rev. C* **8**, 106 (1973).
- [4] A.M. Young *et al.*, *Phys. Rev. Lett.* **25**, 1764 (1970).
- [5] J. Wheeler, *Phys. Rev.* **52**, 1083 (1937).
- [6] U. Brosa and S. Grossmann, *Phys. Lett.* **126B**, 425 (1983).
- [7] U. Brosa and S. Grossmann, *Z. Phys. A* **310**, 177 (1983).
- [8] U. Brosa and S. Grossmann, *J. Phys. G* **10**, 933 (1984).
- [9] J. Rayleigh, *Proc London Math. Soc.* **10**, 4 (1878).
- [10] G. Farwell *et al.*, *Phys. Rev.* **71**, 327 (1947).
- [11] S.L. Whetstone Jr. and T.D. Thomas, *Phys. Rev. Lett.* **15**, 298 (1965).
- [12] T. San-Tsiang, *J. Phys. Radium* **9**, 6 (1949).
- [13] Y. Gazit *et al.*, *Phys. Rev. C* **4**, 223 (1971).
- [14] E. Duek *et al.*, *Phys. Lett.* **131B**, 297 (1983).
- [15] L. Schad *et al.*, *Z. Phys. A* **318**, 179 (1984).
- [16] B. Lindl *et al.*, *Z. Phys. A* **328**, 85 (1987).
- [17] A. Brucker *et al.*, *Phys. Lett.* **186B**, 20 (1987).
- [18] R. Lacey *et al.*, *Phys. Rev. C* **37**, 2540 (1988).

- [19] W.U. Schroeder and J.R. Huizenga, in *Treatise in Heavy-Ion Science*, edited by D.A. Bromley (Plenum Press, New York and London, 1984), Vol.2, p. 113, and references therein.
- [20] W.W. Wilcke *et al.*, *Phys. Rev. Lett.* **51**, 99 (1983).
- [21] J. Toke *et al.*, *Phys. Rev. Lett.* **75**, 2920 (1995).
- [22] C.P. Montoya *et al.*, *Phys. Rev. Lett.* **73**, 3070 (1994).
- [23] F. Bocage *et al.*, *Nucl. Phys.* **A676**, 391 (2000).
- [24] A. S. Botvina *et al.*, *Phys. Rev. C* **59**, 3444 (1999).
- [25] H. Müller and B. Serot, *Phys. Rev. C* **52**, 2072 (1995).

Chapter 2

LASSA: A Large Area Silicon Strip Array for Isotopic Identification of Charged Particles

2.1 Introduction

It has been recently proposed that the thermodynamic properties of nuclear matter (the nuclear equation-of-state) are sensitive to the N/Z degree of freedom. Theoretical calculations [1] suggest that characterizing the N/Z of fragments formed in a low-density medium, in contrast to the N/Z of fragments emitted from normal density nuclear matter, could provide important information about the nuclear equation-of-state. Dynamical properties (*e.g.* deflection functions) of the transient systems used to create excited nuclear matter are also influenced by the N/Z of the two colliding nuclei [2]. Initial experimental and theoretical work on N/Z equilibration [3] - [8] at intermediate energies demonstrates clearly the dynamical and non-equilibrium nature of the short-lived systems formed. More detailed studies, however, require isotopic identification of fragments over a substantially broader range of Z , energy, and angle than is presently possible. In addition, these measurements must be carried out with both good energy and angular resolution in order to investigate multi-particle correlations.

2.2 Design Constraints

The requirements of good energy resolution ($\leq 1\%$), for isotopic identification of intermediate mass fragments (IMF: $3 \leq Z \leq 20$), and of good angular resolution ($\theta \leq 1^\circ$), mandate the use of a telescope based upon a semiconductor detector. In addition, if segmented, such devices provide the capability of multiple particle detection at small relative angles within a single telescope.

In order to provide low identification thresholds for low velocity, highly ionizing particles, a $65 \mu\text{m}$ Si strip detector was selected to be the first element of the telescope, resulting in a threshold of $\sim 2.5 \text{ MeV/u}$ for ^4He and $\sim 5 \text{ MeV/u}$ for ^{16}O . The strips served to both reduce the capacitance of each detector element and to provide position resolution within a single telescope. Energy measurement of high velocity light charged particles (p, d, t, ^3He , ^4He , and ^6He) necessitated use of a scintillator for which we chose CsI(Tl) crystals, 6 cm thick, read out by photodiodes (PD). This crystal thickness results in a maximum identification energy of $E/A = 140 \text{ MeV}$ for protons and $E/A = 335 \text{ MeV}$ for ^{16}O ions. To measure the scintillation caused by the charged particle striking the CsI(Tl) crystal, we elected to use a photodiode due to its characteristics of excellent linearity over a wide dynamic range, stability over long durations, and compact size. The PD chosen was the Hamamatsu S3204 [16], a 2 cm x 2 cm photodiode. The maximum count rate of such a Si-CsI(Tl)/PD telescope is limited, by the long decay constant of the CsI(Tl), to a few kilohertz in order to avoid pile-up in the CsI(Tl) crystal. This rate was sufficient for all the intended experiments. Since energetic light particles deposit very little energy in the $65 \mu\text{m}$ Si, thus making particle identification by the ΔE -E technique difficult, a second thicker Si strip detector in front of the CsI(Tl) was also necessary. The arrangement of the double-stack of Si backed by CsI(Tl)/PD used in LASSA is shown in Fig. 2.1. This telescope is designed to operate in high vacuum ($P \sim 1 \times 10^{-6}$ torr) with minimal outgassing.

The silicon detectors used in LASSA are ion-implanted, passivated devices, Si(IP), (Design W) obtained from Micron Semiconductor [18]. The first detector of the stack is nominally $65 \mu\text{m}$ thick. The second Si detector is either $500 \mu\text{m}$ or 1 mm thick depending on the focus of the experiment. The 1 mm Si detector has strips on the front surface (junction side) only while the $500 \mu\text{m}$ detector has strips on both front (junction) and rear (ohmic) surfaces

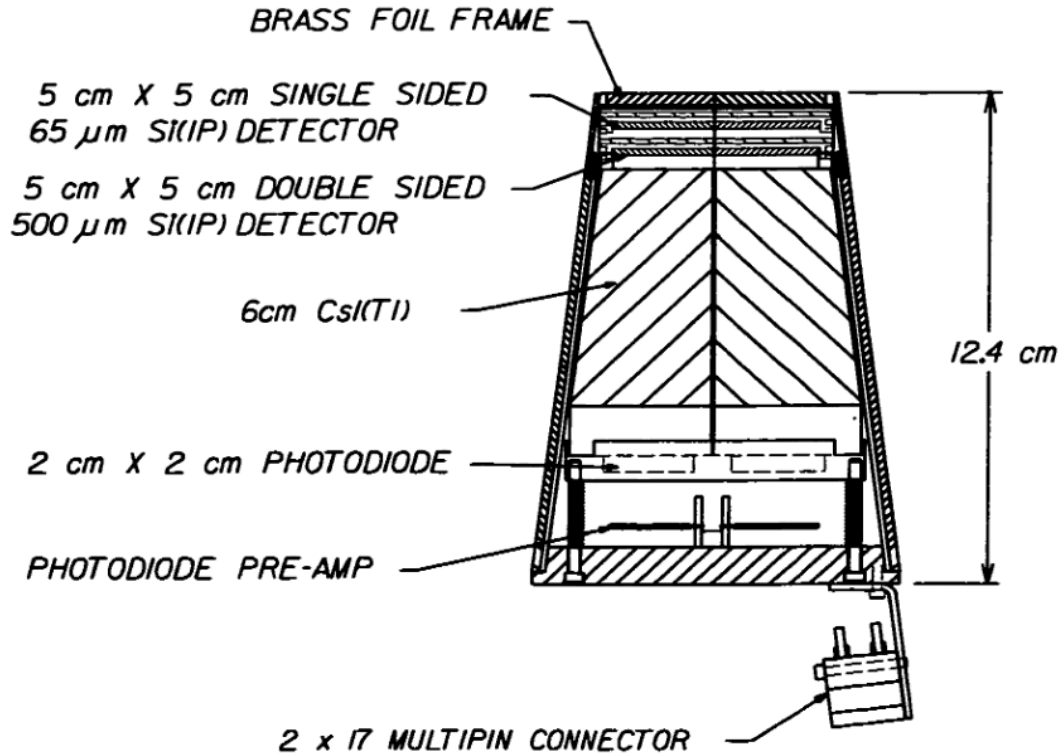


Figure 2.1: CAD rendition of a detector telescope (cross-sectional view).

in orthogonal directions, allowing two-dimensional position information from this detector alone. When the 1 mm detector is utilized, its strips are oriented orthogonal to the strips in the 65 μm in order to provide two-dimensional position resolution for this configuration. The pitch of the strips (nominally 3 mm with an interstrip SiO_2 isolation of 100 μm) was chosen in order to maintain a modest value of capacitance ($\sim 250\text{-}300$ pF/strip) for the thin (65 μm) detector. At the design target-telescope distance of 20 cm, the angular resolution of a strip is $\Delta\theta \sim 0.9^\circ$.

The entire detector assembly was housed in two separable aluminum boxes of a trapezoidal geometry. These boxes were designed to provide mechanical support, relative alignment, and electromagnetic shielding of the detectors and photodiode pre-amplifiers, as shown in Fig. 2.1. The housing was designed and fabricated to contribute as minimally as possible

to the dead area of a detector. The total active area of a detector is $\sim 75\%$. The inactive area of 25% is divided among the interstrip region (3%), the SiO₂ border on the wafer itself (7.3%), the printed circuit board frame that holds the Si wafer (6.7%), and the aluminum can (8.0%).

The detachable nature of the front Si box and the back CsI(Tl)/PD box allows easy access to either section. In Fig. 2.2, two sides of both the Si box and the CsI(Tl)/PD box have been removed to show the internal mounting structure. The CsI(Tl)/PD box is mounted on a brass flange from which the relative alignment of all active elements of the telescope is determined.

2.3 Si Detectors

2.3.1 Mechanical Mounting and Electrical Contacts

Since several of the experiments for which LASSA was designed require close packing of the telescopes in the array, it was necessary to minimize the dead area surrounding each Si wafer. The commercially available detector frame for a Design-W detector did not allow close packing of the telescope. Therefore, a new frame was designed in which the Si wafer is epoxied into a frame made out of printed circuit board (G-10) with a recessed well. Only 1 mm of this detector frame extends beyond the physical dimension of the Si wafer. This 1 mm border is responsible for the loss of 6.7% of the active area. The challenge of such a minimal detector frame was the extraction of the 16 (or 32 for a double-sided detector) signals. This problem was overcome by the "in-house" development of a flexible cable that is attached permanently to the frame with a low volatility epoxy (Ablestik 84-3) [17] to form an integrated package. The flexible cable provides gold plated pads (0.062 in. x 0.030 in.) in the plane of the Si wafer, thus allowing automated wire bonding of the cable to the Si strips.

The flexible cable was fabricated by first printing the desired pad and trace pattern on a sheet of polyimide covered on one side with rolled annealed copper (R/flex 1000L810) [19] and subsequently etching it, bending it, and epoxying it to the printed circuit board detector frame. The polyimide is 0.001 inches thick with a copper thickness of 0.001 inches. (Sheets of electro-deposited copper proved unsatisfactory as they cracked during the bending stage

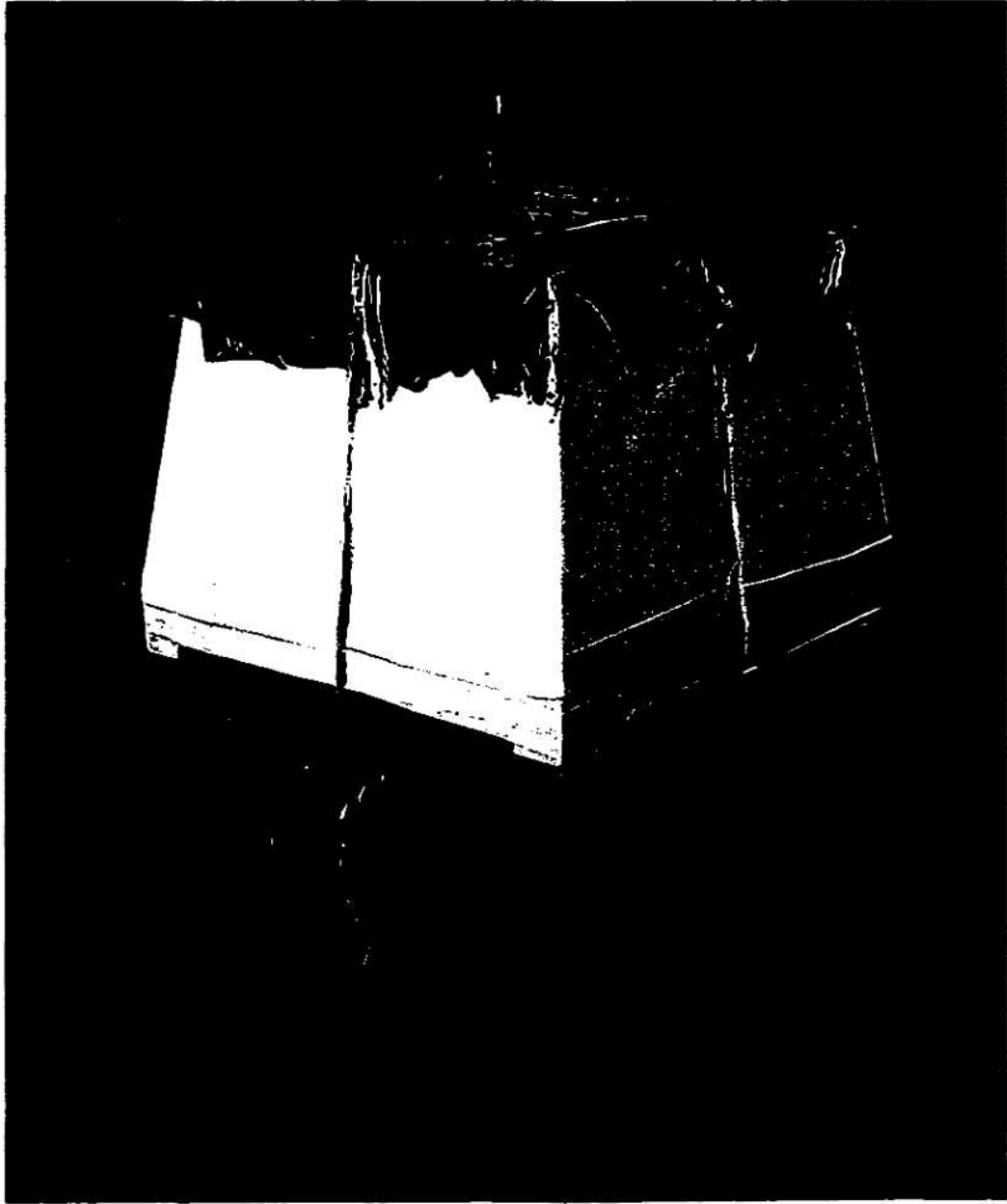


Figure 2.2: Photo of a telescope with Si-Si section partially removed from the CsI(Tl)/PD section.

of the fabrication process.) After printing the desired pad and trace pattern, the sheet was then etched using a DirectImaging plotter/etcher [20]. Next, the cable was laminated with a 0.001 inch thick polyimide protective cover (R/flex 1000C110) on the copper-clad side to prevent accidental shorting of signals. The lamination was achieved by sandwiching the cable and its cover between two 1-inch thick steel plates at a temperature of 175 °C for 1.5 hrs. The resulting cable was then bent with a precision bending fixture and epoxied to the G-10 detector frame. At the other end of the cable, another printed circuit board was attached to allow subsequent mounting of a multipin connector. The entire assembly was cured in an oven for 2 hrs at a temperature of 125 °C. Following a thorough mechanical and electrochemical cleaning, nickel (SIFCO 2080) and then gold (SIFCO 3024) [21] were electroplated onto the pads using a brush plating technique (*e.g.* 19 V, 15 mA, 8 minutes for the gold). Finally, the IDC 34 pin connector (3M 3431-2303) was soldered on. Closeup views of the Si-flexible cable assembly for both the single-sided 65 μm and double-sided 500 μm detectors are provided in Figs. 2.3 and 2.4, respectively.

2.3.2 Measurement of Silicon Resolution and Depletion Voltage

Upon delivery of the Si(IP) detectors from Micron Semiconductor, the energy resolution of each strip was measured by scanning the detector with a collimated ^{228}Th α -particle source. A typical spectrum, obtained at $\sim 28^\circ\text{C}$, is shown in Fig. 2.5. The strip resolution was recorded based on the FWHM of the 6778 keV peak. (Typical resolution of the two end strips was sometimes worse due to the absence of a guard ring to ensure better voltage isolation for these terminal strips.) Leakage currents upon delivery varied from 0.420 to 9.55 μA for the 500 μm detectors. Large leakage currents, indicative of a low resistance path to ground, generally correlated with poorer resolution. A compilation of the observed FWHM of all the detectors is depicted in Fig. 2.6. It should be noted that the strip resolution shown in Fig. 2.6 includes the electronic noise of the test setup. Typically, the electronic noise was 30 keV as measured using a precision pulser. Thus, the most probable resolution of 75 keV measured for a 65 μm detector corresponds to an intrinsic resolution of 69 keV. In Fig. 2.6, it can also be noticed that the resolution distribution of the back (ohmic side strips) exhibits a tail on the poor resolution side. We hypothesize that this poorer resolution (of some detectors) may be due to lower inter-strip isolation on the ohmic side, inherent to

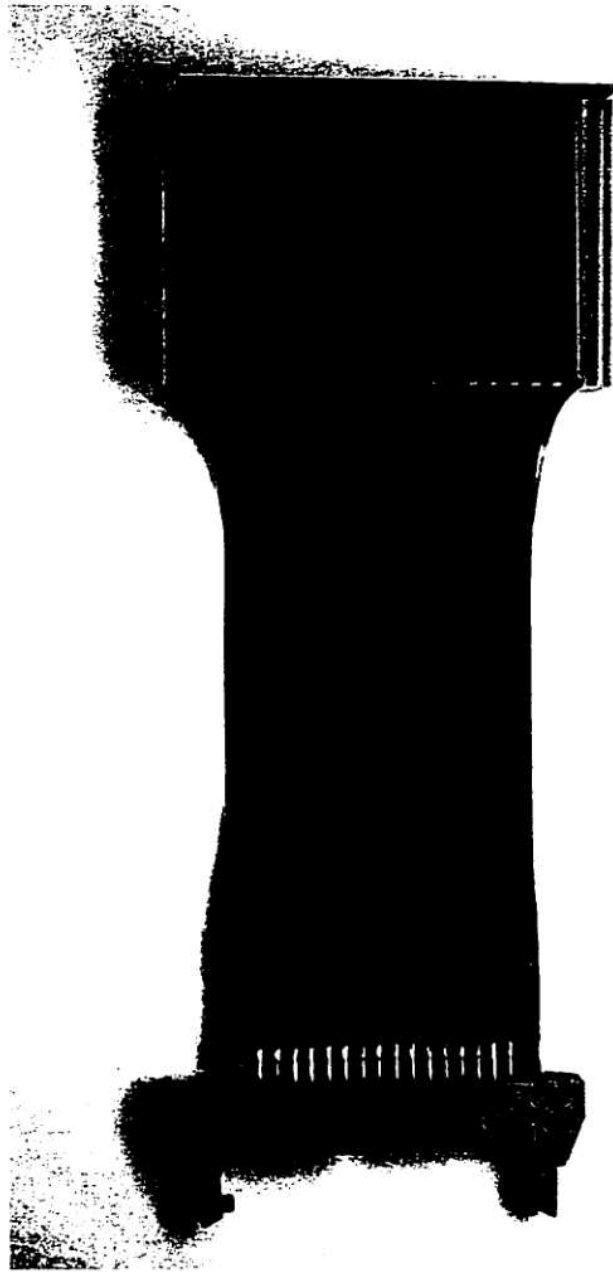


Figure 2.3: Photo of a 65 μm single sided detector.

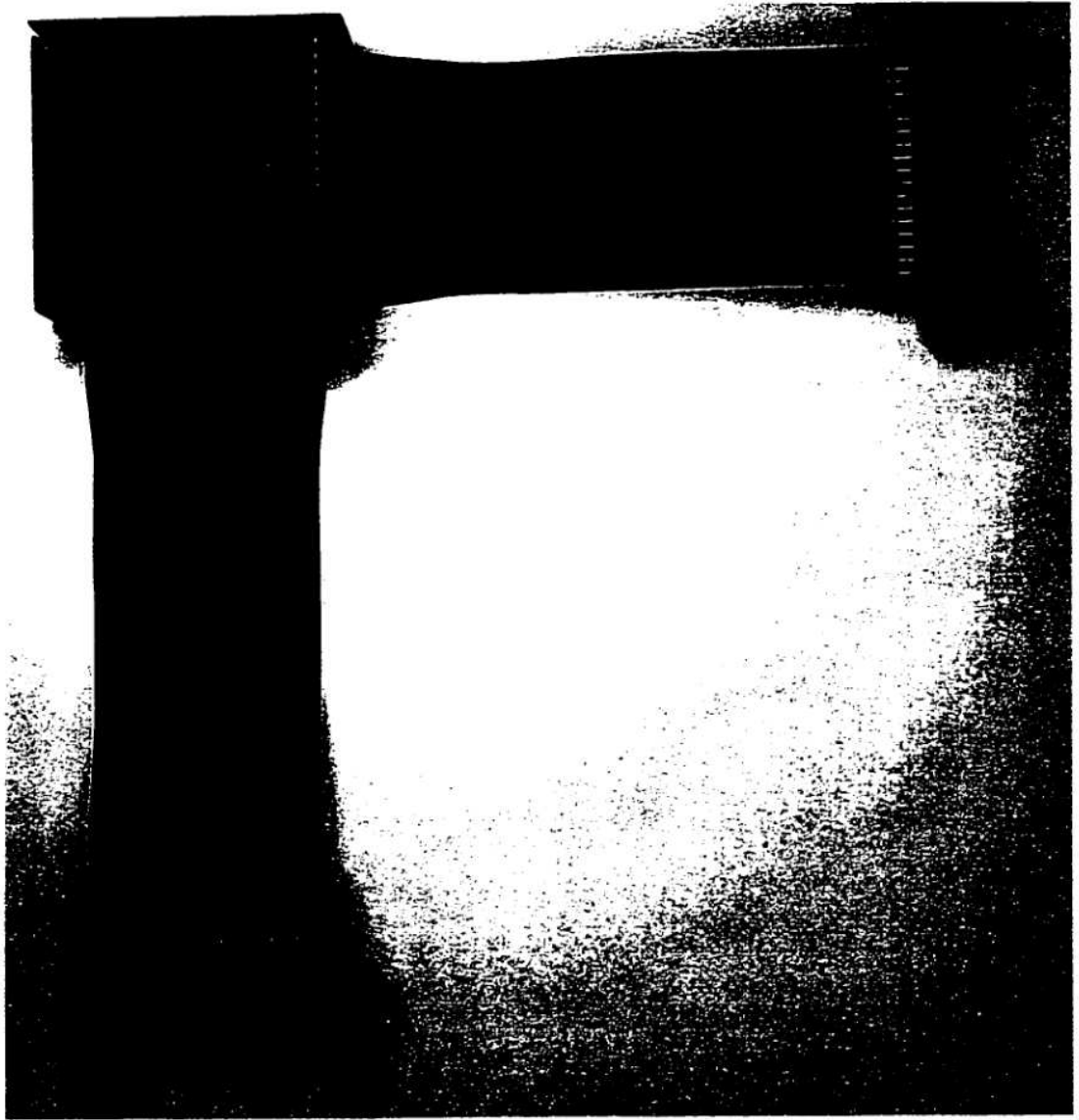


Figure 2.4: Photo of a 500 μm double sided detector.

the fabrication process, leading to charge leakage to adjacent strips. Use of implanted p^+ isolation strips between adjacent strips on the ohmic side can improve inter-strip isolation.

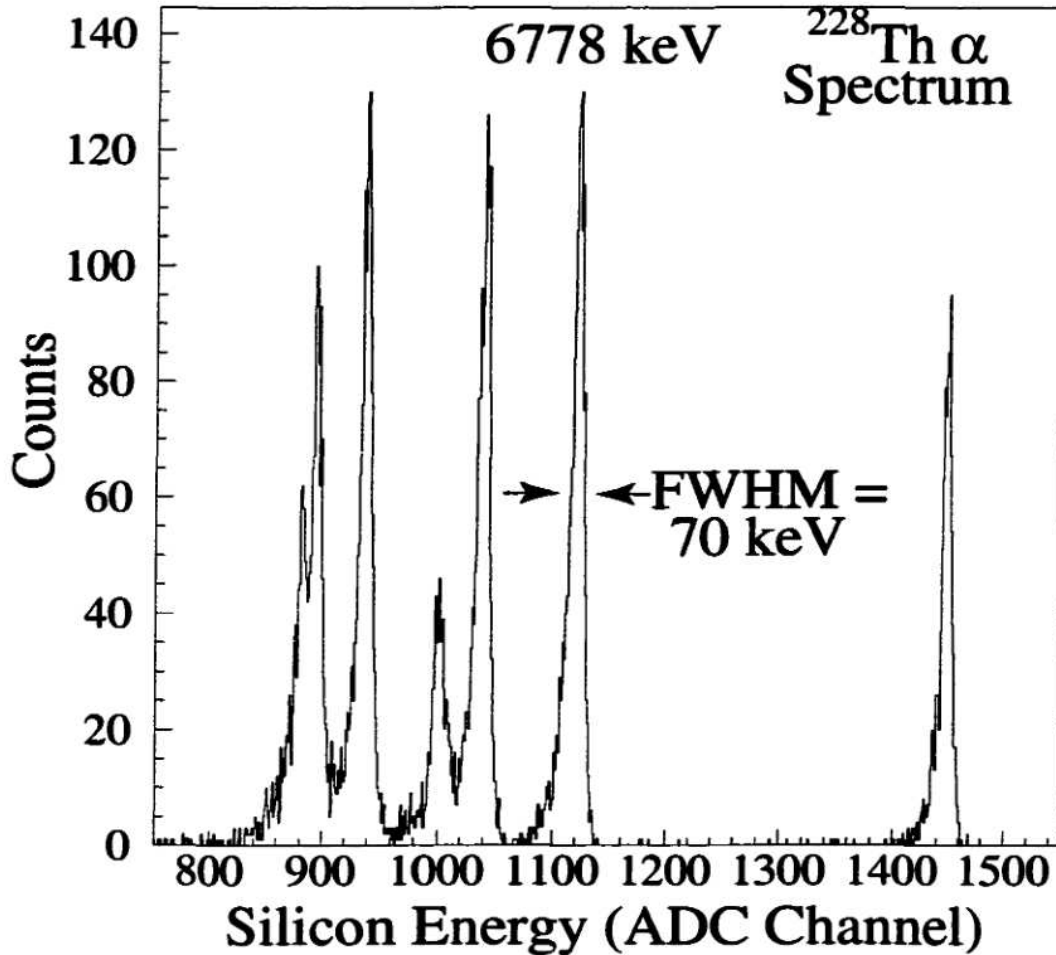


Figure 2.5: Alpha spectrum of a collimated ^{228}Th source in one strip of a LASSA detector.

As it is necessary to fully deplete the detectors in order to achieve complete charge collection, we measured the full depletion voltage for each detector. This voltage was determined by injecting an α particle into the rear surface and maximizing the collected charge as a function of the applied bias. Dead layers on similar detectors have been previously measured [22] to range between 0.5-0.75 μm Si equivalent.

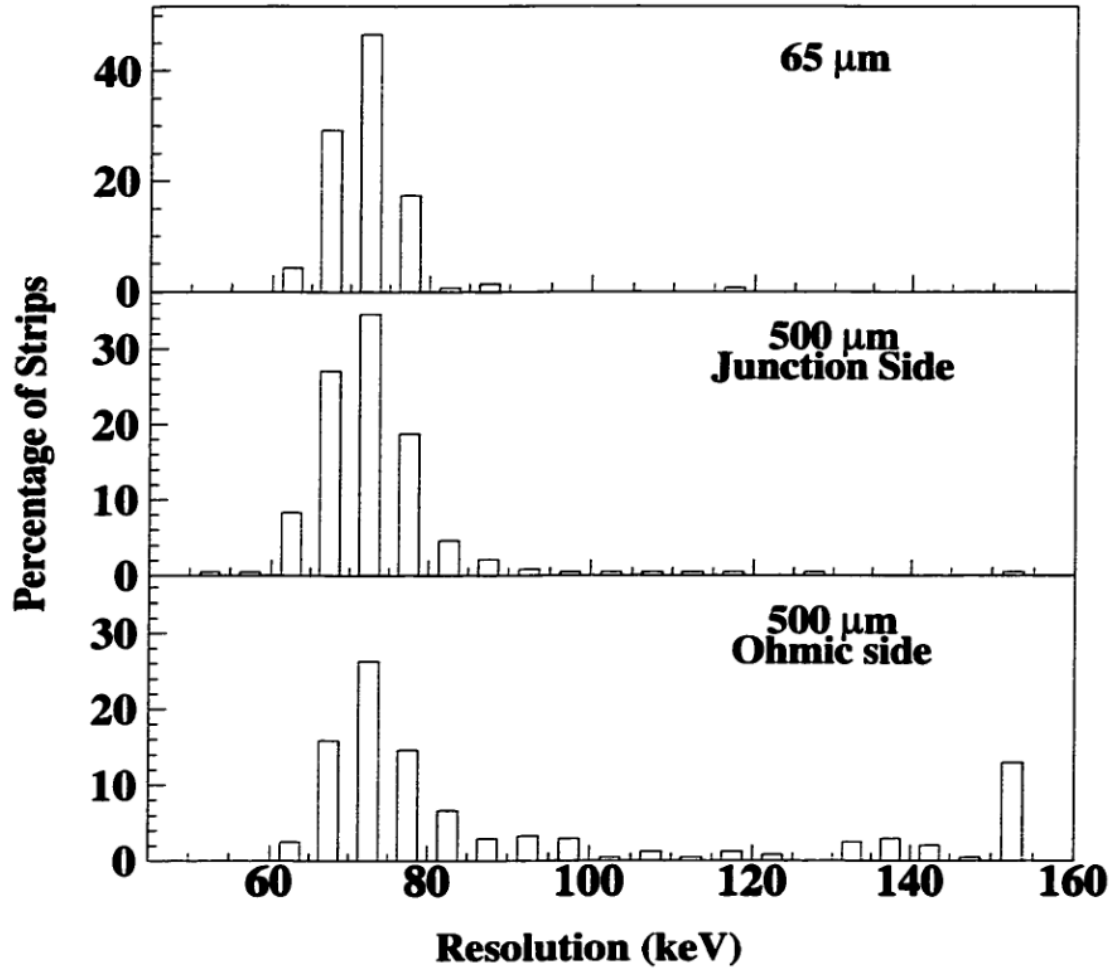


Figure 2.6: Distributions of measured resolutions for the 65 μm and 500 μm silicon detectors.

2.4 Electronics

A crucial aspect of this project was the ability to maintain the good energy resolution possible with a Si(IP) detector in any associated electronics. The large number of Si channels in LASSA (432) mandated the development of a low-cost, high-density pre-amplifier. Based upon Monte Carlo energy loss calculations, which included straggling, and our design constraint of isotopic resolution up to and including oxygen, we determined the necessary energy resolution to be $\delta E/E = 60 \text{ keV} / 6 \text{ MeV}$ for α particles. Maintaining this design con-

straint for the 432 Si channels of LASSA required that the charge integrating pre-amplifier be capable of operating in vacuum adjacent to the detectors, so as to minimize the influence of cable capacitance.

The large number of channels in LASSA also required development of an integrated shaper/discriminator module that would allow easy control of the LASSA signals (*e.g.* gain of the slow output and discriminator threshold). It is also vital to measure the longterm stability of these electronics. This requirement necessitated development of a versatile and easily controlled pulsing system. The details of all these electronic elements are described in the following sections.

2.4.1 Charge Integrating Pre-amplifier

The quality of the pre-amplifier (PA) used is a critical component in the measured energy resolution of the Si detector. Given the number of channels involved and the space constraints, all pre-amplifiers were constructed using surface mount technology, with the exception of the input field effect transistor (FET) and the load resistor. Discrete components were used for the input FET to allow access to the largest variety of input FET's. To achieve the best possible resolution it is necessary for the input FET to have optimal characteristics (transconductance, slew rate, etc.). Using this approach we were able to limit the size of the pre-amplifier to 0.7 in x 1.0 in. A schematic of the pre-amplifier is shown in Fig. 2.7. The three FET's we tested were the J109 (Siliconix), 2N5434 (InterFET), and the IF9030 (InterFET). The principal characteristics of these FET's are summarized in Table 2.1. Our tests demonstrated that pre-amplifiers with the IF9030 provided measurably better energy resolution than those with the other two FET's. In benchtests the PA with the IF9030 was able to produce a resolution of 37 keV for a 6 MeV α particle. In measurements with a internal conversion electron from ^{209}Bi we measured an intrinsic resolution of 14 keV. We therefore selected the IF9030 for all strips in which energy resolution was important; *i.e.* the front strips of the 500 μm detector (EF₅₀₀). For the back strips of the 500 μm detector (EB₅₀₀), which are primarily used for position measurement, we used the 2N5434, which was significantly cheaper than the IF9030. The quality of the output signal was further ensured by use of a high quality isolation buffer amplifier (HA5002). The LASSA charge integrating pre-amplifier is shown on the right hand side of Fig. 2.8.

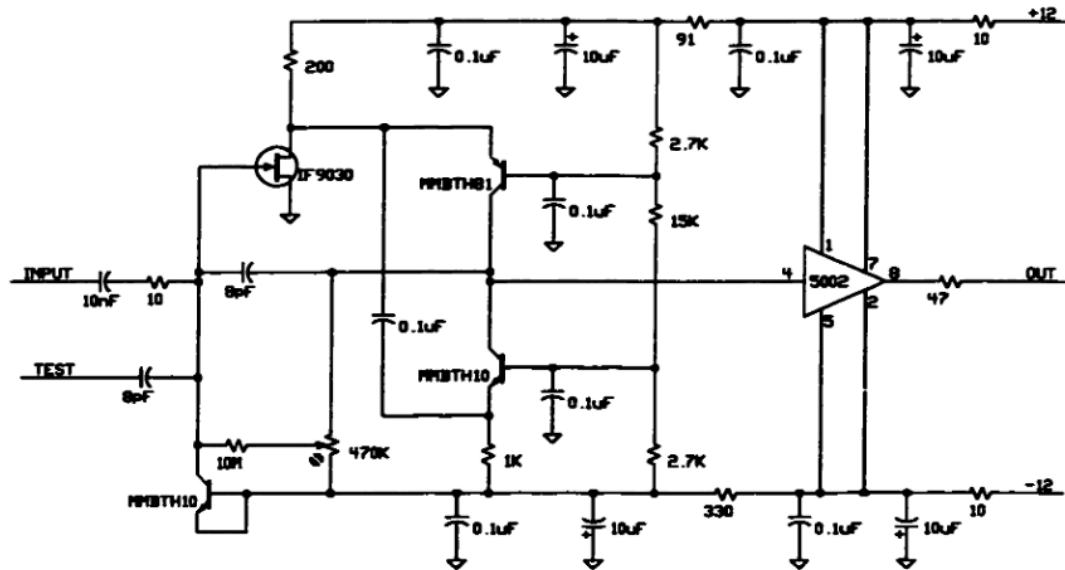


Figure 2.7: Electronic circuit diagram of pre-amplifier.

FET	$V_{GS(off)}$ (V)	$r_{DS(on)}$ (Ω)	I_{Doff} (pA)	t_{on} (ns)
J109	-2 to -6	12	20	4
2N5434	-3 to -9	7	10	2.5
IF9030	-2 to -7	5	10	7

Table 2.1: Comparison of the characteristics of different FET's tested in the LASSA preamp circuit.

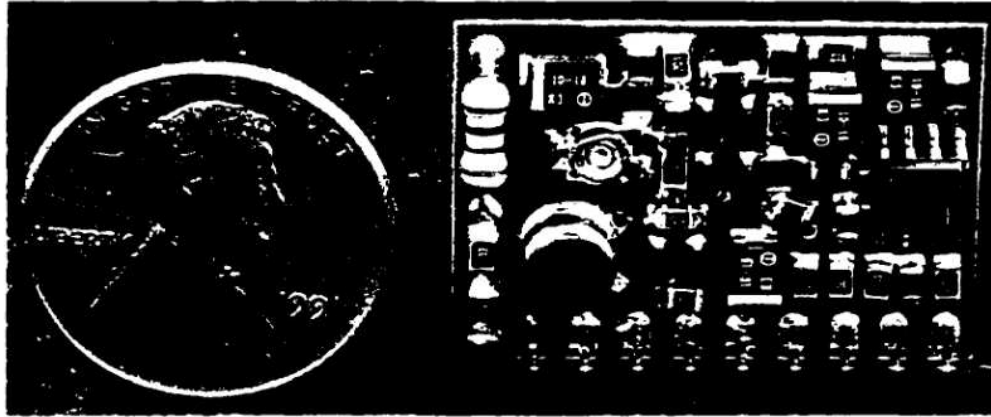


Figure 2.8: Photo of a pre-amplifier.

The pre-amplifiers are plugged into a motherboard (16 channels) that provides power, a distributed pulser signal, and the individual detector inputs and outputs. These motherboards, housed in an aluminum box, operate in vacuum with active cooling to dissipate the heat generated. Each pre-amplifier generates ~ 300 mW.

2.4.2 Silicon Processor Module

In order to process the Si (and CsI(Tl)/PD) signals efficiently, we developed a double-width CAMAC module consisting of a slow shaper, a timing filter amplifier, a leading edge (LE) discriminator, and a time-to-charge converter all for 16 independent channels [23]. The output of the timing filter amplifier for a Si strip (EF₅₀₀) has a risetime of ~ 25 ns, resulting in a time resolution of 2-3 ns, making fast coincidence timing possible. The timing resolution is limited by the LASSA pre-amplifier. We achieved a risetime of ~ 12 -14 ns with a prototype fast pickoff circuit that was not implemented in the final design due to its additional heat dissipation. The CAMAC module also provides an OR output of the discriminators, a linear signal proportional to the number of channels above threshold (MUL), and a pile-up bit. The linear and logic signals are multiplexed separately to an output for inspection purposes. The gain of the slow shaper and the thresholds of the LE discriminators are controllable

via an 8-bit digital-to-analog (D/A) converter. Integration and differentiation constants for the slow shaper can be modified by changing plug-in resistors and capacitors in the module. The output polarity of the slow analog signal is selectable by internal jumpers. A functional block diagram of the silicon processor module is shown in Fig. 2.9.

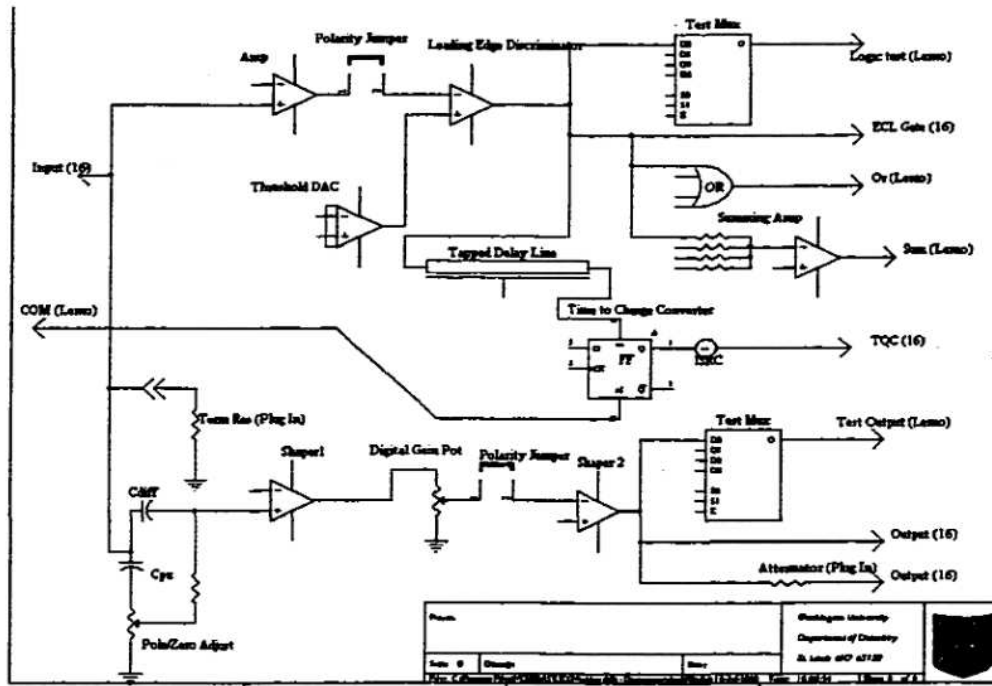


Figure 2.9: Functional block diagram of silicon processor module.

2.4.3 Stability Measurement

In order to monitor the stability of the electronics over an extended period of weeks, an automated pulsing system was developed at Indiana University [24]. This pulser is stable to within $\sim 0.1\%$ and injects a precise voltage into the test input of each pre-amplifier. A functional block diagram of the IU pulser is shown in Fig. 2.10. A Master Clock (oscillator of

3.2768 MHz) synchronizes all analog pulses. Two different capacitors are charged to provide pulses for the Si (ΔE_{65} , EF_{500} , EB_{500}) and CsI(Tl) pre-amplifiers separately. The charging rate is controlled by a 12-bit D/A converter that allows remote manipulation of the pulse amplitude. An attenuator on each class of signals (ΔE_{65} , EF_{500} , EB_{500} , and E_{CsI}) allows selection of either a high or low gain range which differ by a factor of 10. The signals are subsequently fanned out by the driver electronics to 10 pulser channels each. Each pulser channel has a remotely controllable relay on the output and has sufficient power to drive 16 pre-amplifiers without loading effects. The pulse frequency is selectable from 0.5 to 100 Hz. All functions of the pulser, including the amplitude of the pulse for any pulser channel and the ON/OFF state of the output relay, can be varied under computer control *via* an RS-232 serial interface. During the course of an experiment, the pulser can be operated in "picket-fence mode." In this mode, the pulse amplitude is incremented automatically every 1000 pulses in order to span the entire dynamic range of the electronic channel. Thus, both the gain and linearity of all electronic channels are measured continuously. Moreover, changes in electronic noise can be distinguished from radiation damage to the Si detector. All pulses generated by the IU pulser were identified by a bit in the data stream, allowing separation of these events in the off-line analysis. The IU pulser also facilitates gain matching of electronic channels during the start-up phase of an experiment.

Due to the long duration of some of the experiments, a major concern was the extent to which the IU pulser could track changes in electronic gain. The stability achieved during a recent experiment is depicted in Fig. 2.10. In this figure, the percent change in the fitted slope relating the Si ADC channel to the IU pulser amplitude is plotted as a function of time. The four panels in Fig. 2.11 show increasing sensitivity to variations in gain. Evident in panel a) (the largest gain variations) are three different regions of gain. Each of these regions corresponds to a different non-contiguous part of the experiment. These gain changes were manually selected during the experiment. Within each region the gain is relatively constant. In panel b) a somewhat different pattern is observed. Over the interval 1000-3000 minutes the gain changes steadily. After this interval it remains relatively constant. A somewhat similar behavior is observed in panel c) with a higher level of sensitivity. Finally, panel d) shows a trend in gain change that is constant within the sensitivity of the gain change determination. From this figure we deduce that electronic changes in gain can be monitored

at the 0.02% level.

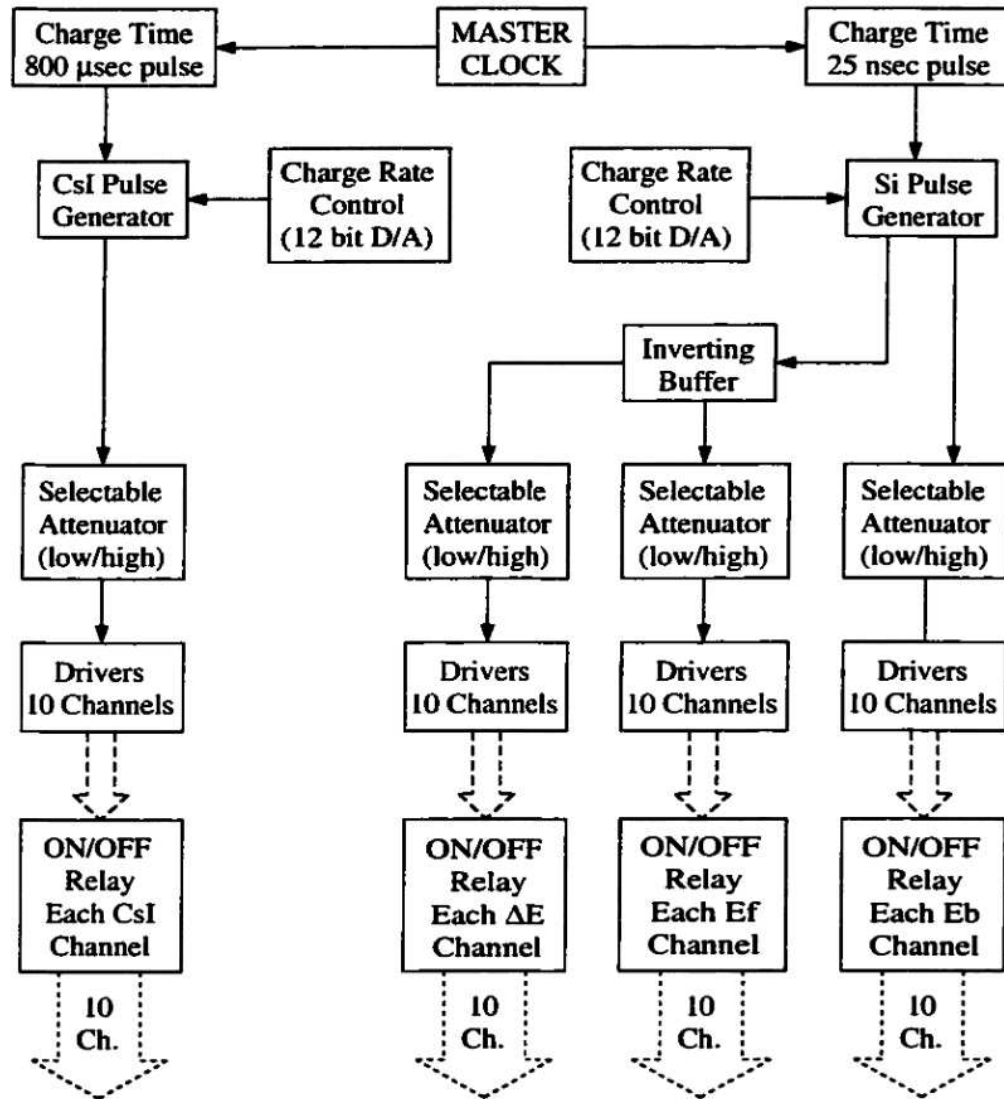


Figure 2.10: Functional block diagram of IU pulser.

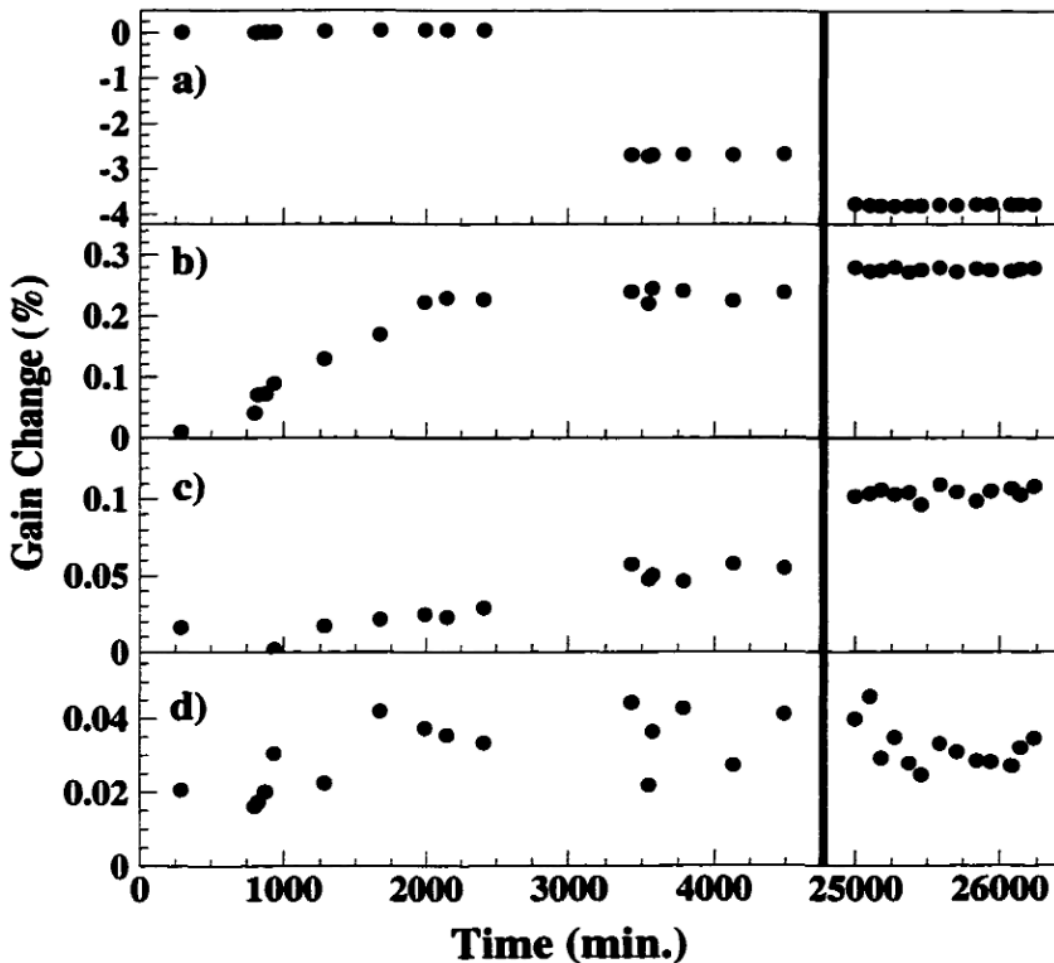


Figure 2.11: Stability as measured by IU pulser. The red line denotes a 14 day separation between the two parts of the experiment.

2.5 Overview of LASSA Data Acquisition

An overview of the LASSA electronics can be seen in Fig. 2.12. Analog signals for the Si and CsI(Tl)/PD detectors processed by the processor module were digitized in Phillips Scientific peak-sensing ADC's (7164H) or Lecroy 4300B Fast Encoding Readout ADC's. A total of thirty 16-channel ADC's and nine FERA modules were required to read out all the

signals from LASSA. Read-out of this relatively large number of electronic channels was facilitated by a non-standard readout technique to improve upon what is attainable under the CAMAC standard for the Phillips 7164H.

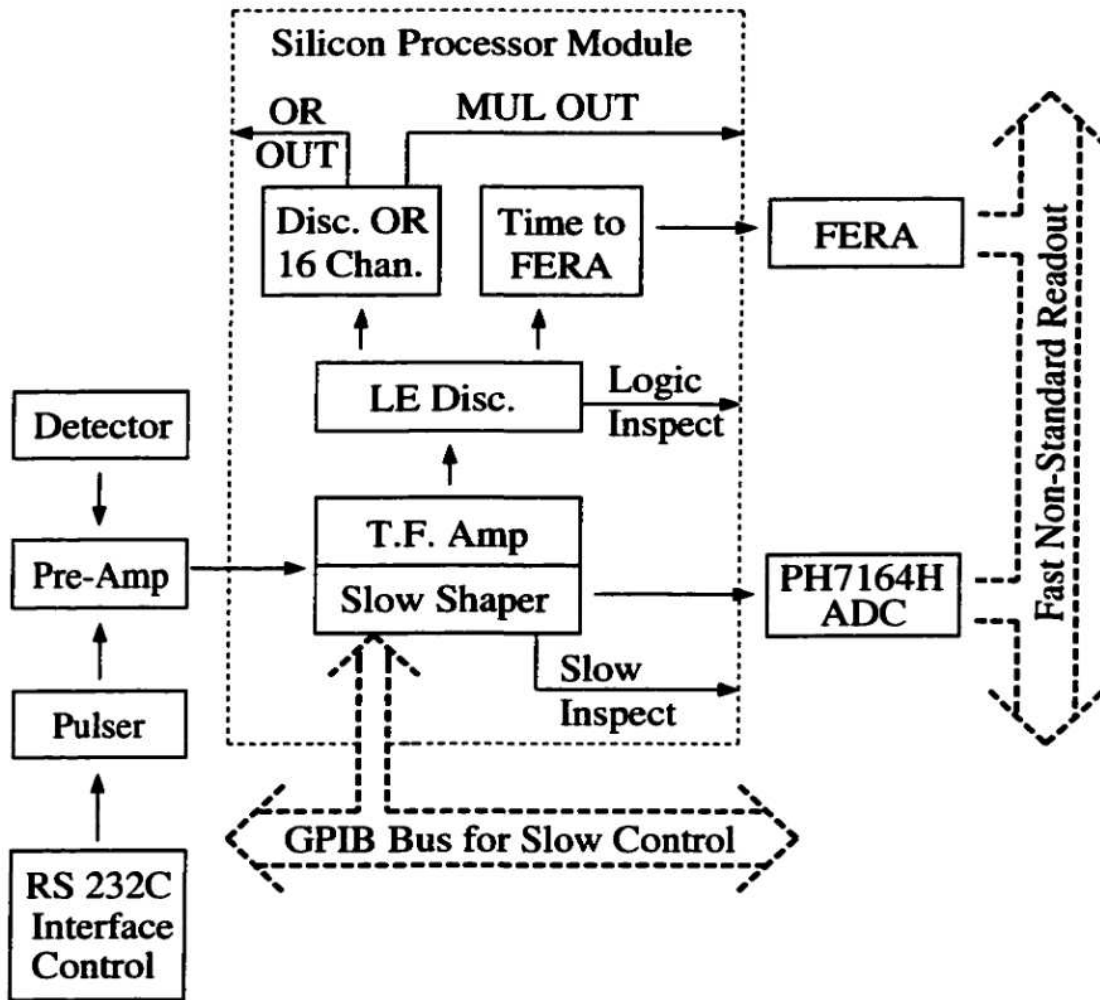


Figure 2.12: Functional block diagram of the electronics.

The Phillips 7164H CAMAC ADC's were read out using a specially designed CAMAC-to-FERA protocol converter SS32 [25]. Utilizing its intrinsic intelligence, every converter executed a hit-pattern-based sparse readout of up to 24 ADC's *via* the standard CAMAC

protocol. The data were then immediately transferred *via* a front panel 16-bit ECL port to the remote FERA receiver, pursuant to the Lecroy FERA handshaking protocol. Limited by the ADC access time, the readout of the Phillips ADC's proceeded at a rate of approximately 3 MHz. This non-standard readout, which required no hardware modifications to the 7164H ADC's, the CAMAC crates or controllers, resulted in a 7.5-fold reduction in the readout time of the LASSA electronics as compared to a standard CAMAC readout.

2.6 Calibration

Calibration of the LASSA modules consists of three parts: calibration of ΔE_{65} Si strips with an α -particle source, calibration of all electronic channels with a precision charge pulser into the detector input, and calibration of the telescopes with direct beam. Depending upon the goal of the experiment, *e.g.* if isotopic identification beyond $Z = 4$ is not required nor is good absolute energy determination for energetic light particles, the complexity of the in-beam calibration can be minimized or perhaps omitted altogether. The most demanding requirements are isotopic identification for $Z \geq 5$ and calibration of the CsI(Tl) for energetic particles. These requirements necessitate an in-beam calibration. An example of such a calibration procedure, performed with the Michigan State K1200-A1200 cyclotron/magnetic analysis system following a series of experiments, is described below.

Immediately following the last experiment, the LASSA array was calibrated in three stages. The first stage involved calibration of the device in the running configuration with a precision pulser and a charge terminator. In the second stage, a series of fragmentation beams was used and each detector was repositioned to allow beam to be put directly into the telescope. Beams of 20 MeV/u ^{16}O and 40 MeV/u ^{36}Ar were accelerated by the K1200 cyclotron at Michigan State University and used to bombard a production target at the exit of the cyclotron. Reaction products from projectile fragmentation were subsequently selected according to magnetic rigidity by the A1200 magnetic channel. These low intensity secondary beams (~ 1300 p/s) were then used to directly scan the detector face. The beams used are listed in Tables 2.2 and 2.3. These beams were useful in correcting the thickness non-uniformity of the 65 μm Si detector, as well as in calibrating both of the Si detectors and the CsI(Tl) detectors. Finally, following the fragmentation beams, a ^{228}Th α -particle

source was used to calibrate the 65 μm detectors.

^{16}O fragmentation products	E(MeV)	^{16}O fragmentation products	E(MeV)
p	77.62	^9C	317.4
d	40.00	^{10}C	286.7
t	26.82	^{11}C	261.3
^3He	105.8	^{12}C	240.0
^4He	80.00	^{13}C	221.9
^6He	53.65	^{12}N	325.4
^6Li	120.0	^{13}N	301.0
^7Li	103.2	^{14}N	280.0
^8Li	90.42	^{13}O	391.7
^7Be	182.3	^{14}O	364.6
^9Be	142.5	^{15}O	340.8
^{10}Be	128.5	^{16}O	320.0
^8B	248.5		
^{10}B	200.0		
^{11}B	182.2		

Table 2.2: Secondary beams produced by projectile fragmentation of ^{16}O used in the calibration of LASSA.

^{36}Ar fragmentation products	E(MeV)	^{36}Ar fragmentation products	E(MeV)
p	151.1	^{13}N	601.0
d	79.98	^{14}N	559.9
t	53.94	^{15}N	523.9
^3He	210.0	^{16}N	492.3
^4He	160.0	^{15}O	680.6
^6He	107.9	^{16}O	639.8
^6Li	239.9	^{17}O	603.6
^7Li	206.8	^{18}O	571.2
^8Li	181.6	^{18}F	719.8
^7Be	363.4	^{19}F	683.4
^9Be	285.6	^{20}F	650.4
^{10}Be	257.9	^{20}Ne	799.8
^{10}B	399.9	^{22}Na	879.8
^{11}B	364.9	^{23}Na	843.0
^{12}B	335.4	^{24}Na	809.1
^{11}C	521.5	^{24}Mg	959.8
^{12}C	479.9	^{25}Mg	922.9
^{13}C	444.3	^{26}Mg	888.7
^{14}C	413.6		

Table 2.3: Secondary beams produced by projectile fragmentation of ^{36}Ar used in the calibration of LASSA.

2.6.1 Thickness Non-uniformity Correction for the 65 μm Detector

Following the energy calibration of the LASSA 65 and 500 μm detectors using the information provided by the precision charge pulser (Ortec 448) and the ^{228}Th α -particle source, the observed isotopic resolution is rather poor, as illustrated in Fig. 2.13. However, we had previously determined that the intrinsic isotopic resolution of such Si strip detectors is better than the result shown in Fig. 2.13. We had established this fact by an in-beam test of a prototype telescope carried out at the Texas A & M University Cyclotron Institute.

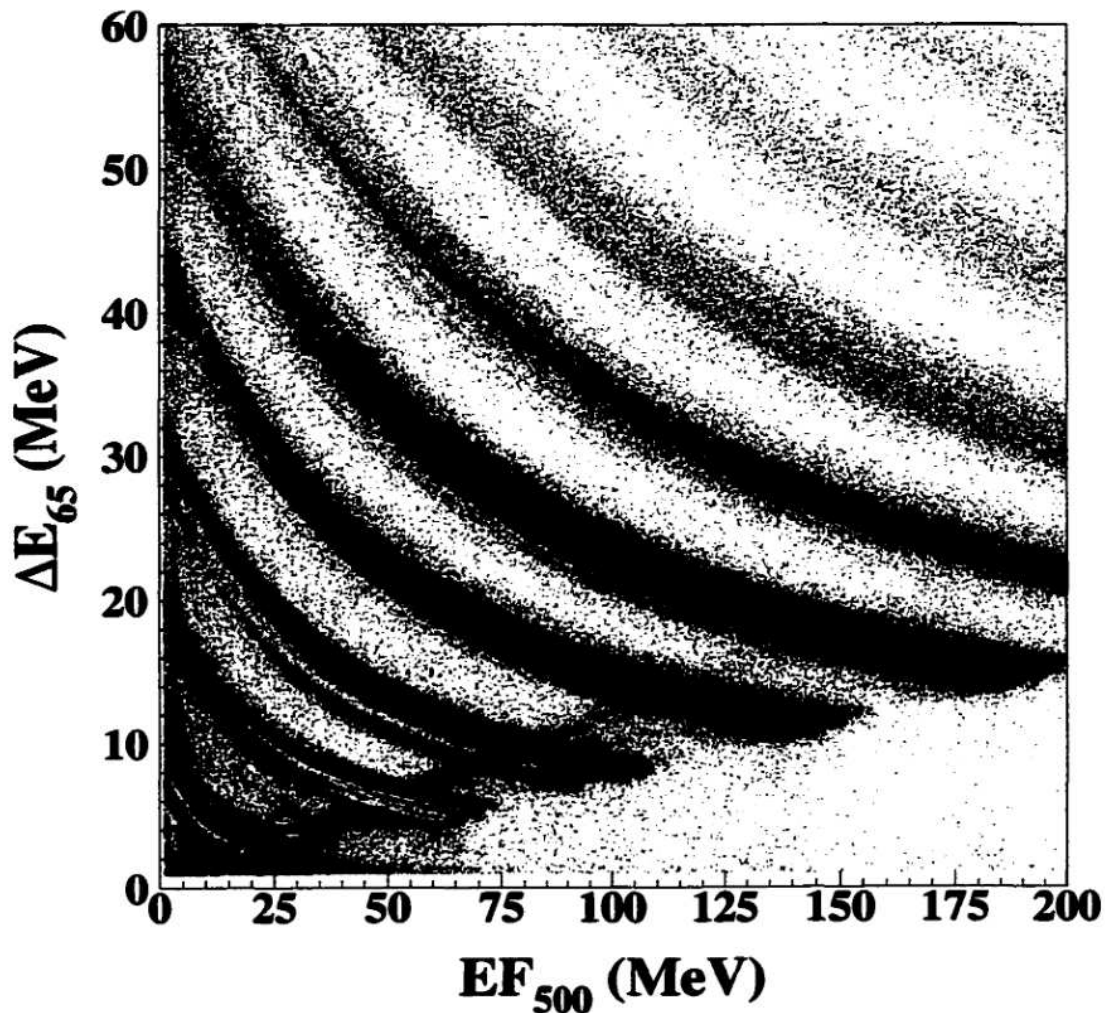


Figure 2.13: Two-dimensional plot of ΔE_{65} - E_{500} before thickness correction of the 65 μm detector.

When one constructs a ΔE - E map (ΔE_{65} - EF_{500}) selected on one particular “pixel” (the intersection of a given front and back strip in the 500 μm detector) for the prototype telescope, one observes isotopic resolution of carbon isotopes, limited only by the counting statistics. These results suggested a thickness variation of the prototype 65 μm wafer across its face. This finding is consistent with results obtained for the non-planarity of thin Si detectors [22, 26].

Since the energy loss a particle experiences in traversing the detector is proportional to the detector thickness, it is crucial to correct for the thickness non-uniformity of the 65 μm detector. Therefore, in analyzing data from the LASSA detectors, we first determined the change in thickness along a single strip of the LASSA ΔE_{65} detector. All pixels along a strip are associated with the same electronic channel and hence the deduced thickness variation is calibration independent. To determine the thickness variation along a strip we used fixed points in the residual energy in the 500 μm detector (EF_{500}) of α particles and determined the associated energy loss in the transmission detector (ΔE_{65}) for each of the pixels in the strip. Once the thickness variation along a strip was corrected, we were able to utilize the same technique for isotopically identifying fragments through boron. We parameterized the matching factors obtained in this way as a function of ΔE_{65} (MeV). As a result of this procedure, variations in the calibration between strips, as well as the thickness variation between strips, is minimized. The two-dimensional correction matrix we obtained in this way is shown in Fig. 2.14. The X and Y position shown in the figure reflect the EF_{500} and EB_{500} strips in the 500 μm detector, respectively. Along a strip in the ΔE detector (constant value of X as the strips in the ΔE_{65} and EF_{500} run in the same direction), the variation reflects simply the thickness variation of the 65 μm detector. Between strips one is sensitive to both the thickness variation of the 65 μm detector, as well as to small residual electronic variations (subsequent to calibration) between different electronic channels. The matching procedure using this matrix resulted in the two-dimensional ΔE - E spectrum (ΔE_{65} - EF_{500}) displayed in Fig. 2.15. This mapped spectrum clearly shows isotopic resolution through nitrogen and is representative of all nine telescopes in LASSA. A comparison of Fig. 2.13 with Fig. 2.15 illustrates the crucial importance of correcting for the thickness variation in the 65 μm detector in achieving optimal particle identification. The spectrum shown in Fig. 2.15 is for all particles that do not have a CsI(Tl)/PD signal; *i.e.* particles that

either stop in the 500 μm Si or “punch-through” 500 μm Si but somehow escape the CsI(Tl) crystals behind the silicon detector. The background haze visible in Fig. 2.15 is due to particles passing through inactive regions (edges, interstrips, etc.) of the telescope, resulting in inconsistent $\Delta E_{65}\text{-}EF_{500}$ combinations. Also visible in Fig. 2.15 is a faint band of particles with a positive slope between He and Li. Particles in this band “punch-through” the 500 μm Si detector and consequently that signal is effectively a ΔEF_{500} signal. These particles are present due to a slight mis-alignment of the Si detectors relative to the CsI(Tl) crystals, as well as to the dead area between adjacent CsI(Tl) crystals (due to wrapping for the purpose of optical isolation). One is able to eliminate this contribution, at the expense of geometric efficiency, by gating selectively on the position in the Si detectors.

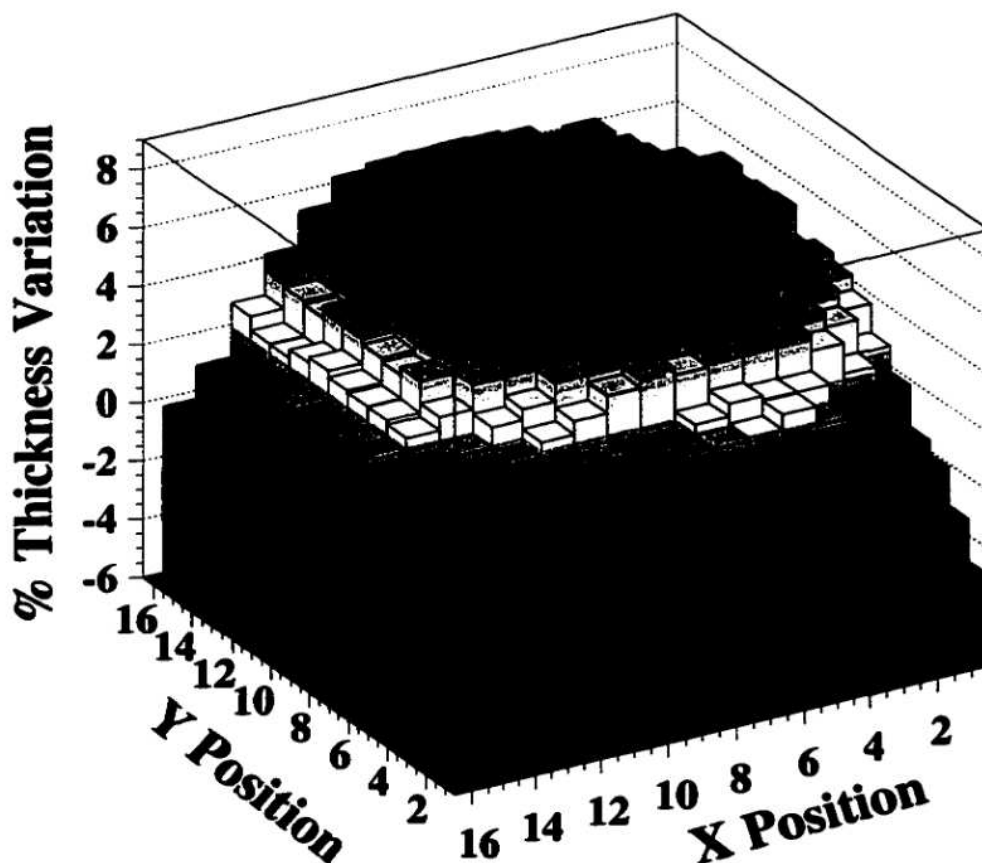


Figure 2.14: Two-dimensional map of thickness correction factors for 65 μm detector.

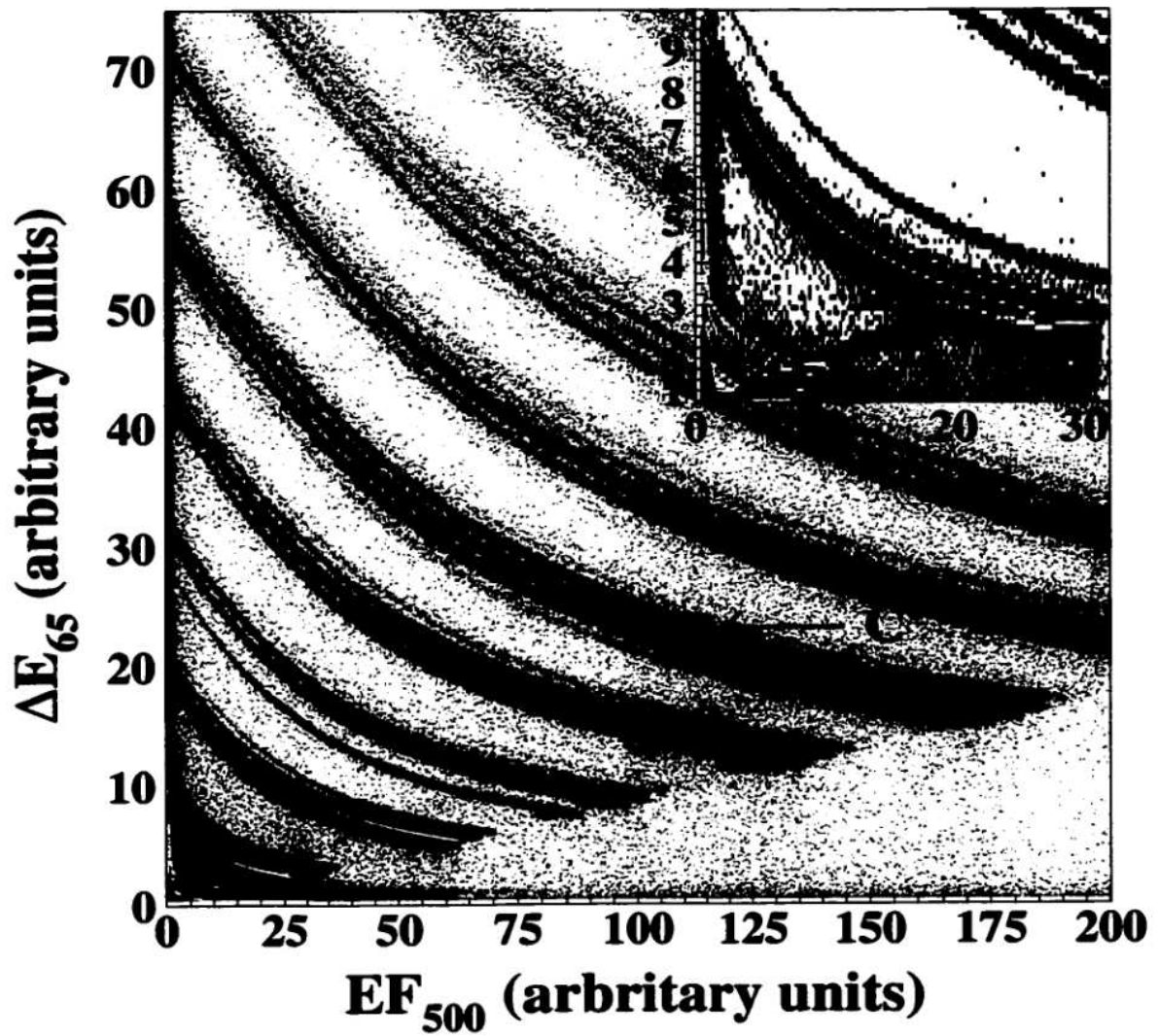


Figure 2.15: Two-dimensional plot of ΔE_{65} - EF_{500} following thickness correction of the $65\mu\text{m}$ detector.

2.6.2 Thickness Determination for the 500 μm Detector

Using the fragmentation data, a two-dimensional ΔE - E spectrum (EF_{500} - E_{CsI}) of the Si-CsI(Tl) was constructed for each telescope and the centroids in EF_{500} were determined for all identifiable isotopes. Since the Z , A and incident energy of these ions (selected by the magnetic channel) is known, the energy deposited in the 500 μm detector could be calculated with an energy loss program, TRIM [27], for different input values of the detector thickness. The effective thickness of the detector was determined by minimizing the difference between the calculated energy loss and the measured energy loss as a function of thickness. The effective thicknesses deduced in this manner for the nine telescopes are summarized in Table 2.4. Also shown, for reference, in Table 2.4 are the nominal thicknesses quoted by the manufacturer. These nominal thicknesses were determined by measuring, by mechanical means, an outer section of the silicon wafer from which a detector was cut. Based on our previous work [22], it is not surprising that the silicon detectors are on average 15 μm thinner than their nominal values. Subsequent energy calibration of the CsI(Tl) utilizes the deduced thicknesses.

Detector	1	2	3	4	5	6	7	8	9
Nominal Thickness (μm)	510	499	471	461	468	481	456	482	476
Deduced Thickness (μm)	494	481	460	442	456	464	453	461	454

Table 2.4: Nominal and deduced thicknesses of the 500 μm LASSA Si strip detectors.

2.6.3 Isotopic Resolution in the Si-CsI(Tl)

To identify particles that stopped in the CsI(Tl) crystal, the EF_{500} signal of the 500 μm detector was chosen due to the superior PA used for these signals, as compared with EB_{500} . The EB_{500} signals were used with higher gain shaping amplifiers to improve the identification of the isotopes of hydrogen at the expense of dynamic range. The primary

purpose of the EB_{500} signals was for position determination.

Following calibration of the EF_{500} signals with a precision charge pulser two-dimensional ΔE - E maps (EF_{500} - E_{CsI}) were generated summed over the pixels in a demi-strip. A demi-strip corresponds to the half of an EF_{500} strip in front of a single CsI(Tl) crystal. In a procedure analogous to the analysis of the ΔE_{65} - EF_{500} , we generated matching factors by determining the ΔE for fixed values of Z , A , and CsI(Tl) light output. By examining the light output in different demi-strips associated with different fragments from the fragmentation beams, we deduced that the light output of the CsI(Tl) did not manifest a significant global trend as a function of position. Local variations measured by penetrating α particles have been reported previously [28]. By this matching procedure we were able to produce a matched EF_{500} - E_{CsI} spectrum for each crystal. Different CsI(Tl) crystals within a telescope were subsequently matched by utilizing the fragmentation beams. A typical EF_{500} - E_{CsI} two-dimensional spectrum for a telescope is shown in Fig. 2.16. The isotopes of oxygen can be clearly distinguished. The background haze visible in Fig. 2.16 has two origins. Particles passing through the inactive regions of the telescope give rise to spurious EF_{500} - E_{CsI} combinations. Coincidence summing within a CsI(Tl) crystal is particularly evident in the low EF_{500} region. Double-hits of a neutron or high energy proton with a second particle in a single CsI(Tl) crystal distort the E_{CsI} signal. Assignment of the isotopically resolved bands (PID: particle identification lines) was further checked by comparison with the fragmentation beams, resulting in no uncertainty in associating a given locus with a particular isotope.

A more quantitative measure of the isotopic resolution achieved is depicted in Fig. 2.17. In this figure, the isotopic distributions for carbon and oxygen fragments resolved in the ΔE_{65} - EF_{500} and the EF_{500} - E_{CsI} are shown. These spectra are summed over all nine telescopes in LASSA. In the Si-CsI(Tl) carbon PID spectrum (panels c), one can resolve all isotopes from ^{10}C to ^{16}C . Separation of ^{10}C from ^{11}C is somewhat worse in the Si-Si PID spectrum (panel a). In the oxygen PID spectra (panels b and d) isotopes from ^{15}O to ^{20}O are clearly visible. This excellent particle identification meets the design criteria for the array. The isotopic resolution achieved by LASSA facilitates studies of mirror nuclei. For example, the isotopic resolution achieved allows examination of the $^8\text{Li}/^8\text{B}$, $^{10}\text{Be}/^{10}\text{C}$, $^{13}\text{C}/^{13}\text{N}$, and $^{15}\text{N}/^{15}\text{O}$ mirror nuclei in addition to previously studied pairs.

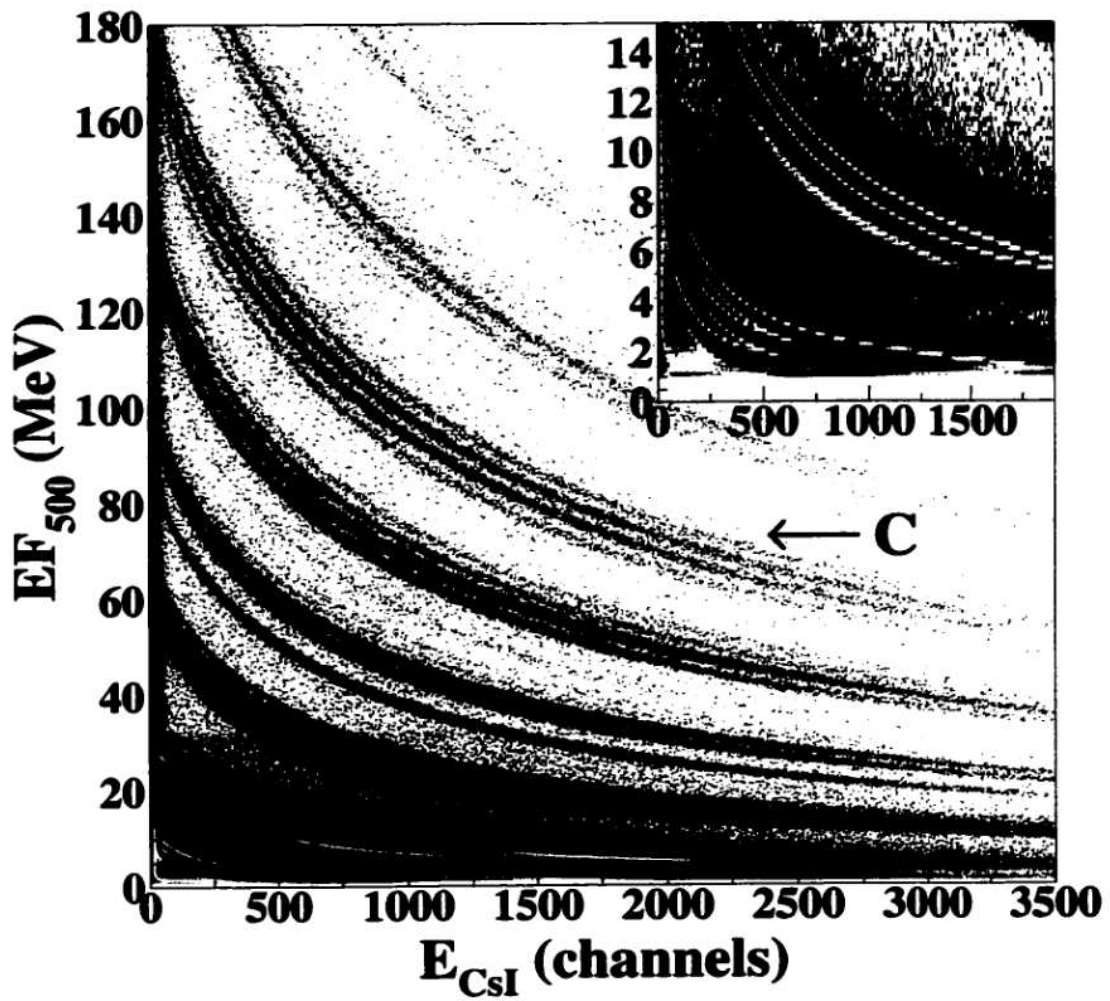


Figure 2.16: Two-dimensional plot of $\Delta EF_{500}\text{-CsI(Tl)}$ for a telescope in LASSA.

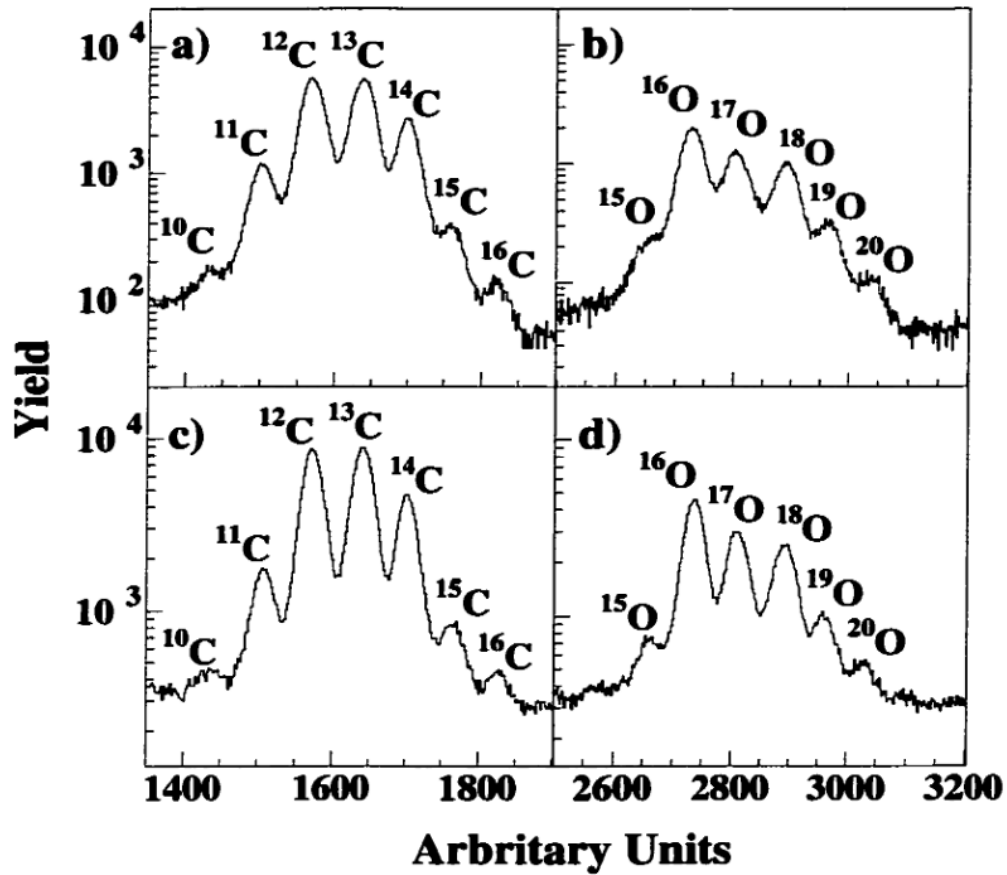


Figure 2.17: Panels a) and b) depict the isotopic distributions for C and O respectively in the Si-Si portion of the telescope. Panels c) and d) depict the isotopic distributions for C and O respectively in the Si-CsI(Tl) portion of the telescope. These spectra are summed over all nine telescopes in LASSA.

2.7 Energy calibration of the CsI(Tl)

To calibrate the CsI(Tl) crystals in energy we used the two-dimensional spectra ($EF_{500}-E_{CsI}$), an example of which is shown in Fig. 2.16. For fixed E_{CsI} (channel number) and each of the isotopes identified, the corresponding energy in the 500 μm detector (EF_{500}) was determined. Using the energy deposited in the 500 μm detector, the corresponding energy deposited in the CsI(Tl) crystal was calculated using TRIM [27]. (This approach works well when a significant change in EF_{500} is associated with a finite change in E_{CsI}). The light output (L.O.) response arrived at in this way is shown in Fig. 2.18 for a typical telescope. Open circles and open squares denote the PID line data extracted from the $\Delta E-E$ maps ($EF_{500}-E_{CsI}$) for ^{11}C and ^{14}C , while asterisks represent the data provided by the fragmentation beams (Tables 2.2 and 2.3). A clear mass dependence is evident, particularly at high energy. In the right-hand panel of Fig. 2.18, the fragmentation data is fit using the parameterization of Larochelle *et al.* [29] and the resulting curves for ^{11}C , ^{12}C , ^{13}C , and ^{14}C are shown. As can be seen in this right-hand panel, the fits do not describe the data extracted from the PID lines (open symbols), particularly at low values of the light output. These differences may be due to temperature variations in the CsI(Tl) crystals (although the detector housing is actively cooled) as the calibration with the fragmentation beams was conducted following the experiment and the CsI(Tl) may not have had sufficient time to temperature equilibrate prior to the calibration.

In the left-hand panel of Fig. 2.18 we show the result of fitting the PID line data with a two part fit. For the low energy portion of the calibration ($\text{L.O.} \leq 1000$) the formalism described in Ref. [30] was used, however, each isotope was calibrated independently as this formalism has no explicit mass dependence. In the high energy region ($\text{L.O.} \geq 1000$), the formalism described in Ref. [29] was used as this formalism has an explicit mass dependence. The two fit regions were “feathered” together in a linear fashion over the interval 900 - 1100. This procedure yielded the best fit of the PID line data. As can be seen in the left-hand panel, this calibration is in reasonably good agreement with the fragmentation data at low energies, but over predicts the energy for large values of the light output. This difference between the fragmentation and characteristic line data can be used as an estimate of the absolute uncertainties involved in the CsI(Tl) calibration.

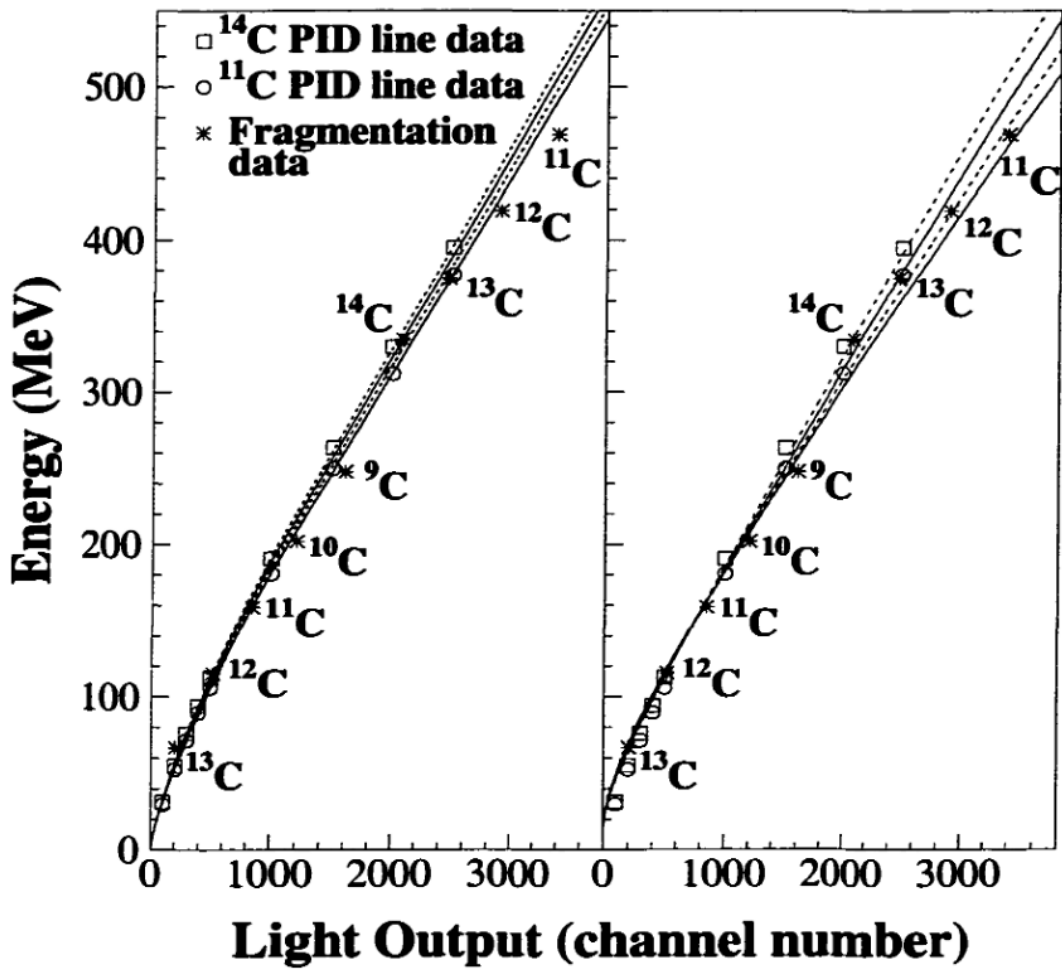


Figure 2.18: Light output of CsI(Tl) as a function of Z, A, and E.

To quantitatively examine the absolute uncertainties in the CsI(Tl) calibration, we have constructed the percent deviation of the data from the fits shown in the Fig. 2.18. The percent deviation from the fit to the PID line data alone is shown in the top panel of Fig. 2.19. The corresponding case in which the fragmentation data alone has been fit is shown in the bottom panel of the figure. In the top panel, a maximum deviation of 5% is observed at the highest incident energy for the fragmentation data. In the lower panel, where one relies on the fragmentation data alone for the light output calibration, the percent deviation is as

large as 40% at low energy. Part of the difficulty in relying upon the fragmentation data alone is the restricted range in which these data were measured and the limited number of constraining points. In addition, the large deviation shown in the lower panel is amplified because it is examined in relative rather than absolute terms. The uncertainty associated with energy loss calculations for particles that just punch through the 500 μm detector may also play a role in amplifying this difference. Nevertheless, this plot emphasizes the difficulty in performing an absolute calibration to the sub-percent level (as has been achieved with the Si detectors) with detectors that are both non-linear and have a temperature sensitive response function.

From the isotopic resolution we have achieved, we estimate the uncertainty in relative calibration between different Si strips and electronic channels to be $\sim 0.5\%$, however, the uncertainty in absolute calibration (due to the CsI) is considerably larger $\sim 2\text{-}5\%$.

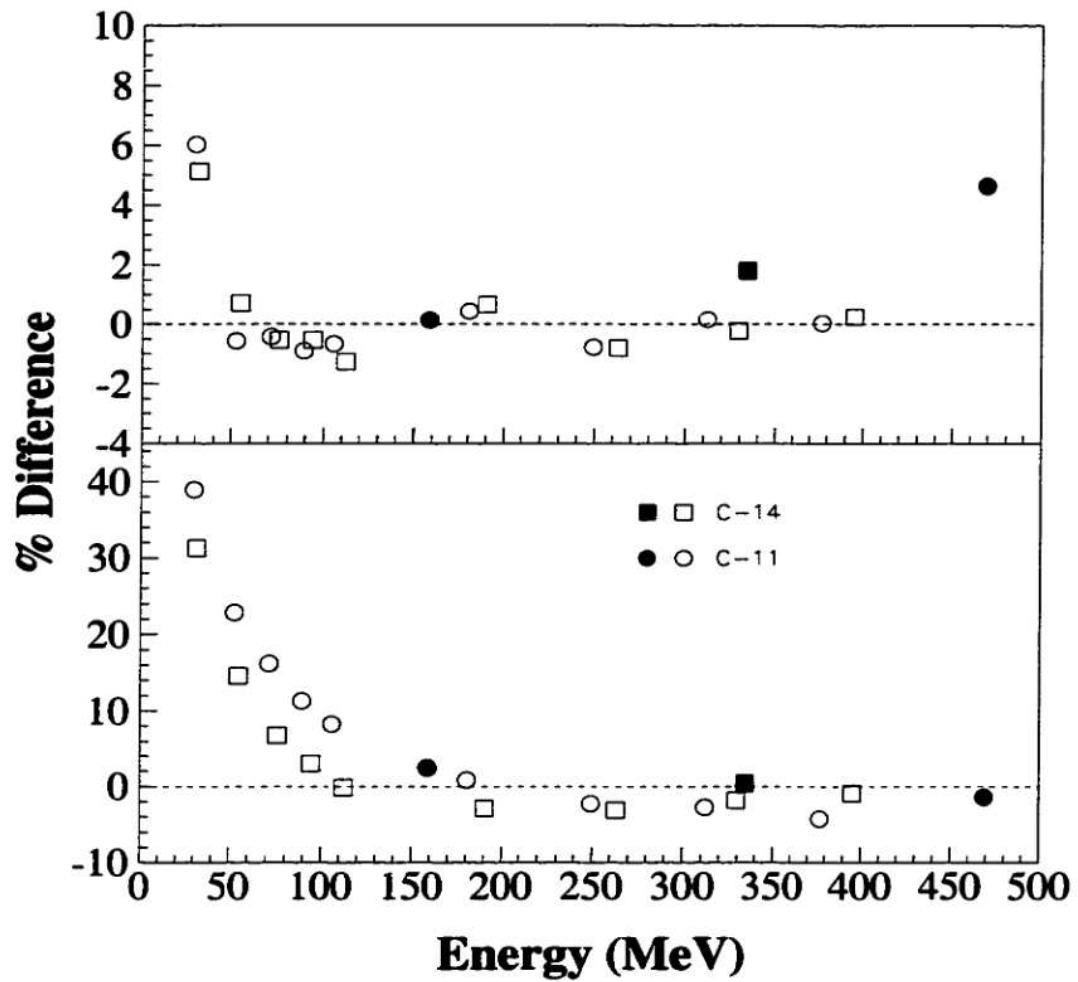


Figure 2.19: Percent deviation of the fragmentation and PID calibration data from the PID data fit (top) and fragmentation data fit (bottom).

References

- [1] H. Muller and B. Serot, *Phys. Rev. C* **52**, 2072 (1995).
- [2] L. G. Sobotka *Phys. Rev. C* **50**, R1272 (1994).
- [3] J. F. Dempsey, *et al.*, *Phys. Rev. C* **54**, 1710 (1996).
- [4] M. Colonna, M. di Toro, G. Fabris, S. Maccarone, *Phys. Rev. C* **57**, 1410 (1998).
- [5] Bao-An Li and C. M. Ko, *Phys. Rev. C* **57**, 2065 (1998).
- [6] F. Rami, *et al.*, *Phys. Rev. Lett.* **84**, 1120 (2000).
- [7] R. LaForest, *et al.*, *Phys. Rev. C* **59**, 2567 (1999).
- [8] R. Nebauer, *et al.*, *Nucl. Phys.* **A658**, 67 (1999).
- [9] R. Trockel, *et al.*, *Phys. Rev. Lett.* **59**, 2844 (1987).
- [10] Y. D. Kim, *et al.*, *Phys. Rev. Lett.* **67**, 14 (1991).
- [11] H. F. Xi, *et al.*, *Phys. Rev. C* **58**, R2636 (1998).
- [12] E. Cornell, *et al.*, *Phys. Rev. Lett.* **75**, 1475 (1995).
- [13] E. Cornell, *et al.*, *Phys. Rev. Lett.* **77**, 4508 (1996).
- [14] S. Albergo *et al.*, *Nuovo Cimento* **89**, 1 (1985).
- [15] J. Pochodzalla, *et al.*, *Phys. Rev. Lett.* **75**, 1040 (1995).
- [16] Hamamatsu Photonics K.K., 360 Foothill Rd., Bridgewater, N.J. 08807 USA.
- [17] Ablestik Electronic Materials & Adhesives, Rancho Dominguez, CA 90221
- [18] Micron Semiconductor Ltd., 1 Royal Bldg, Marlborough Rd., Lancing, Sussex, BN15 8UN U.K.
- [19] Rogers Corp., Circuit Materials Division, 100 N. Dobson Rd., Chandler, AZ 85224 USA.

- [20] Printed Circuit Board prototype fabrication facility, Direct Imaging of Vermont, Inc., 30 A Street, P.O. Box 820, Wilder, VT 05088.
- [21] SIFCO Selective Plating, 5708 Schaaf Road, Cleveland, OH 44131, USA.
- [22] D. Fox, *et al.*, Nucl. Instr. and Meth. A **368**, 709 (1996).
- [23] Available from Pico Systems, 543 Lindeman Rd., St. Louis, MO 63122.
- [24] Electronic Instrument Services, Department of Chemistry, Indiana University, Bloomington.
- [25] J. Toke, DOE Report ER-40414, University of Rochester (1998) p. 160.
- [26] B. Davin, Ph.D. Thesis, Indiana University (2001).
- [27] TRIM, J. F. Ziegler, <http://www.research.ibm.com/ionbeams/home.htm>.
- [28] A. Wagner, *et al.*, Nucl. Instr. and Meth A. **456**, 290 (2001)
- [29] Y. Larochelle, *et al.*, Nucl. Instr. and Meth A **348**, 167 (1994).
- [30] P. F. Mastinu, *et al.*, Nucl. Instr. and Meth A **338**, 419 (1994).

Chapter 3

Experimental Details

3.1 Experimental Details

The experiment was performed using the K1200 cyclotron at the National Superconducting Cyclotron Laboratory at Michigan State University. Beams of ^{106}Cd or ^{114}Cd at $E/A = 50$ MeV with an intensity of $4\text{-}30 \times 10^7$ particles per second were extracted and focused on to either a ^{98}Mo or ^{92}Mo target. The ^{98}Mo target had a thickness of 0.777 mg/cm² and the ^{92}Mo had a thickness of 5.45 mg/cm². Charged particles emitted in the angular range $5.4^\circ \leq \theta_{lab} \leq 160^\circ$ were detected with the MSU Miniball/Washington University Miniball (MB/MW) phoswich detector array [1, 2]. The MB/MW detectors between $\theta_{lab} \leq 55^\circ$ and $-55^\circ \leq \phi_{lab} \leq 55^\circ$ were replaced by LASSA [3]. In addition, particle detection at forward angles ($2.1^\circ \leq \theta_{lab} \leq 4.2^\circ$) was supplemented with an annular counter (ring counter). Figure 3.1 depicts a cross sectional view of the experimental setup. Two trigger conditions were utilized during this experiment. The first condition required at least three MB/MW detectors were triggered in order to record and event. The three detector requirement decreased the probability the taking data if a single MB/MW detector was trigger due to noise or low energy electrons. The second condition involved a scaled-down number of events detected by the ring counter. The down-scaling of events from the ring counter was necessary to exclude the data from a majority of the elastically scattered projectiles that hit the ring counter.

3.2 Miniball/Miniwall

The Miniball/Miniwall array consisted of 296 fast-plastic scintillator CsI(Tl) phoswich detectors mounted in 15 independent rings. As shown in Fig. 3.1, each ring is labeled (3-11 for the Miniball and 12-16 for the Miniwall) with the number of detectors used in the experiment in parenthesis. The Miniball occupied the angular range $25^\circ \leq \theta_{lab} \leq 160^\circ$, while the Miniwall occupied the angular range $5.4^\circ \leq \theta_{lab} \leq 25^\circ$. The Miniball detectors consisted of 40 μm fast-plastic scintillator foils in front of 2 cm thick CsI(Tl) crystals, whereas the Miniwall detectors had 80 μm fast-plastic scintillator foils in front of 3 cm thick CsI(Tl) crystals.

A schematic diagram of an individual phoswich detector is shown in Fig. 3.2 [2]. To transmit the light from the fast scintillator-CsI(Tl) to the photomultiplier tube (PMT), two ultra-violet transparent plexiglass light guides were used. One light guide was the same size as the CsI(Tl) crystal and the second light guide was the size the PMT. The entire PMT as well as the second light guide were enclosed in a μ -metal shield to reduce the influence of external magnetic fields. The CsI(Tl)-light guide-light guide-PMT assembly was glued together using optical cement. In order to increase light reflection, the front face of the detector was covered by aluminized mylar foil and the CsI(Tl) crystals were covered with white teflon tape. To suppress higher counting rates from electrons, X-rays and γ -rays, all Miniwall/Miniball detectors were covered by a 4 mg/cm² Pb-Sn foil.

3.2.1 Particle Identification

When radiation interacts with CsI(Tl), fluorescent light is created. The light pulse is related to the atomic number, mass, and energy of the incident particle and can be utilized to distinguish the particle entering the CsI(Tl) [4] - [7]. The fluorescent light created can be described by the equation :

$$L(t) = L_t \exp(-t/\tau_t) + L_s \exp(-t/\tau_s)$$

where $L(t)$ is the light pulse amplitude at time t , while L_t and L_s are the total light amplitudes for the tail and slow components, respectively [6]. The time constant for the tail component (τ_t) has a value of approximately 7 μs and the slow component (τ_s) has a value of approximately 0.4-0.7 μs . In addition, τ_s and the ratio L_s/L_t are dependent on the particle

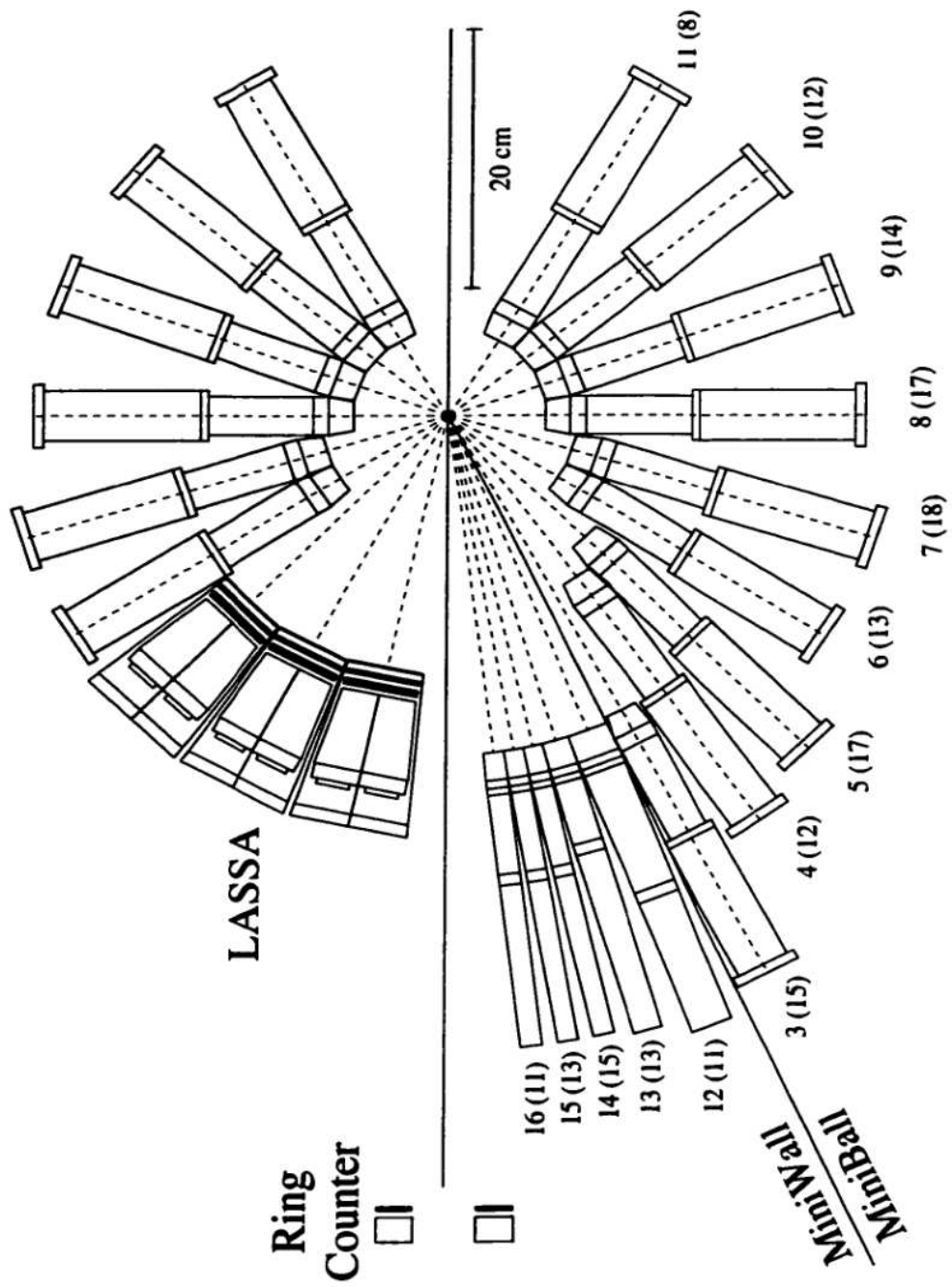


Figure 3.1: Cross sectional view of experimental apparatus.

type, whereas τ_t is independent of the particle type. As a consequence of these dependencies, the ratio of pulse heights at two different times can be used to identify different particle types. However, the identification of particles with $Z > 3$ is difficult when using the slow and tail light components [6]. To increase the capability of resolving particles with $Z > 3$, a thin fast scintillator can be added to the front of the CsI(Tl) crystal to alter the L_f/L_s ratio. The time constant for the fast component has a value of approximately 2.4 ns. In addition, the fast scintillator is chosen because more light is generated as the atomic number increases for particles passing through the scintillator.

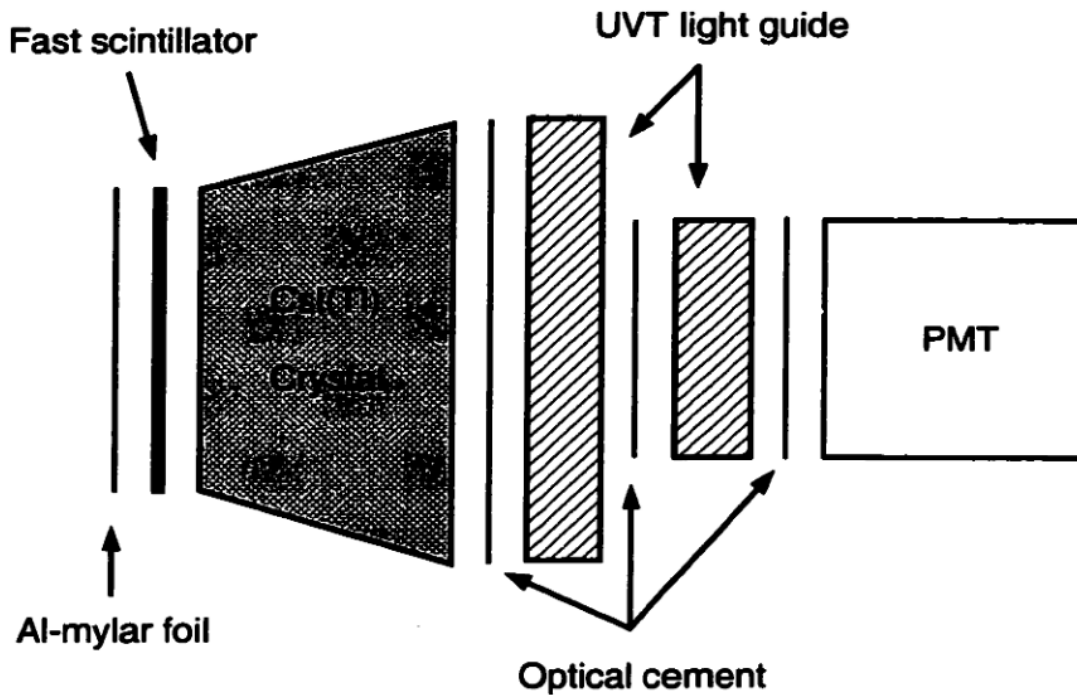


Figure 3.2: Schematic diagram of an individual phoswich detector.

Figure 3.3 depicts the anode signal from the photomultiplier tube. The 'fast' part of the signal results from the fast plastic scintillation, whereas the 'slow' and 'tail' parts of the signal result from CsI(Tl) scintillation. The length of time gates and the start of the time

gates are indicated on Fig. 3.3. To determine the atomic number of the particles detected in a Miniball/Miniwall detector, the 'fast' component is plotted against the 'slow' component, as illustrated in Fig. 3.4. Each of the distinct bands represents a different element up to $Z \approx 14$. Particle identification gates were drawn around $Z = 1$, $Z = 2$ and $Z \geq 3$. To identify the isotopes of hydrogen and helium, the 'slow' and 'tail' signals are used as shown in Fig. 3.5. Particle identification gates were drawn for protons, deuterons, tritons, ${}^3\text{He}$, ${}^4\text{He}$, ${}^6\text{He}$, and ${}^8\text{Be}$ breakups (two ${}^4\text{He}$).

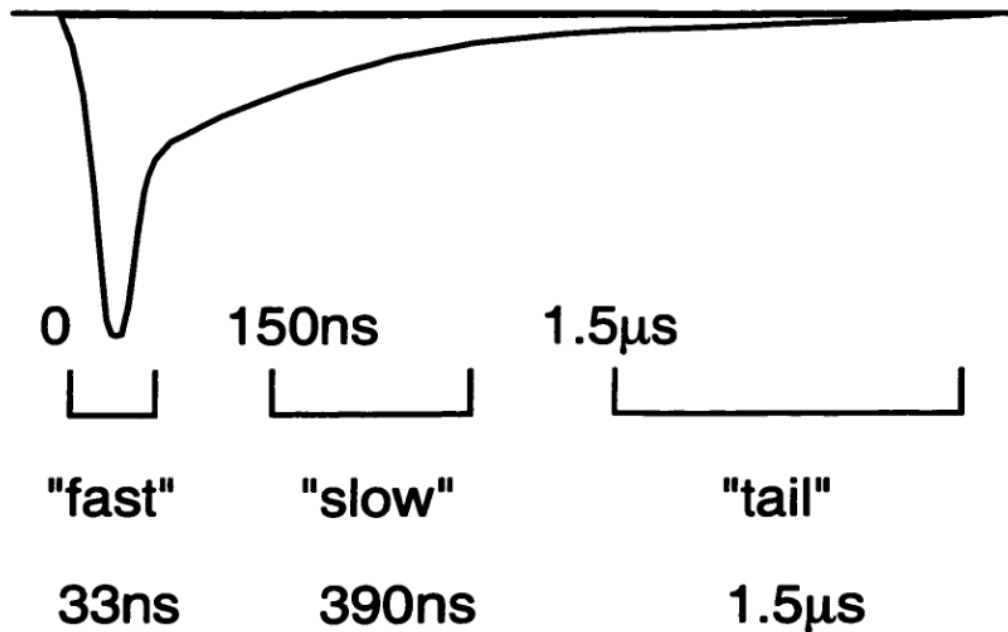


Figure 3.3: Schematic anode signal from the photomultiplier tube of a phoswich detector along with the timing and widths of the "fast", "slow" and "tail" gates.

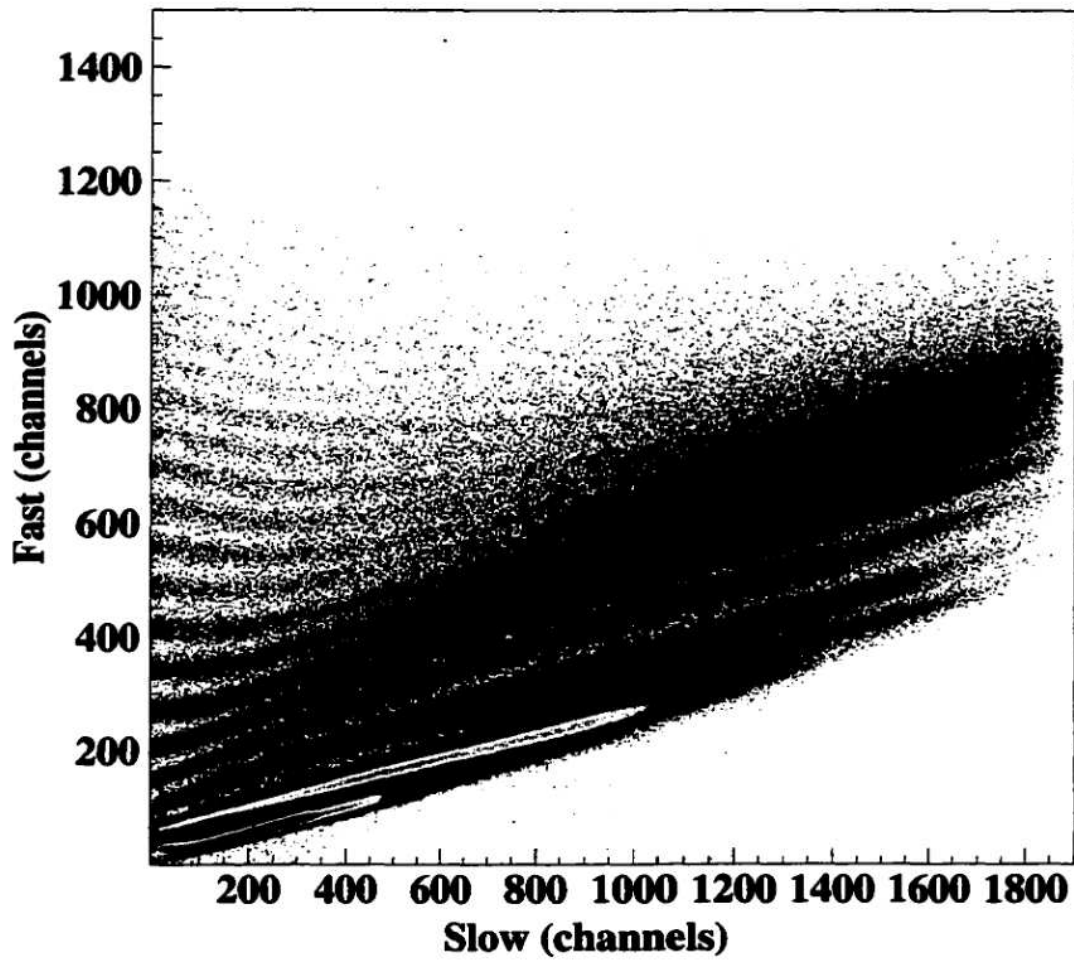


Figure 3.4: "Fast" versus "slow" spectrum measured in ring 13 ($\theta_{lab} = 16.6^\circ$)

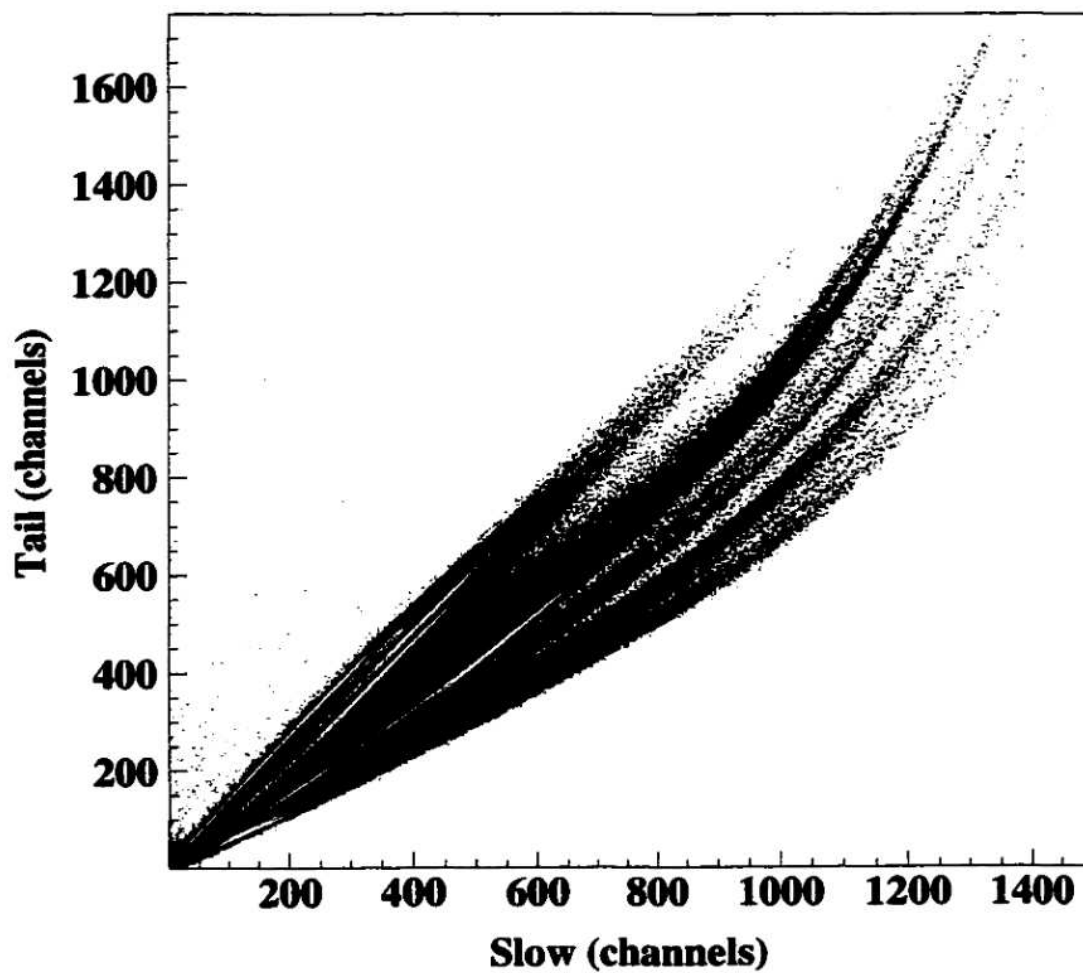


Figure 3.5: "Tail" versus "slow" spectrum measured in ring 5 ($\theta_{lab} = 45^\circ$)

3.3 Ring Counter

The ring counter consisted of a segmented 300 μm thick silicon detector backed by 2 cm of CsI(Tl). The front face of the silicon counter was segmented into 16 independent readout pie-shaped slices and the back face was segmented into four sections each having 16 independent readout annular rings. Scintillation of the CsI(Tl) crystals were readout by 16 independent photodiodes and the signals were processed by 16 independent pre-amplifiers and shaping amplifiers.

3.3.1 Energy Calibration of the Silicon Pie Detectors

The calibration of the 16 silicon pie segments was performed using a precision pulser. First, an Ortec pulser (model 448) [10] and a charge terminator were calibrated using a windowless ^{241}Am alpha source and a surface barrier detector. With the silicon detector connected to the pre-amplifier, the calibrated pulser and charge terminator delivered a charge equivalent of up to 2 GeV into the input of the pre-amplifier. A series of pulser dial settings was used to give peaks in the spectrum such that below channel 400 the peaks were 70 channels apart, above channel 3500 the peaks were 70 channels apart and the channels between 400 and 3500 the peaks were separated by 700 channels. The reason for this order of points was to determine if there was any non-linearity in the low or high end of the ADC. The pulser peaks were extracted from the spectra, plotted versus the pulser dial setting and fitted with a first order polynomial as is shown in Fig. 3.6. To determine the energy deposited in the silicon, a first order polynomial relating pulser setting to energy was used, which was calculated from data taken with the surface barrier detector and an ^{241}Am alpha source. As a result of using the incorrect switch settings on the precision pulser when calibrating the silicon pies, the relation of the pulser to energy was derived from using the calibration of the 140 MeV energy range. A scaling factor based on the 10 MeV, 100 MeV, 140 MeV, and 500 MeV energy ranges was used to get the full dynamic range.

In addition to the pulser calibration, the ring counter was moved into the beam and the following beams of known E/A were put into the ring counter: ^{36}Ar , ^{48}Ti , ^{52}Cr , ^{56}Fe , ^{60}Ni , $^{64,68}\text{Zn}$. However, before these beams could be used to verify the pulser calibration, knowledge of the thickness of the counter was needed. The nominal thickness quoted by

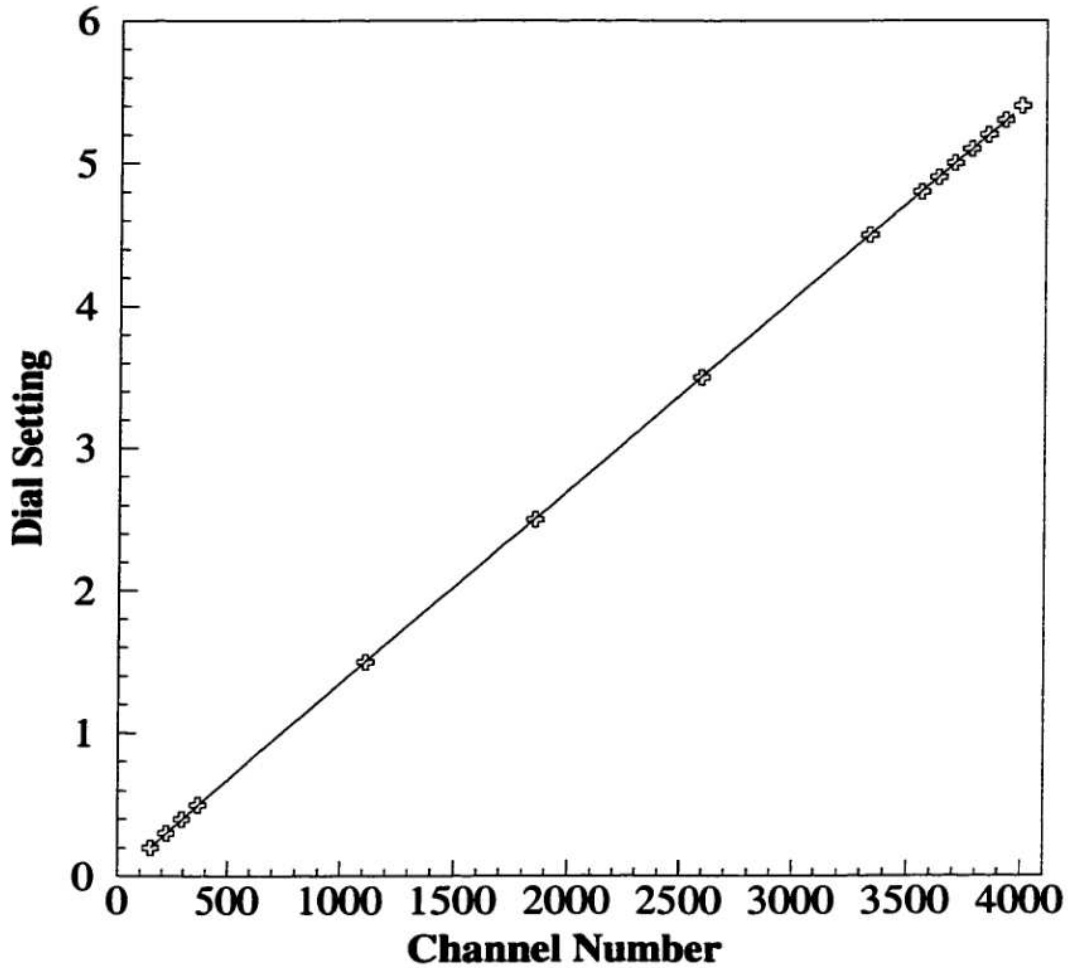


Figure 3.6: Relationship between dial setting on the precision pulser and raw channel number for the calibration of the silicon detectors.

Micron Semiconductor Ltd. is $300 \mu\text{m}$ [9]. To confirm the thickness experimentally, ^{36}Ar and ^{64}Zn beams were used. These two beams were chosen because of large statistics and the energy deposited in the silicon detector differed by approximately 360 MeV. The energy loss for the two projectiles passing through $290 \mu\text{m}$ and $302 \mu\text{m}$ of silicon was calculated using Ziegler's [12] energy loss code. Using the energy loss of each projectile calculated from the pulser calibration, the thickness of each pie section was determined from the ^{36}Ar and ^{64}Zn beams. These results were then averaged together for each pie section and ranged from 290

to 300 μm . Because the silicon is a single wafer, the thickness cannot be a step-like for the detector. To avoid using sixteen different values for the thickness, the average was taken of the 16 individual thickness. Displayed in Fig. 3.7 is calibration for a silicon pie detector. The line is the fit from the pulser, and the points are the various projectiles whose energy losses were determined from the energy loss code. With the exception of the ^{114}Cd elastic, all of the points lie on the line.

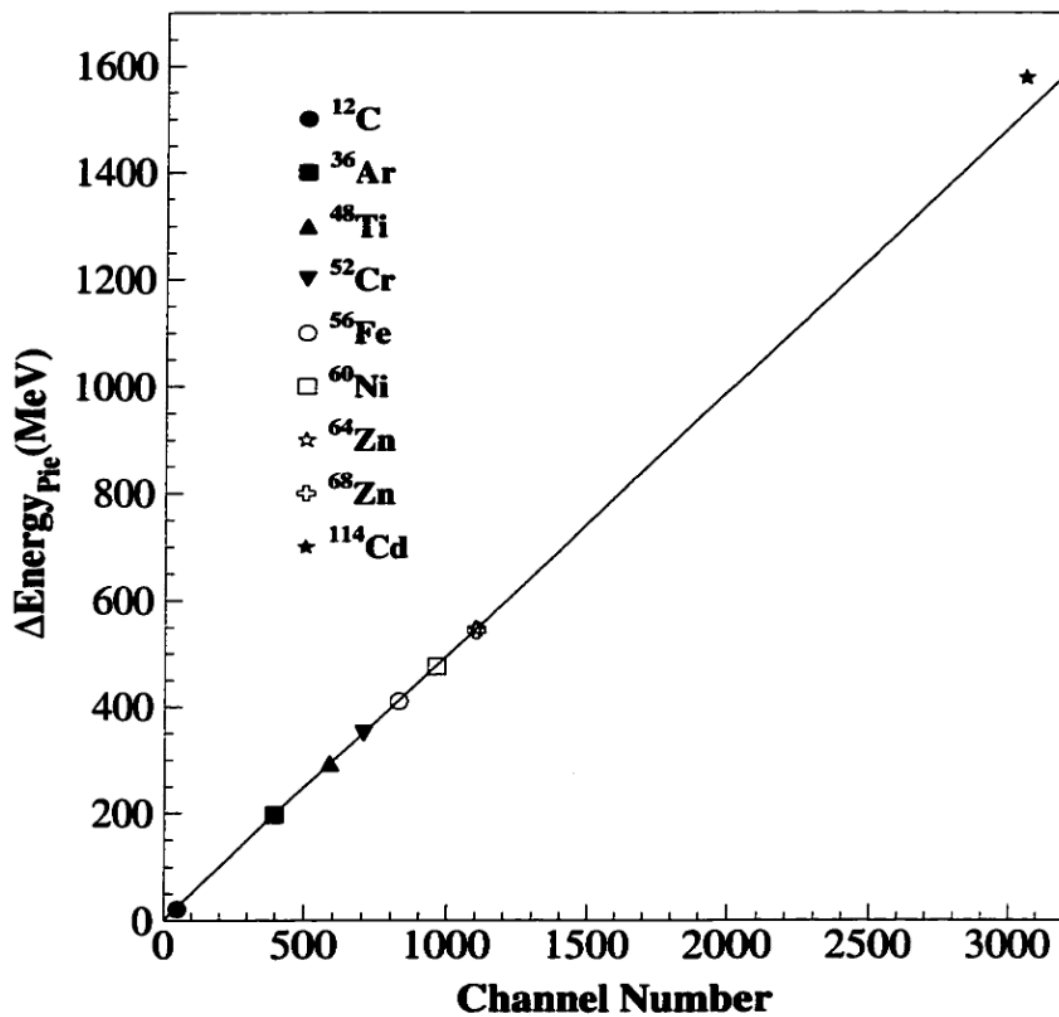


Figure 3.7: Silicon energy calibration with calibration data. The solid line is the fit from the pulser and the symbols are data from the calibration experiment.

3.3.2 Energy Calibration of the Annular Ring Detectors

In addition to the 16 pie detectors, the ring counter has 80 annular ring detectors. The 80 annular rings were not calibrated with the research pulser. Therefore, to calibrate the rings, it was necessary to derive a calibration from the silicon pie calibration. Spectra were generated of silicon pie energy in MeV versus ring in channel with the condition that per event only one pie and one ring per quadrant detected a fragment (256 total spectra). Calibration points were extracted every 50 channels on the x-axis (ring) and a calibration was calculated for each pie-ring combination using a first order polynomial. Figure 3.8 depicts the dependence of the energy deposited in the ring detector to the energy deposited in the pie detector.

During the energy calibration, an interesting phenomenon was discovered. When only one silicon pie per quadrant detected a fragment, either one ring or multiple rings had a signal. While examining the raw data event by event with the condition that only one pie had a signal, it was noticed that sometimes two adjacent rings had signals, and that the sum value of the two rings was about equal to the pie value. For every occurrence of only one ring having a signal, 15% of the time two adjacent rings split the signal. Figure 3.9 depicts the distribution where only one pie had a signal and the corresponding rings that also had signals. Ring three had the majority of the split signal. However, rings two and four had the other half of the split signal. The reason for this split signal was due to a leakage of charge from one ring to an adjacent ring. This phenomenon could occur if the fragment passed very close to the edge of one ring and the charge bled into the adjacent ring due to poor inter-ring isolation. To determine if this type of event was recoverable, the energies from the two adjacent rings were added together and compared to the pie energy. If the sum of the rings was within 20 MeV of the silicon pie energy, then the event was accepted. Figure 3.10 shows the distribution of the sum of the ring energies subtracted from the pie energy.

3.3.3 Energy Calibration of CsI(Tl) Detectors

Calibration of the CsI(Tl) detectors was more difficult than the calibration of the silicon pies. Three principal factors were responsible for making the calibration of the CsI(Tl) difficult: the number of data points from the calibration experiment was insufficient, there was no capability to inject a charge from the precision pulser into the photodiode pre-amplifier

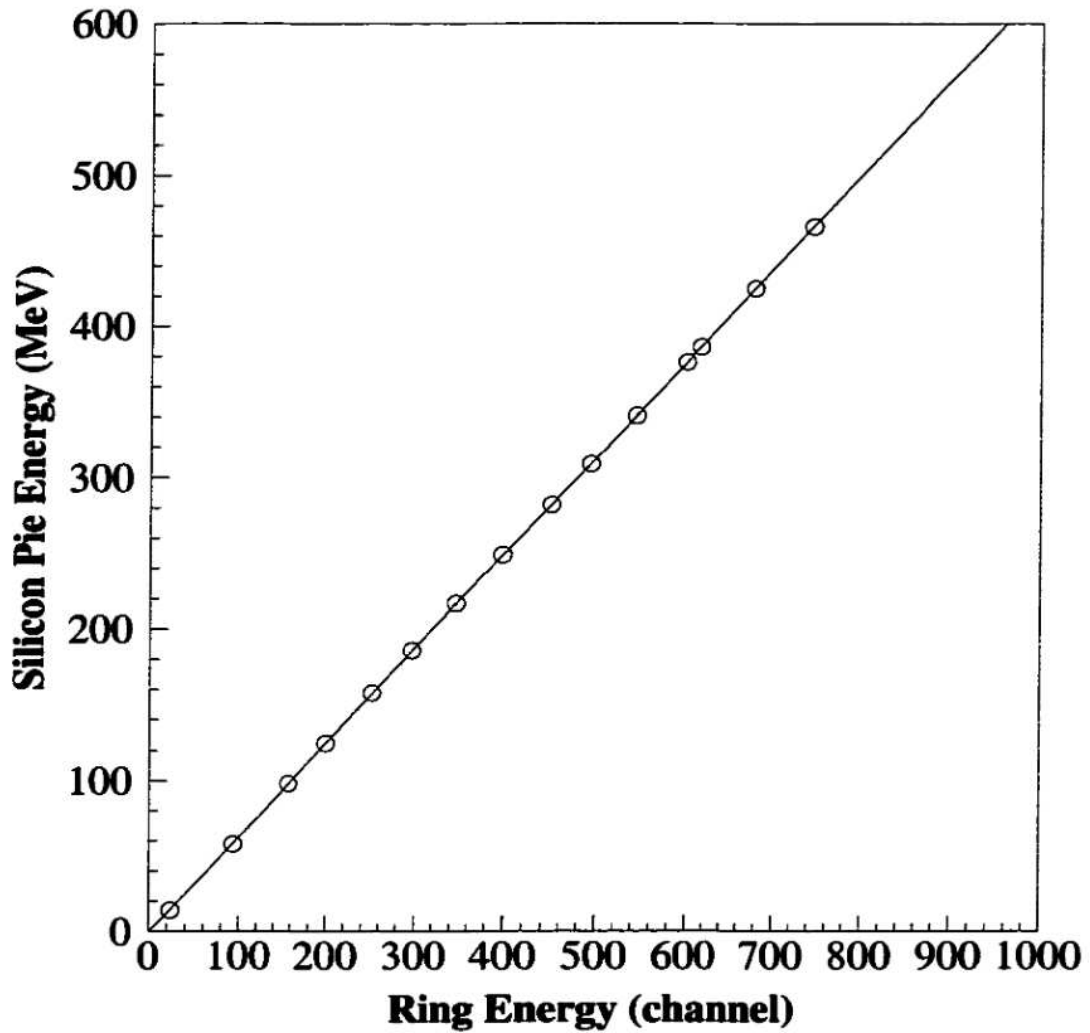


Figure 3.8: Dependence of the energy deposited in the ring detector to the energy deposited in the pie detector. Y axis is the pie energy in MeV and the x axis is the ring energy in channel number.

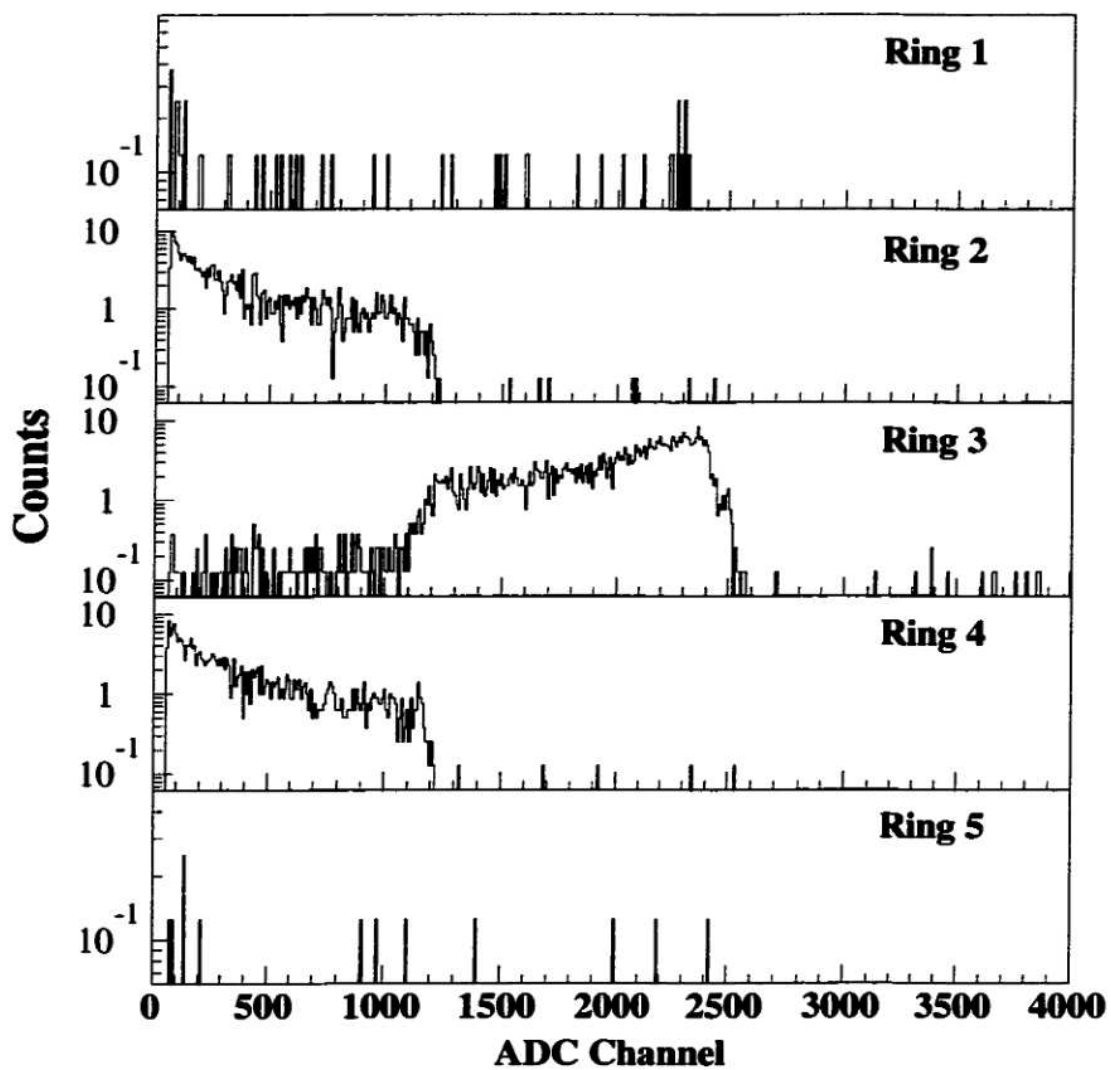


Figure 3.9: Distribution of signal leakage into adjacent rings. Ring 3 had the largest signal and the other rings had the remaining signal.

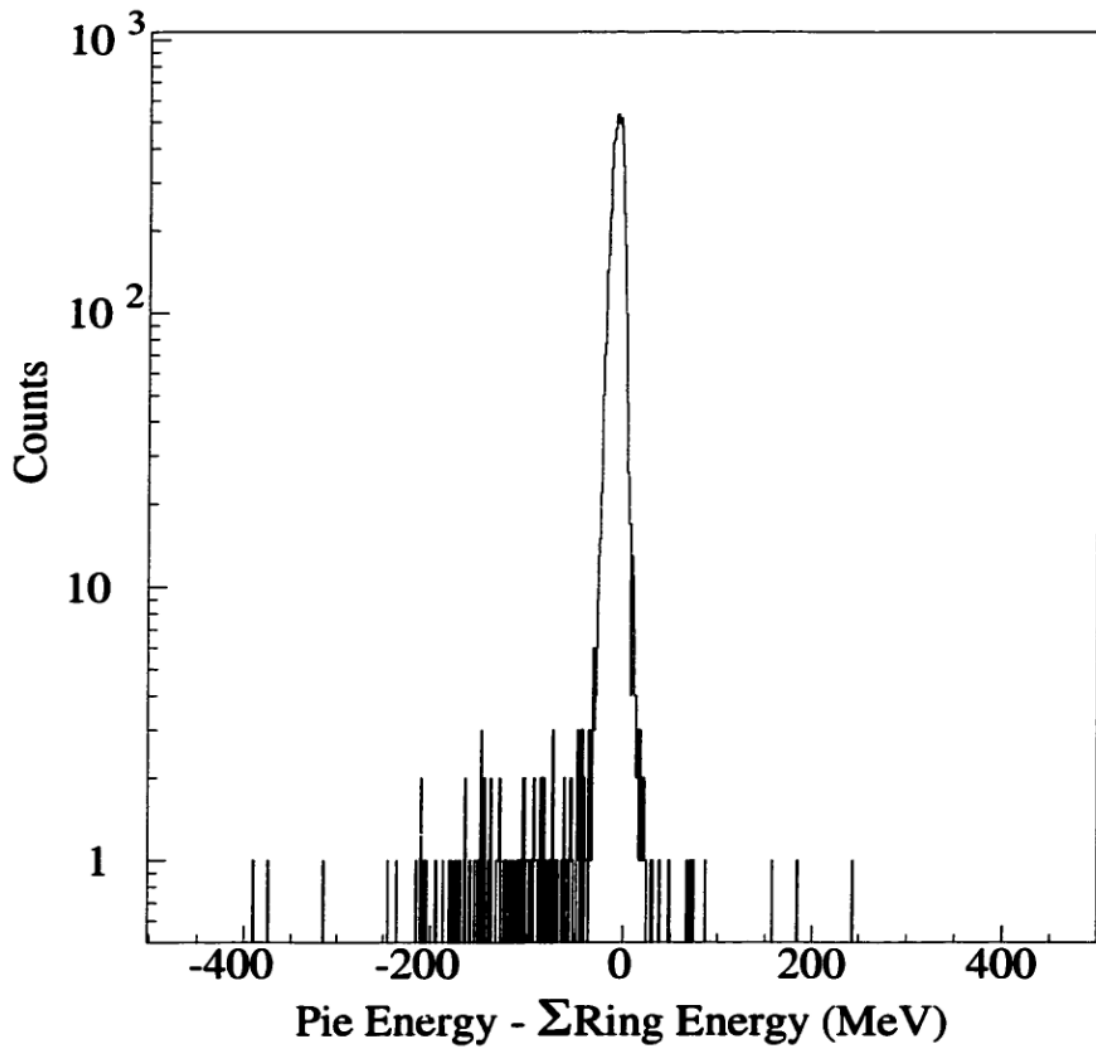


Figure 3.10: Distribution of pie energy minus the sum of ring energies.

input, and the only pulser input to the pre-amplifier was a test input, which is insufficient to provide a good absolute calibration. In order to calibrate the CsI(Tl) crystals, the particle identification lines in the Si-CsI(Tl) spectrum, which provide a continuous calibration, were employed. The calibrated energy loss, ΔE , from the silicon pie detector was related to an energy in the CSI(Tl) detector by utilizing energy loss calculations. Then the procedure of Mastinu [8] was applied. This technique involves using multiple data points of energy and light output to fit four parameters simultaneously using the function

$$L(E) = \gamma(E + E_i(e^{-E/E_i} - 1))$$

where $E_i = d_1 Z$ and $\gamma = d_2/Z + d_3 + d_4 Z$ where E is the energy deposited in the CsI(Tl), Z is the atomic number and d_1, d_2, d_3, d_4 are the four fit parameters. To obtain enough data points, the following procedure was used for each CsI(Tl). Using an uncalibrated 1024 x 1024 two-dimensional plot of silicon pie in channel versus CsI(Tl) in channel, a two channel wide gate in constant CsI(Tl) channel was drawn at the following intervals: 50, 100, 200, 300, 400, 500, 600, 700, 800. The contents of this gate were then projected onto the silicon axis and the centroid of each peak was determined. The value from each centroid was then converted to energy. Along with the centroid energy, the Z of each peak was also determined by assigning a Z to each band starting from the Cd elastic peak.

Before determining the energy deposited in the CsI(Tl) from energy loss calculations, the mass of the fragment was needed. However, the resolution of the ring counter silicon was only good enough to be able to separate the Z of the products. To estimate the mass of the products, a modified version of the EPAX equation [11] was used. A modified version was used because the EPAX equation did not reproduce the N/Z ratio of the neutron-rich ^{114}Cd projectile. Figure 3.11 shows the function that was used to determine the mass. The asterisk is the N/Z ratio for ^{114}Cd the dashed line is the EPAX line. The asterisk and the EPAX function were joined by a line drawn from $Z = 48$ to $Z = 40$ (zirconium). To create a smooth function between the EPAX line and the projectile, a seventh order fit was used (solid line). The same procedure was used for the ^{106}Cd projectile.

Having estimated the mass, calculated the silicon energy and determined the Z , the energy deposited in the CsI(Tl) was then calculated and a set of calibration points for the CsI(Tl) was generated. Displayed in Fig. 3.12 is the result for $Z = 5, 10, 15, 20, 25, 30, 35$,

40, and 45 which used a global fit of all the calibration data. A lookup table of light versus energy was created for each CsI(Tl) crystal from the light output function.

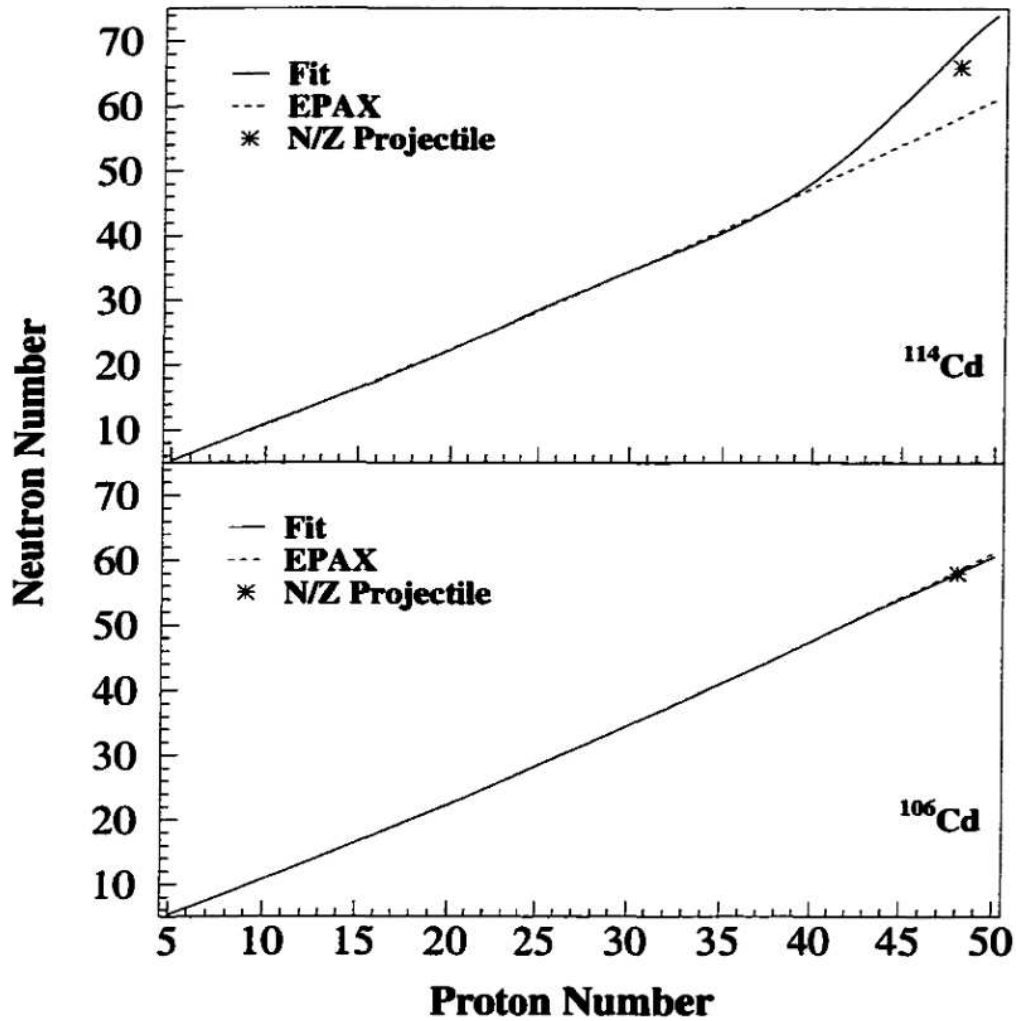


Figure 3.11: Fits used to determine the mass number of the reaction products. The dashed line is the EPAX function, the asterisk is the N/Z of the projectile and the solid line is the fit that was used.

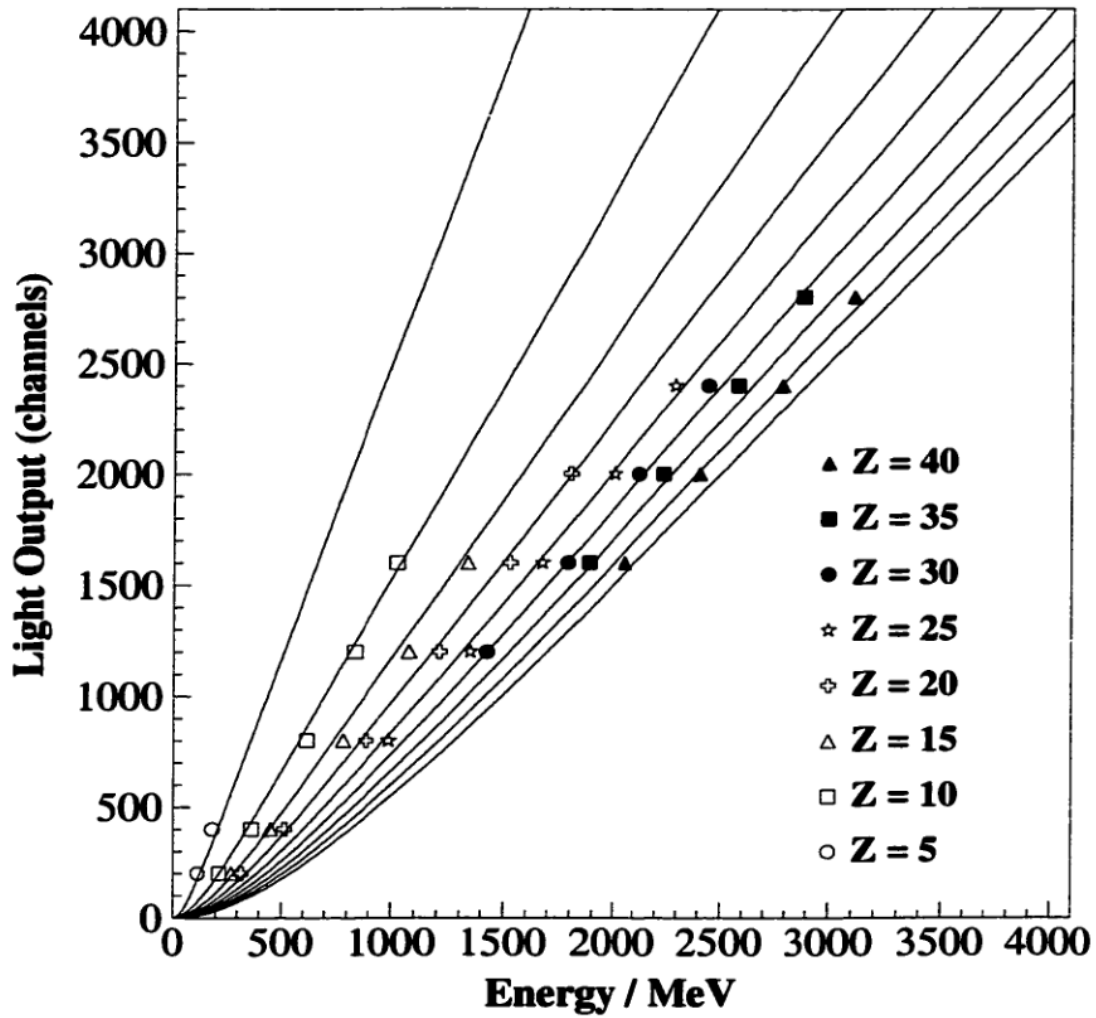


Figure 3.12: Results of the global fit using Mastinu's procedure. The solid lines are the functional fit, in steps of every five Z starting with $Z = 5$.

3.3.4 Particle Identification

To identify the atomic number of each fragment the ΔE -E technique was used. This technique is based on the dependence of the energy loss of charged fragment passing through matter $\Delta E \sim AZ^2/E$ where A is the mass number, Z is the atomic number and E is the energy of the incident fragment. Displayed in Fig. 3.13 is the ΔE -E plot for the relationship of silicon energy in MeV to CsI(Tl) in raw channel. The distinct bands clearly show the excellent Z resolution from Z = 2 to Z = 50. Some of the other features evident in the spectra are the elastic peak located at the upper right ($E_{CsI} \sim 3700$ ch., $E_{Si} \sim 1600$ MeV) and the light haze of random data points to the right of the bulk of the data which extend to higher CsI values ($E_{CsI} \geq 3000$ ch.). These latter data correspond to events when a heavy fragment was detected in coincidence with a light fragment or a neutron. Individual gates were drawn on each of the bands of data for all of the 16 Si-CsI(Tl) ΔE -E spectra for charges from Z = 2 to Z = 51. The atomic number was then interpolated between the gates yielding a non-integer value for Z. Depicted in Fig. 3.14 is the particle identification (PID) spectrum for a single Si-CsI(Tl) detector. The resolution of a single peak is $\approx 0.25Z$. When the sixteen individual PID spectra are summed together correcting for the down-scale factor, the result is shown in the top of Fig. 3.15. The bottom panel of Fig. 3.15 depicts the Z distribution in the ring counter. The dashed line represents the distribution when the MB/MW was the event trigger, the dotted line represents the distribution when the ring counter was the event trigger scaled by the down-scale factor, and the solid line is the sum of the two trigger conditions.

3.3.5 Consistency Checks

Once the silicon and CsI(Tl) detectors were calibrated, the validity of the calibration for the entire period the experimental data was collected was checked. Of particular concern was the fact that the experiment was performed in two periods of beam time, separated by two weeks, whereas the calibrations were performed using data from the calibration experiment (performed two weeks after the data collection) and data from the second beam time. A continuously cycling pulser was attached to the test input of the pre-amplifier during the experiment. To check the stability of the CsI(Tl) electronics, the centroid of each pulser peak was extracted for a run at the end of the first part and for a run at the beginning

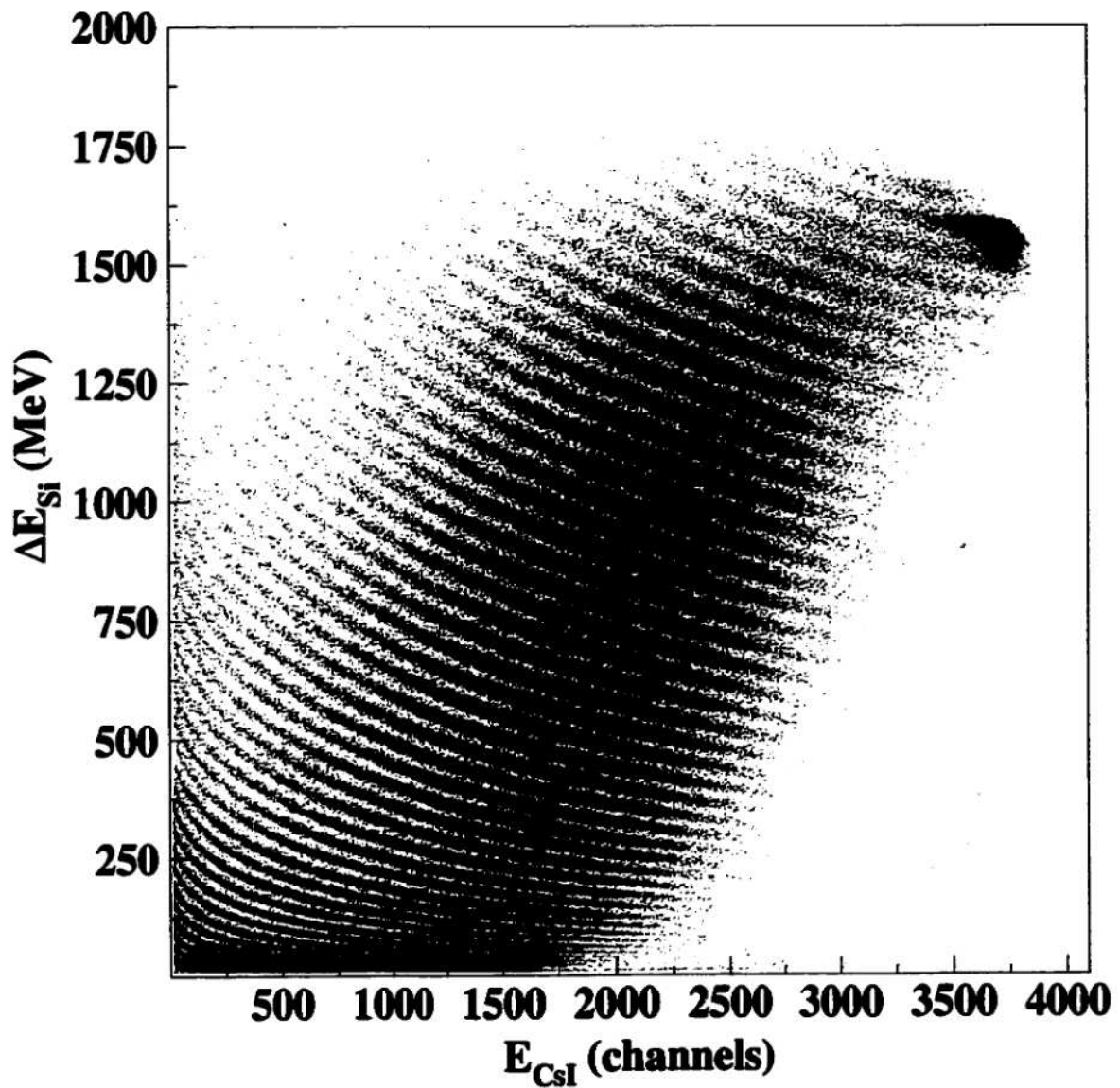


Figure 3.13: Two-dimensional plot used for the particle identification. Silicon energy in MeV is on the y-axis and raw CsI(Tl) in channel number is on the x-axis.

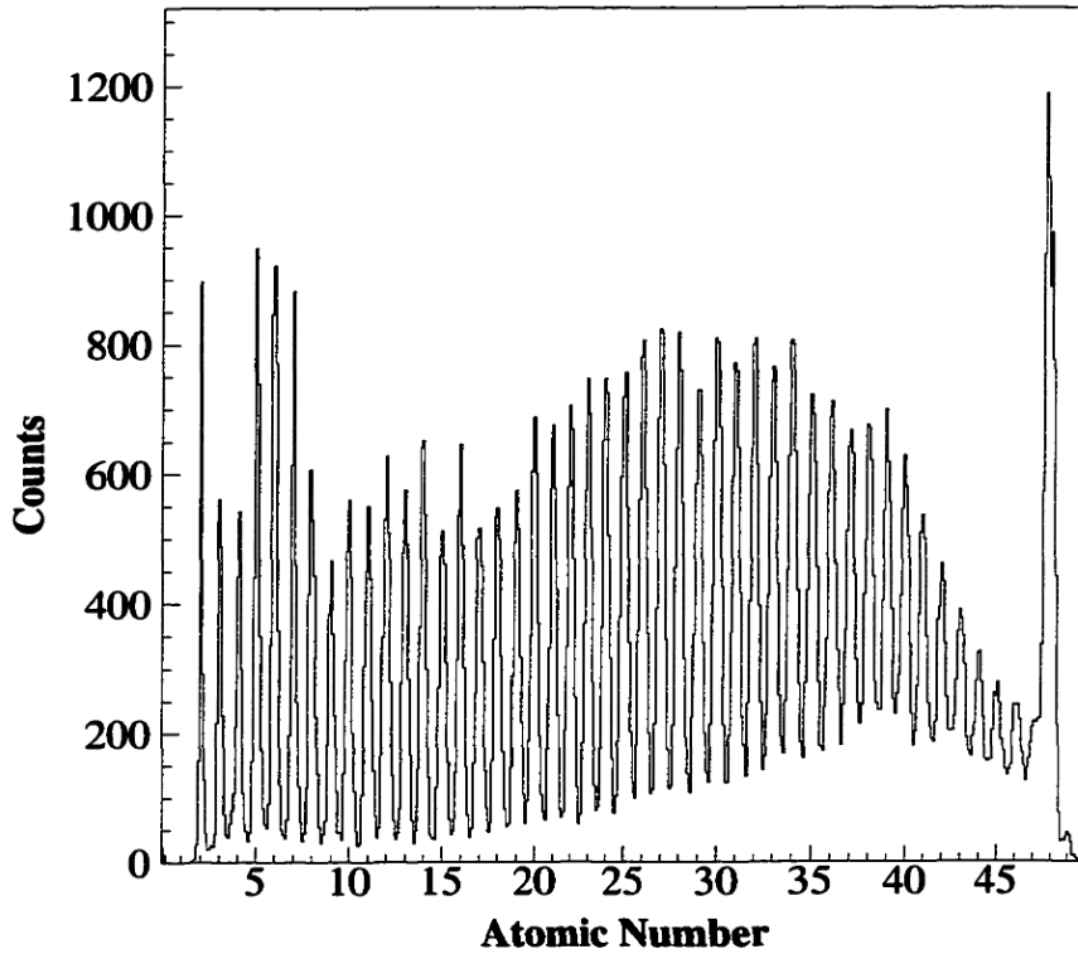


Figure 3.14: One-dimensional spectrum of the particle identification for a single silicon pie-CsI(Tl) combination.

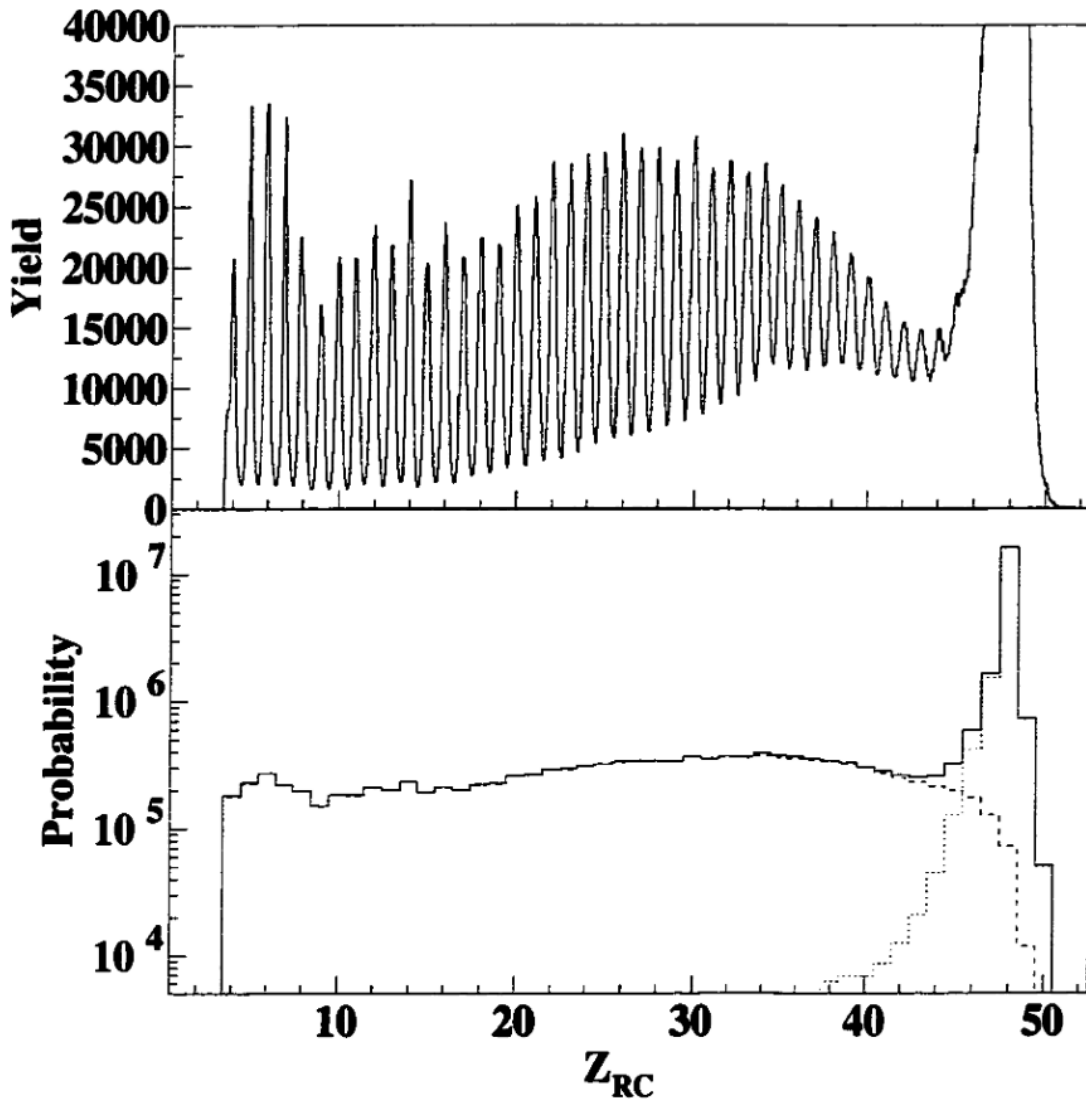


Figure 3.15: One-dimensional spectra of the particle identification summed over the entire ring counter. Spectrum showing resolution for each Z corrected for the relative weights of the experimental triggers (top). Z distribution for the reaction (bottom). The dashed line represents the distribution when the MB/MW was the event trigger, the dotted line represents the distribution when the ring counter was the event trigger and the solid line is the sum of the two trigger conditions.

of the second part. The centroids for each run were plotted against pulser setting and fit with a first order polynomial. Shown in Fig. 3.16 (top panel) is the ratio of the slopes from the pulser fits expressed as a percent difference from the first part of the experiment to the second part as a function of CsI(Tl) detector number. For comparison the ratio of the elastic peak for the same two runs is displayed in Fig. 3.16 (middle panel). The results indicate that for the elastic peak and the test input pulser, the gain of the CsI(Tl) is relatively constant between the two parts. However, based on the elastic peak, the silicon pies have a different gain as shown in Fig. 3.16 (bottom panel), which varies from -3% to 1.5%. The gain changes are likely the result of different thermal conditions for the detectors and electronics for the two separate segments of the experiment. Differences in temperature of the pre-amplifiers can alter the gain, while the light output from a CsI(Tl) crystal has a known temperature dependence.

The matching of parts one and two for the silicon pies had several problems using either the pulser or ^{114}Cd elastically scattered peak. The test input pulser could not be used because the amplitude of the pulser signal was too small resulting in data in only the lower ten percent of the ADC range. In addition, to match the entire silicon energy range based on the single data point from the elastic peak is not feasible and could over or under correct the gain matching at low channels. Instead, the calibrations from the second part were matched to the first part using experimental data. Two dimensional plots of silicon pie in channel number versus CsI(Tl) in channel number were created from parts one and two. Gates were then drawn in constant CsI(Tl) channel (after confirming that the CsI(Tl) were matched using the pulser data as described previously) and projected onto the silicon axis for all spectra. After determining the centroids and calculating the silicon pie energies, the energies from part one were plotted against the energies from part two, giving a relationship between part one and part two. The data was fit with a first order polynomial with percent errors estimated from the resolution of the silicon bands in the raw ΔE -E spectrum. Specifically, if the silicon energy was less than 150 MeV, the error was 8%, between 150 MeV and 500 MeV the error was 5% and greater than 500 MeV the error was 3%.

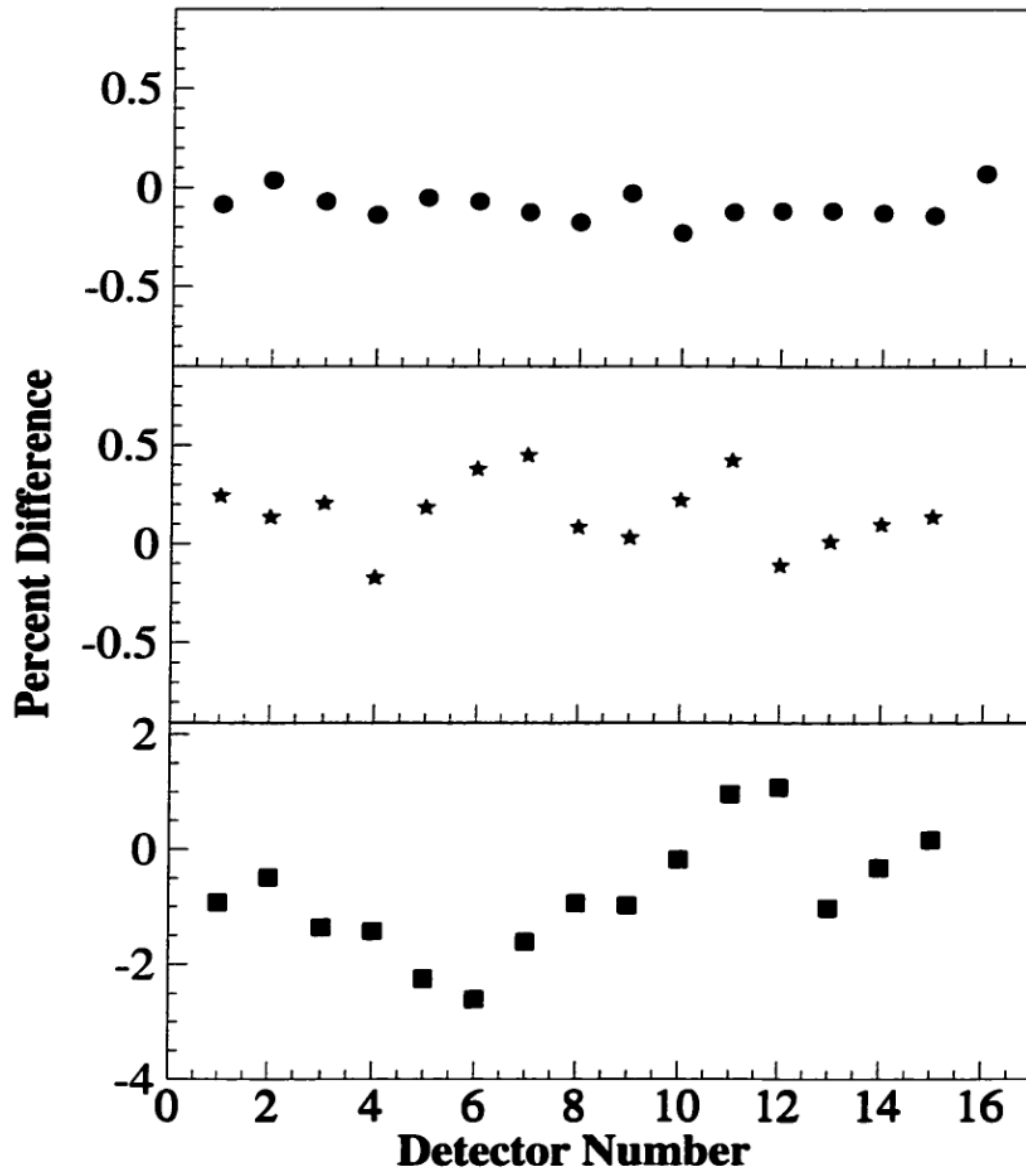


Figure 3.16: Percent difference in the gain changes of the CsI(Tl) crystals (top and middle panels) and silicon detectors (bottom panels) from parts one and two of the experiment. Comparison using pulser data (top) and elastically scattered ^{114}Cd (middle and bottom)

References

- [1] R.T. de Souza *et al.*, Nucl. Instr. Meth. A **295**, 109 (1990).
- [2] T.M. Hamilton, Ph. D. Thesis, Indiana University (1996).
- [3] B. Davin *et al.*, Nucl. Instr. Meth. A **473**, 302 (2001).
- [4] R.S. Storey *et al.*, Proc. Phys. Soc. **72**, 1 (1958).
- [5] J.A. Biggerstaff *et al.*, Nucl. Instr. Meth. **10**, 327 (1961).
- [6] J. Alarja *et al.*, Nucl. Instr. Meth. A **242**, 352 (1986).
- [7] N. Colomma *et al.*, Nucl. Instr. Meth. A **321**, 529 (1992).
- [8] P. F. Mastinu, *et al.*, Nucl. Instr. and Met. A **338**, 419 (1994).
- [9] Micron Semiconductor Limited, Lancing, Great Britain.
- [10] PerkinElmer Instruments, Seven Hills, OH.
- [11] K. Sümmerer, *et al.*, Phys. Rev. C **42**, 2546 (1990).
- [12] TRIM, J.F. Ziegler, <http://www.research.ibm.com/ionbeams/home.htm>.

Chapter 4

General Characteristics of PLF*

Decay

4.1 Introduction

It is well established at $E/A \sim 5 - 10$ MeV that during a peripheral or mid-central collision the projectile and target nuclei interact by exchanging mass, charge and energy [1]. The projectile-like fragment and target-like fragment (PLF and TLF respectively), formed as a result of the interaction, separate after less than a full rotation. Both product nuclei may be highly excited due to the interconversion of kinetic energy of relative motion into intrinsic excitation. At these low bombarding energies, the de-excitation of the PLF and TLF occurs after the two heavy nuclei have reached essentially their full acceleration. Thus the reaction can be thought of in two distinct phases: the initial interaction involving proton, neutron exchange and the buildup of excitation energy and the subsequent de-excitation of the two reaction partners. In contrast to collisions with incident energies near the Coulomb barrier, it has been proposed that at intermediate energies [2] the excited projectile-like fragment (PLF*) may decay while still in close proximity to the TLF. Consequently, the target's field may affect the decay of the PLF*, causing the PLF* to favor decay along the axis separating the PLF* and TLF*. If however, the PLF* decay occurs when the target's field has a negligible effect on the PLF*, i.e. there is no proximity effect, the PLF* will decay isotropically in a plane perpendicular to the spin axis of the PLF*. In this chapter, we

attempt to characterize the decay of an excited projectile-like fragment from the measured observables. In particular, after examining the general reaction characteristics, we focus on charge-charge correlations and charge-relative velocity correlations.

4.2 General Reaction Characteristics

The collision of a projectile nucleus with a target nucleus can be described by considering the impact parameter of the collision as depicted in Fig. 4.1. If the impact parameter, b , is much larger than the sum of the radii of two nuclei, $(R_P + R_T)$, the projectile is elastically scattered, i.e. the interaction is purely electromagnetic. In this case, the atomic number and mass number of the projectile are unchanged and the final kinetic energy is simply governed by Rutherford scattering. When $b \leq (R_P + R_T)$, a grazing collision occurs in which a few nucleons are exchanged between the colliding nuclei. Hence, the atomic number and mass number of the two nuclei is changed and some kinetic energy is dissipated. As $(R_P + R_T)$ becomes even smaller, the transfer of mass, charge and damping of energy increases and can become substantial – several hundred MeV. Reactions occurring under these conditions are classified as damped collisions. Some defining characteristics of a damped reaction are: the process is binary; the reaction products have an identity (atomic and mass numbers) similar to the reactants; there is a significant damping of the initial kinetic energy [1]. For the reaction $^{114}\text{Cd} + ^{92}\text{Mo}$ at $E/A = 50$ MeV, our primary focus is addressing what can be learned about the decay of the highly excited projectile-like fragment (PLF*)?

Depicted in Fig. 4.2 are the kinetic energy spectra for $Z = 10$ to $Z = 48$ measured for $2.1^\circ \leq \Theta_{lab} \leq 4.2^\circ$ in the reaction $^{114}\text{Cd} + ^{92}\text{Mo}$. For the Cd ($Z = 48$) energy spectrum there is a pronounced narrow peak with a tail extending to lower energies. This peak arises from the elastically scattered projectiles that dominate the cross-section. As the Z decreases from 48, the shape of the energy spectra changes from a peak with a low energy tail to an approximately bell shaped function. The appearance of a bell shaped distribution becomes prevalent for all $Z \leq 44$. For the distributions with $Z \leq 20$ the bell shaped distribution changes to an asymmetric distribution (increase in yield of lower energy fragments) resulting from a different process. Starting with Ru ($Z = 44$) and continuing to smaller atomic numbers the most probable energy decreases approximately linearly with Z ,

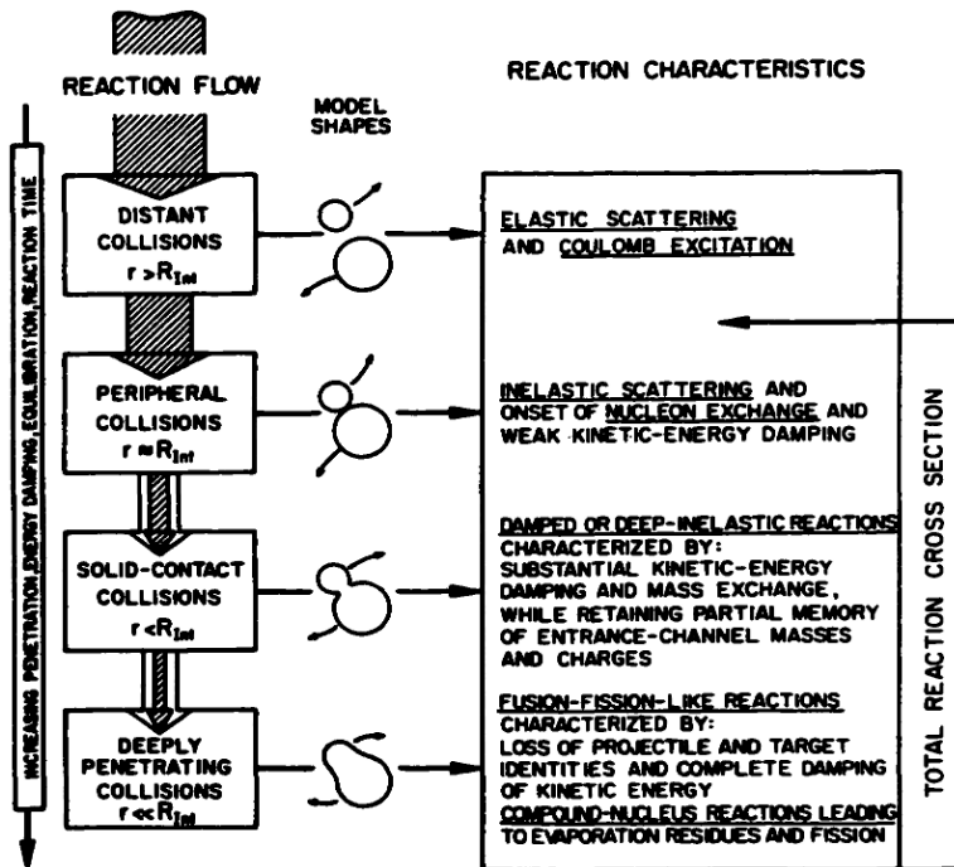


Figure 4.1: Classification of projectile-target collisions based on impact parameter. The distance of closest approach between the two nuclei is represented by r . From Ref. [1].

represented by the dotted line.

To illustrate the dependence of energy on scattering angle, Fig. 4.3 shows the relationship between the energy of the detected fragment and the laboratory angle at which the fragment was detected for $2.1^\circ \leq \theta_{lab} \leq 4.2^\circ$. This type of plot is similar to a Wilczynski [4] contour diagram; however, a Wilczynski diagram uses center-of-mass angle and energy, whereas Fig. 4.3 uses laboratory values. Results at lower incident energies used a Wilczynski diagram

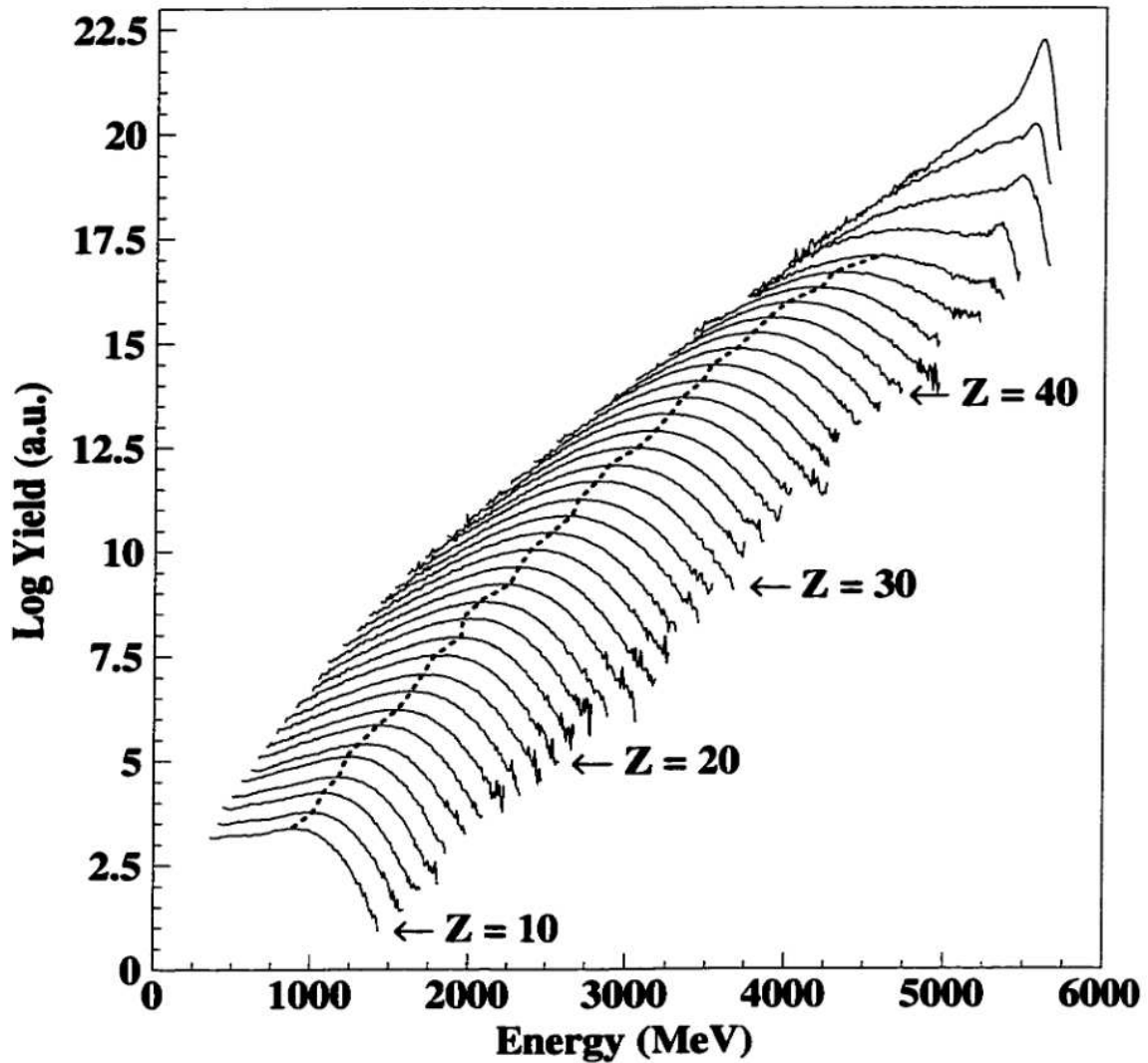


Figure 4.2: Measured kinetic energy spectra for $Z = 10$ to $Z = 48$ for $2.1^\circ \leq \Theta_{lab} \leq 4.2^\circ$ in the reaction $^{114}\text{Cd} + ^{92}\text{Mo}$. The dotted line indicates the most probable energy for each Z .

to determine whether the projectile and the target nuclei were in contact for more than one rotation [4]. The peak (energy = 5600 MeV) in the cross section (elastically scattered ions) extends to about 2.5° , after which the cross section decreases sharply as the angle increases. This decrease in the elastic cross-section is directly related to the onset of non-elastic nuclear reactions. The decrease in the cross section occurs at the quarter point angle,

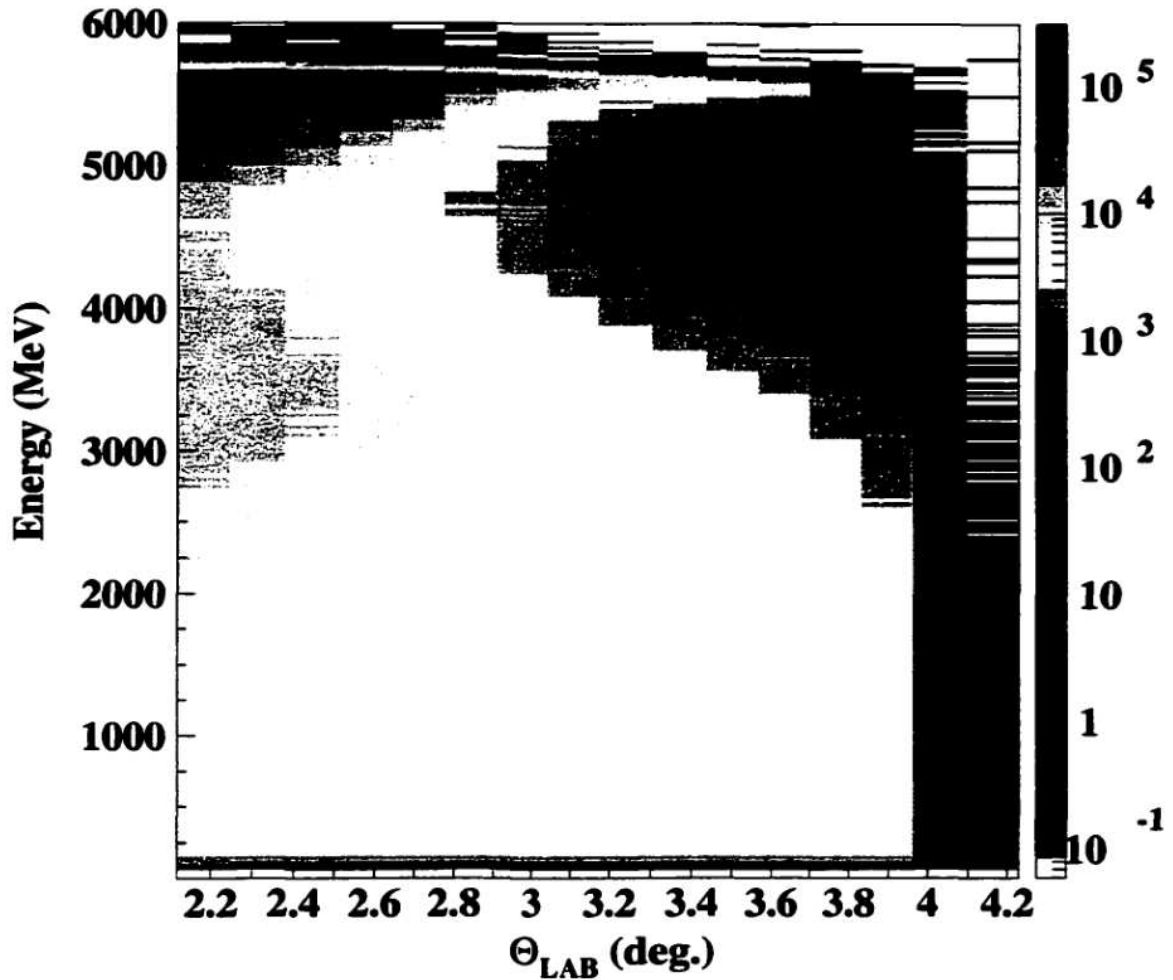


Figure 4.3: Relationship between the energy of the detected fragment and the laboratory angle at which the fragment was detected.

$\Theta_{1/4}$ (the angle in the center-of-mass for which the ratio of elastic cross section to Rutherford cross-section is 0.25). For the $^{114}\text{Cd} + ^{92}\text{Mo}$ reaction systematics predict $\Theta_{1/4} = 2.4^\circ$ [5]. A second broad ridge of cross section starts at $E \sim 3750$ MeV and extends to lower energy as θ_{lab} increases. This ridge can be attributed to target-projectile interactions when the detection is on the side opposite of the interaction [4]. While the dissipated energy is the most direct means of determining the total excitation of the system (both PLF* and TLF*), as the dissipation is linked to the transport of nucleons between projectile and target nuclei,

one can also examine the atomic number as a measure of the dissipation. This approach has a few drawbacks however. Foremost is the fact that this variable is not sensitive to dissipation due to neutron exchange. Secondly, subsequent decay (e.g. charged-particle emission) may alter the Z of the PLF distorting the relationship between Z and the incurred dissipation.

The relationship between Z_{RC} and θ_{lab} is depicted in Fig. 4.4. Despite the limitations mentioned above, the same general trends evident in Fig. 4.3 are observed. For $Z = 48$ the cross section decreases sharply for $\theta_{lab} \geq 2.8^\circ$ as the angle increases. The phenomenon of orbiting can also be distinguished. The maximum of the broad ridge starts at approximately $Z = 38$ and continues to lower values of Z as the angle increases. It is interesting to note that for $4 \leq Z \leq 10$ that the yield for each Z is approximately constant as the angle increases.

The three previous figures represented the relationships for all fragments detected in the ring counter. One might imagine however, that if the PLF* was to decay after separating from the target, multiple fragments might be detected within the ring counter. In order to investigate this idea we examine in Fig. 4.5 the probability of detecting a given number of fragments within the ring counter (N_{RC}). The distribution shown in Fig. 4.5 is selected on fragments in the ring counter with $Z \geq 4$ and at least 3 charged particles in the MB/MW and LASSA ($N_C \geq 4$). As is evident in Fig. 4.5, the most probable occurrence is that only one fragment is detected in the ring counter. The probability for detecting two or three fragments in the ring counter is 2.1% and 0.012%, respectively. Clearly this probability, particularly for the case of two fragments in the ring counter, is not negligible. If the two and three fragment cases are breakups of a single PLF*, then the sum of the charges for the events should be less than the projectile Z (48).

Displayed in Fig. 4.6 is the probability distribution for the sum charge for all fragments in the ring counter for a given event. The three distributions presented indicate the behavior of the sum charge distribution when $N_{RC} = 1$ (solid), $N_{RC} = 2$ (dashed) and $N_{RC} = 3$ (dotted). The vertical offset of the three distributions with respect to each other represents the probability of each class of events uncorrected for detector efficiency. In the range $10 \leq \Sigma Z_{RC} \leq 44$, the distributions for $N_{RC} = 2$ and $N_{RC} = 1$ have fairly similar shapes. The similarity of the two distributions can be understood if the size of the parent was similar for both $N_{RC} = 2$ and $N_{RC} = 1$. Clearly evident for the case $N_{RC} = 2$ is that the distribution

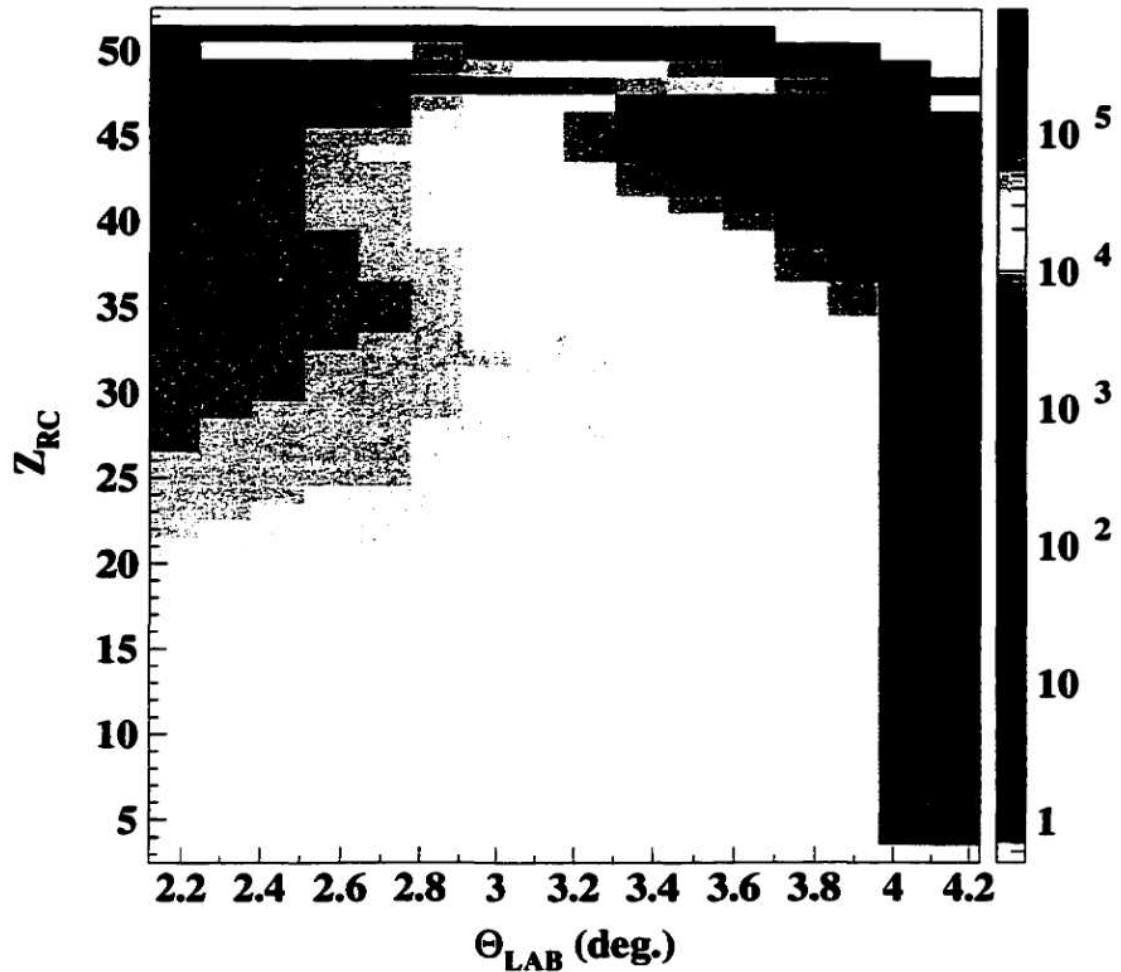


Figure 4.4: Relationship between the atomic number of the detected fragment and the laboratory angle at which the fragment was detected.

extends well beyond $\Sigma Z_{RC} = 48$. In fact, the distribution extends to $\Sigma Z_{RC} = 98$ with a peak at $\Sigma Z_{RC} = 96$. One can understand this peak at $\Sigma Z_{RC} = 96$ as the detection of two projectile nuclei ($Z = 48$) as the result of two collisions. The events when ΣZ_{RC} is greater than 51 can be attributed to such accidental coincidences. The probability of such accidental coincidences can be estimated by examining the relative probability of the $\Sigma Z_{RC} = 48$ and $\Sigma Z_{RC} = 96$ peaks in the $N_{RC} = 1$ and $N_{RC} = 2$ cases respectively. Comparison of these yields indicates an accidental coincidence probability of 0.03%. For events when $N_{RC} = 3$,

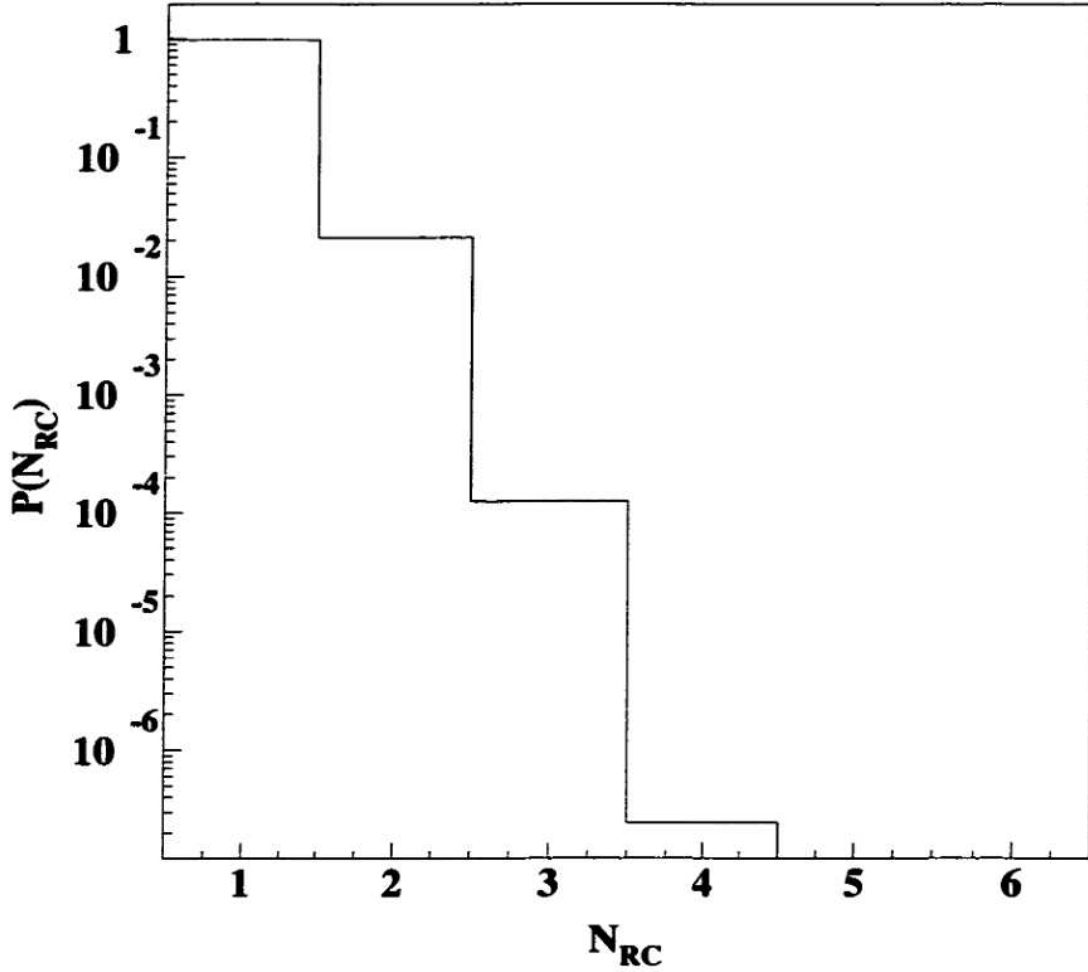


Figure 4.5: Multiplicity distribution of fragments detected in the ring counter.

the distribution is almost symmetric, with the maximum value being $\Sigma Z_{RC} = 33$. The lower cutoff in ΣZ_{RC} results from the requirement that all three fragments have a $Z \geq 4$. The few statistics available for this case over the duration of the experiment limited our use of these events.

The multiplicity of charged particles emitted is an alternate means of determining the excitation of the di-nuclear system [6, 7]. Figure 4.7 depicts the charged particle multiplicity distributions (N_c). Represented as a solid line is the inclusive multiplicity distribution corresponding to detection of at least three charged particles in the Miniball/Miniwall array

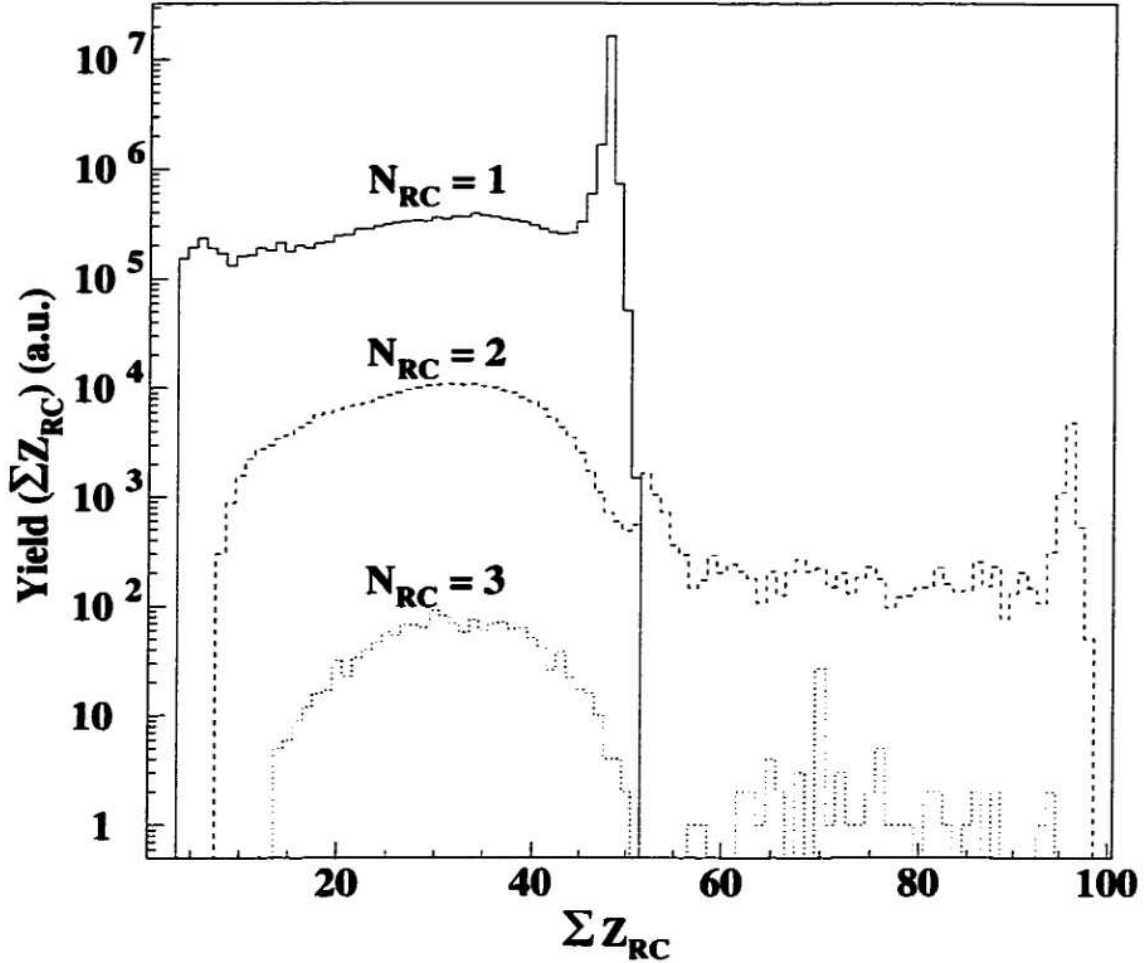


Figure 4.6: Probability distributions for the sum charge ΣZ_{RC} for all fragments detected in the ring counter for a given event when one (solid), two (dashed) or three (dot-dash) fragments were detected.

or detection of at least one fragment in the ring counter with $Z \geq 4$. This distribution is typical of multiplicity distributions for heavy-ion nuclear reactions at intermediate energies. It is broad and relatively flat with a roughly exponential tail extending to the highest multiplicities. A peak at the lowest multiplicities corresponds to the most peripheral reactions. In the N_c distributions selected on $N_{RC} = 1, 2, 3$ are represented by the dashed, dotted and dot-dash lines respectively. In generating all these distributions elastically scattered

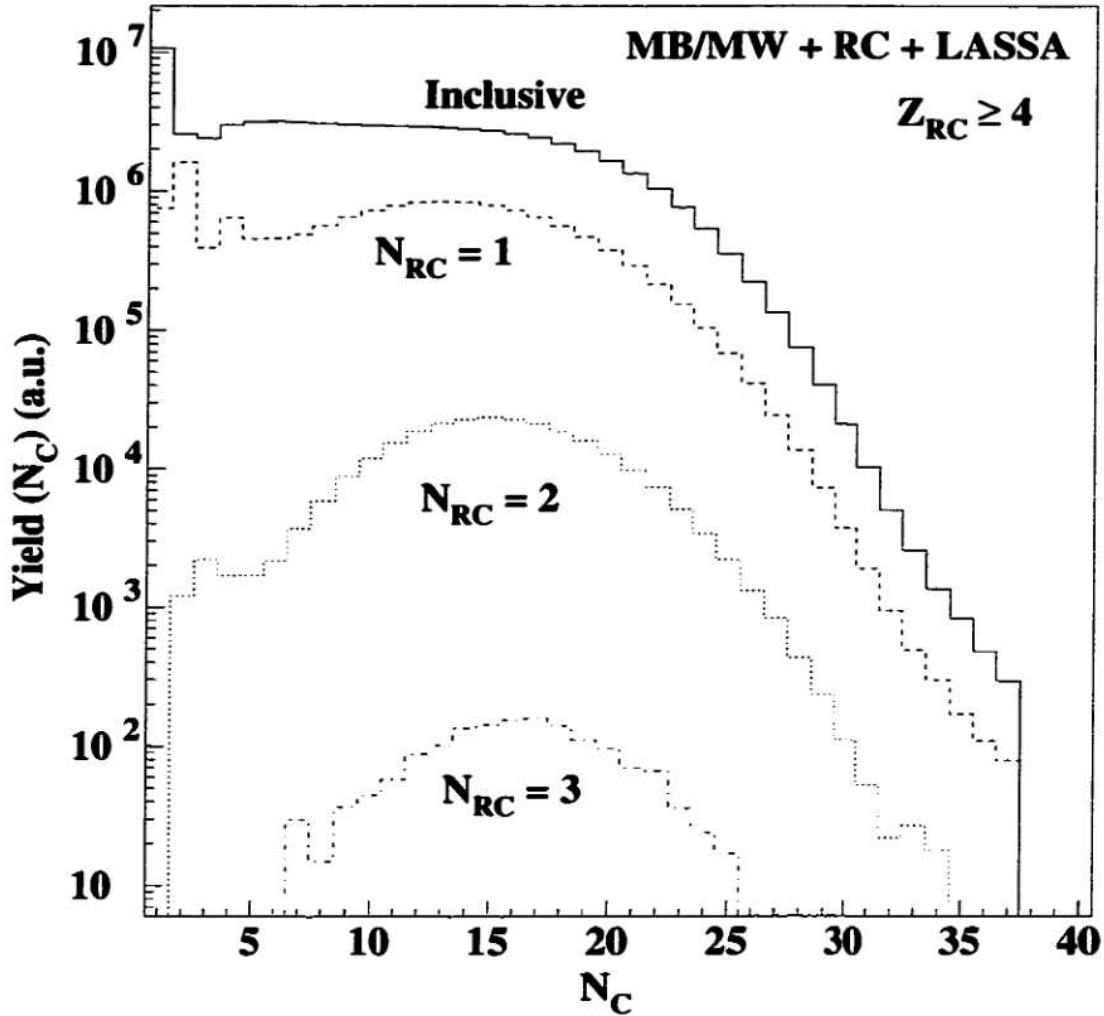


Figure 4.7: Distributions of the charged particle multiplicity, N_c , both inclusive and selected on the number of fragments detected in the ring counter. The smallest atomic number detected in the ring counter used in these distributions is four.

^{114}Cd are excluded. The peaks in the inclusive and one hit case at $N_c \leq 2$ arise from grazing collisions where one proton is transferred between the target and projectile. The three distributions where a fragment was detected in the ring counter are similar for $N_c \geq 15$. Fitting each of the distributions with a gaussian function for the range $6 \leq N_c \leq 35$, the means of the distributions for the one, two and three fragment cases are 12.8, 15.2 and 16.4,

respectively. The increase in the $\langle N_c \rangle$ as N_c increases can be understood as each case having more excitation energy shared between the projectile and the target and the suppression of peripheral collisions as N_{RC} increases.

4.3 Analysis of the $N_{RC} = 2$ case

The remainder of this chapter will focus on the case where only two fragments were detected. By examining the two-hit case, it may be possible to obtain information about of the breakup of a PLF*. Recently, there has been stimulating work on the PLF* decay which has shown a strong alignment of the decay (“aligned fission”) [3] and has attributed this behavior to dynamical processes. At present however, the essential characteristics of this decay mode are poorly determined.

The relationship between the individual Z of the detected fragments and velocity of the fragments is displayed in Fig. 4.8. Two ridges are apparent in Fig. 4.8. The first ridge extends from a Z value ~ 40 to a Z value of ~ 22 , increasing slightly in velocity as Z decreases. The part of the ridge from $Z = 20$ to 44 that has a nearly constant velocity is ~ 0.5 cm/ns less than the projectile velocity. The constancy of the velocity can be interpreted in terms of an abrasion-ablation scenario [8]. In this scenario the size fragment is determined by the geometrical overlap of the projectile and target nuclei. Little velocity damping occurs in such a picture. Continuing towards smaller atomic numbers, the yield reaches a in yield minimum around $Z = 9$ then increases to a maximum at $Z = 6$. Also noteworthy is that for products between $Z = 4$ and $Z = 14$ there is a second ridge in yield with a peak at ~ 6.5 cm/ns. A few scattered points are also observed large velocities to the side of the solid line. These scattered points arise from cases where two or more particles struck the same CsI(Tl) crystal, these events, however, occur with low probability as is evident in the figure. The relatively sharp cutoff for $Z < 14$ on the low velocity side of the two-dimensional charge-velocity distribution results from the energy thresholds for identifying particles.

To explore the velocity relationship between the two fragments detected in the ring counter, the velocity of the smaller/lighter fragment (v_L) is plotted against the velocity of the larger/heavier fragment (v_H) in Fig. 4.9. Evident in this figure are two prominent peaks. The peak (and the associated distribution) centered in the upper half of Fig. 4.9 is

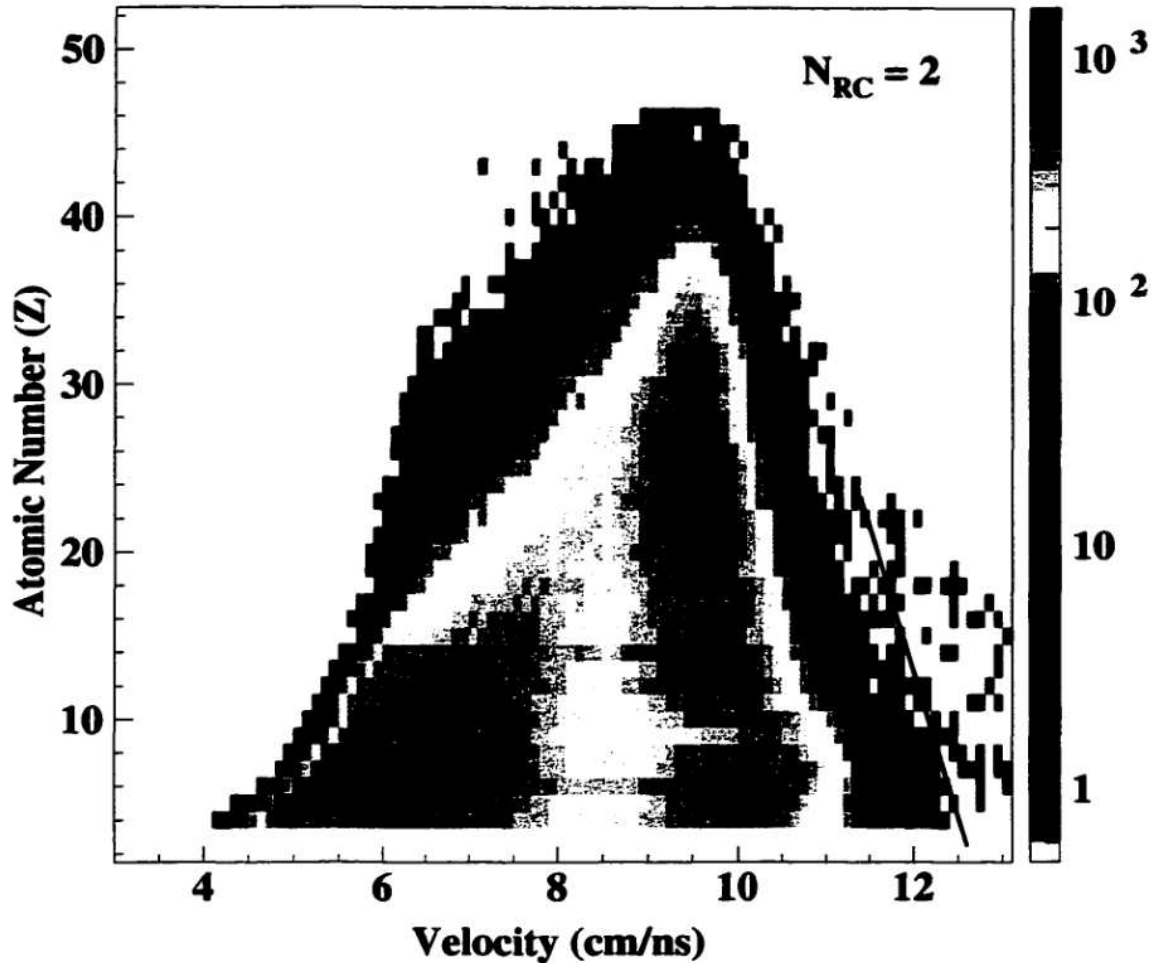


Figure 4.8: Dependence of the atomic number, Z , on its laboratory velocity for the case $N_{RC} = 2$. The solid line reflects a software rejection utilized in the analysis.

associated with events in which v_L is larger than v_H . In contrast, the distribution centered in the lower half of Fig. 4.9 corresponds to events in which v_H is larger than v_L . For the $v_L > v_H$ case the peak occurs at $v_H \sim 8.0$ cm/ns and $v_L \sim 10.1$ cm/ns. For this case one observes that the velocities of the two fragments are well correlated, that is to say as v_H increases, v_L increases. For the $v_H > v_L$ case, the distribution is quite different -- a strong velocity correlation is not observed. In particular, when $v_L < 7.5$ cm/ns the velocity of v_H is almost independent of v_L . The peak for the $v_H > v_L$ case occurs at $v_H \sim 9.5$ cm/ns and

$v_L \sim 7.0$ cm/ns. The valley in between the two peaks can be attributed to the conservation of momentum and the limited angular coverage of the ring counter. When the PLF* splits asymmetrically into two fragments, the conservation of momentum and Coulomb repulsion between the two fragments results in the different velocities. Also, the placement of the ring counter only permitted detection of fragments when the transverse velocity was between 3.6% and 7.3% of the longitudinal velocity.

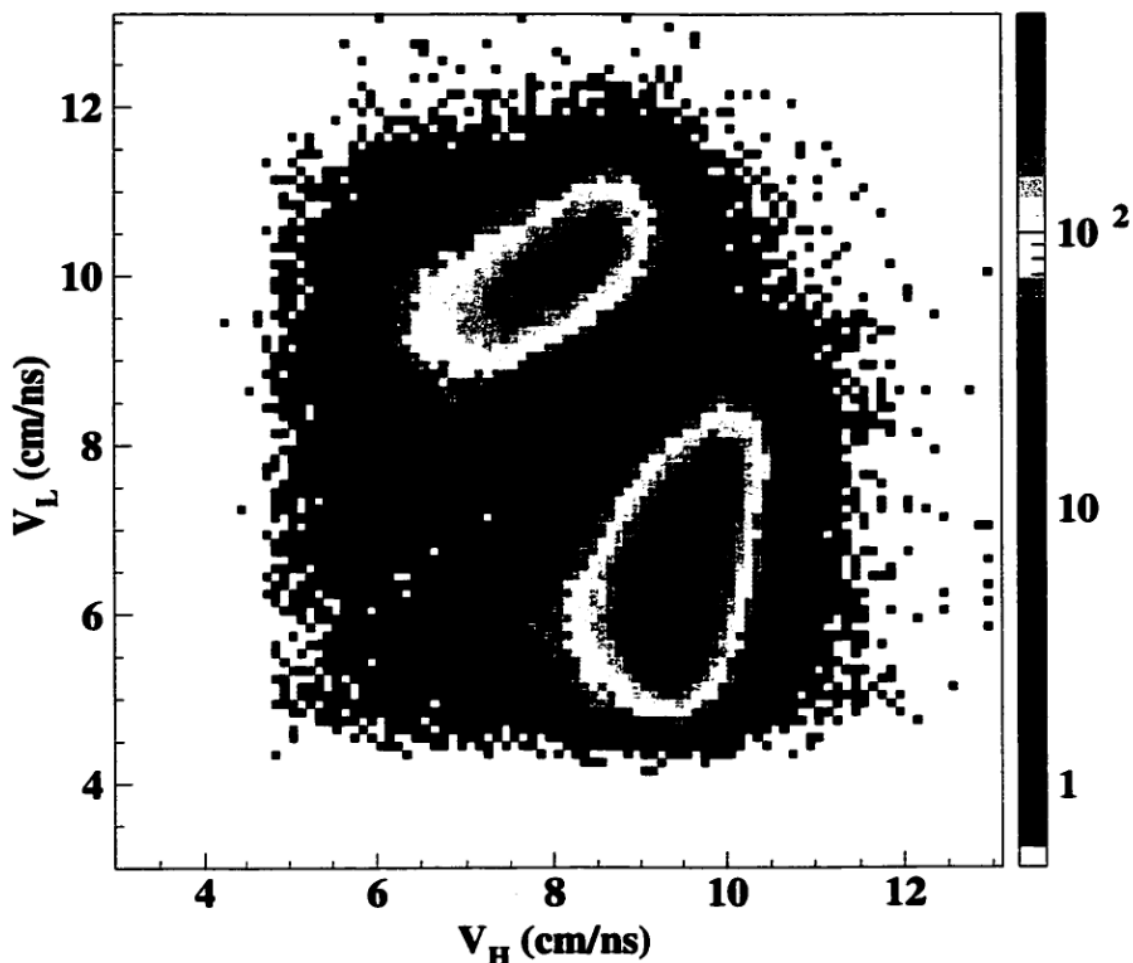


Figure 4.9: The velocity relationship between the two fragments detected in the ring counter for the larger fragment, v_H , and the smaller fragment, v_L .

Depicted in Fig. 4.10 is the relationship between the Z and the velocity of fragments detected for the cases when $v_H > v_L$ (left panel) and $v_L > v_H$ (right panel). For each case, $v_H > v_L$ or $v_L > v_H$ both fragments are plotted. In the right panel ($v_L > v_H$) two features are evident. The fragment with the smaller atomic number has a velocity of ~ 10 cm/ns and is relatively independent of Z . In addition the larger, slower fragment has a velocity- Z correlation. In the left panel the larger fragment's velocity is independent of the atomic number of the fragment and relatively constant at ~ 9.4 cm/ns while the smaller charge fragment has a velocity of ~ 6.25 cm/ns. From the results shown in Fig. 4.9 and 4.10, the velocity ordering of the two fragments clearly selects events which are different in some manner. If the PLF* were to decay isotropically in its rest frame, one would not expect the observed result. Clearly, the decay of the PLF* is not isotropic. In the remainder of this chapter, we will focus on differences in various observables while segregating the events based upon the velocity ordering.

The angular distribution of both fragments selected on the relative magnitude of their velocities is displayed in Fig. 4.11. The left panel displays the angular distribution when $v_H > v_L$ while the right panel displays the distribution when $v_L > v_H$. Several points are noteworthy. When $v_L > v_H$ (right panel), the angular distribution of both fragments is nearly identical. In addition, the the angular distribution is slightly peaked toward smaller angles. When $v_H > v_L$ (left panel) on the other hand, the angular distributions for Z_H and Z_L are quite different. The angular distribution for Z_H is strongly peaked at small angles, whereas the distribution for Z_L has a flat dependence with respect to angle.

In order to examine the decay pattern of the PLF*, we have examined the probability with which the two fragments in the ring counter are co-planar. If these two fragments result from the fission-like binary splitting of a common parent, one expects the two fragments to decay "back-to-back". This behavior can be investigated by constructing the $\Delta\phi$ distributions of the two fragments. Illustrated in Fig. 4.12 is the $\Delta\phi$ distribution of the two fragments in the ring counter selected by the velocity ordering of the pair. The minimum phi angle between fragments is $\Delta\phi$. The left panel represents all events, with a selection on the velocity ordering of the pair. The middle and right panels depict events selected on $6 \leq N_c \leq 10$ and $11 \leq N_c \leq 15$, respectively. The larger multiplicity selection corresponds to a selection of a more central collision. One feature that is consistent regardless of velocity

